

Carbon nanomaterials based nanofibrous scaffolds for regulation of stem cell growth and differentiation

DISSERTATION

zur Erlangung des akademischen Grades des
Doktors der Naturwissenschaften (Dr. rer. nat.)

eingereicht im Fachbereich Biologie, Chemie, Pharmazie
der Freien Universität Berlin

vorgelegt von

Yi Xia

aus Hunan, China

January 2021

The work presented herein was carried out in the research group of Prof. Dr. Nan Ma and Prof. Dr. Rainer Haag from September 2016 until January 2021 at the Institute of Chemistry and Biochemistry of the Freie Universität Berlin.

Hereby, I certify that the work presented in this thesis has not previously been submitted for a degree nor has it been submitted as part of requirements for a degree except as fully acknowledged within the text.

I also certify that the thesis has been written by me. Any help that I have received in my research work and the preparation of the thesis itself has been acknowledged. In addition, I certify that all information sources and literature used are indicated in the thesis.

Date and Signature

1st Reviewer: Prof. Dr. Nan Ma, Freie Universität Berlin

2nd Reviewer: Prof. Dr. Rainer Haag, Freie Universität Berlin

Date of Defense: 19. 04. 2021

Acknowledgements

First of all, I would like to express my sincere gratitude to my Doctoral supervisor Prof. Dr. Nan Ma and Prof. Dr. Rainer Haag for the academic and scientific support extended to me during the last four years. Prof. Dr. Nan Ma offered me a change to work with a very happy group AG Ma, I have learned so many experiment methods and research skills. Meanwhile, I am so grateful to have a chance to do research in outstanding AG Haag. The kind supervision from Prof. Dr. Rainer Haag highly improved my practical skills in doing experiments and the designing projects. His rigorous attitude towards academic research have a significant influence on me. What I learned here during the last four years helped me to have a great foundation for further research life.

I especially want to thank my collaborator Prof. chong cheng (Sichuan University) for his help in my academic life. He lighted the start of my research, I have learned so much from his guidance including project discussions, basic chemistry technology introduction, and manuscript improvement.

I also want to thank my colleague Dr. Katharina Achazi and Dr. Falko Neumann for their kind help with basic principles and experimental introductions in the biolab. I also thank Dr. Stefanie Wedepohl, Paul Hillmann, Elisa Quaas, and all the other members in the biolab for their patient explanations to help me solve the problem during my experiments.

I acknowledge all the former and present group members of the Haag group and the Ma group for the good atmosphere. The regular group meeting and subgroup meeting played an important role in the study during my PhD, which offered good opportunities for me to discuss with each other and stretch my mind in the research field. I gratefully thank the group members especially Mingjun Li, Jianguang Zhang, Suqiong Zhou, Chuanxiong Nie, Xin Fan, Lang Ma, Yan Li, Wenzhong Li, Yong Hou, Leixiao Yu, Yuanwei Pan, shaohui Xu and Wanjun Liang for the nice discussion during the lab work.

I would like to acknowledge Eike Ziegler, Jutta Hass and Dr. Wiebke Fischer for dealing with the complicated paperwork, chemical ordering and lab techniques. I would like to thank Dr. Pamela Winchester for language polishing of my manuscripts and dissertation. I would like to thank the Core Facility BioSupraMol and Sichuan University for offering multiple equipment for the analysis of biomacromolecular and supramolecular compounds. I would like to thank Dr. Shuang Li for the XPS test and analysis. I am grateful for the financial support afforded by China Scholarship Council (CSC) during my Ph.D. thesis.

I am grateful to my family and friends for their care and happy company, especially to my parents for unconditional love and encouragement during all these years. Also, I want to thank my husband Hua Yang and our loving daughter Jiayue Yang for their company.

Table of contents

| | |
|--|-----|
| 1. Introduction | 1 |
| <u>1.1.</u> Stem Cell Scaffolds | 2 |
| 1.1.1. Hydrogel | 3 |
| 1.1.2. Fibrous Scaffolds | 5 |
| 1.1.3. Porous Foaming Scaffold | 7 |
| 1.2. Interaction between Scaffolds and Stem Cells | 9 |
| 1.2.1. Physical Cues | 11 |
| 1.2.2. Chemical Cues | 14 |
| 1.3. Carbon Nanomaterials | 16 |
| 1.3.1. Carbon Nanotubes | 17 |
| 1.3.2. Graphene | 19 |
| 1.3.3. Carbon Dots | 21 |
| 1.4. The Design of Bioactive Nanostructured Fibrous Stem Cell Scaffolds | 24 |
| 2. Scientific Goals | 26 |
| 3. Publications | 28 |
| 3.1. A Multivalent Polyanion-Dispersed Carbon Nanotube towards Highly Bioactive Nanostructured Fibrous Stem Cell Scaffolds | 28 |
| 3.2. Multivalent Polyanionic 2D Nanosheets Functionalized Nanofibrous Stem Cell-based Neural Scaffolds | 51 |
| 3.3. ZnO/Nanocarbons-Modified Fibrous Scaffolds for Stem Cell-based Osteogenic Differentiation | 90 |
| 4. Summary and Outlook | 118 |
| 5. Kurzzusammenfassung | 120 |
| 6. References | 122 |
| 7. Abbreviations | 135 |
| 8. Appendix | 136 |
| 8.1 Publications | 136 |

1. Introduction

Millions of people worldwide require regenerative therapies every year. The repair and replacement of damaged cells and tissues with stem cells are significant and urgent in basic research and medicine.^[1-3] Stem cells could replicate itself into more of the same type of stem cells or differentiate to various of other cells types, which could be secluded from many kinds of tissues, for example umbilical cord blood, embryos, or organs from adult.^[4]

In 1981, Evans et al. separated embryonic stem cells (ESCs) from mouse, which is a milestone in the stem cell research. From then on, an increasing number of attention have been attached to investigation of stem cells in tissue therapy.^[5] ESCs were obtained from the inner layer of embryoid body during the early period stage, which provides the differentiation possibility towards three germ layers, including mesoderm, ectoderm and endoderm. Although ESCs attracted much attention due to the pluripotency, they faced the ethical problems of destroying the embryos, which is especially difficult in investigating human ESCs.^[6] Yamanaka et al. started an entirely novel avenue in stem cell research in 2006 by converting fibroblast cells to ESC mimicking cells, namely, induced pluripotent stem cells (iPSC). In many aspects, iPSCs are very alike to ESCs, such as potential differentiation lineage, embryo formation, doubling time, chromatin methylation patterns, typical proteins and genes expression.^[7] Adult stem cells are usually have confined differentiation potential, most of them are related as predecessors of multilineage cells, which could be discovered in adipose tissue, bone marrow or umbilical cord blood. The most popular and widely investigated stem cells were mesenchymal stem cells (MSCs) with the differentiation potential towards osteoblasts, adipocytes, chondrocytes and myocytes. Meanwhile, MSCs were comparatively simple to isolate, harvest, and expand with the stemness and multipotency well obtained during self-renewal *in vitro*.^[5, 8]

1.1. Stem Cell Scaffolds

Most cells in human body proliferate or differentiate themselves in extra-cellular matrix (ECM) in three dimensions.^[9] The special microenvironment for stem cells termed the “niche,” which is mainly located in 3D environment although varies in physical and chemical properties based on the tissue type.^[10] ECM provides physical and chemical stimuli, which not only provides mechanical scaffolds or anchoring points, but also exert significant influence on regulation of stem cells metabolic functions, morphology, adherence, migration, differentiation and development.^[11, 12] Surround by an exceptionally complex, dynamic and vibrant network environment, stem cells scaffolds sustained the body tissue and cells structural integrity through conveying the stress from movement and gravity.^[1] Through the interaction with cell surface receptors and intracellular signaling molecules, stem cell scaffolds could determine the cell phenotype through regulation of gene expression.^[1, 13] Figure 1 illustrates the potential and process for stem cells engineering on scaffolds. Stem cells derived from embryos, adult tissues or somatic cells reprogramming could be classified to harvest a single type of target cell population before cultured on the scaffold or seeded straightly on a scaffold for differentiation. The scaffolds seeded with cells could be cultured to obtain a intended organ or tissue before implantation *in vivo*.^[5]

It is known that different tissue and organs have various morphology and physiological properties and ECM as the consequence of cells’ integrated, continuous and reciprocal interaction in tissue differs accordingly.^[14] Although conventional 2D surfaces where stem cells were cultured with multiple nutrients, cytokines and growth factors in media offered the major knowledge in modern cell and tissue research, however, the lack of ECM mimicking 3D environment where most nutrients were provided in bound state, may leads to the development of physiologically compromised or mislaid stem cells.^[4, 5, 15, 16] The engineering properties desired stem cell 3D scaffolds include (a) porous structure available for cell adhesion, proliferation, migration, differentiation;^[17] (b) Interconnect networks for oxygen, nutrients and waste to transfer and deliver through the whole cell or tissue mass;^[18] (c) physically and chemically

bioactive surface to promote cell–material interactions;^[19, 20] (d) mechanical proper function for cell differentiation and biosynthesis.^[19, 21, 22] Easy to handle in dynamic and various environment is necessary for the various applications in which extreme fragile or brittle materials may not fit. Meanwhile, the proper mechanical properties or special cell-interactive chemical cues in the materials are favorable.^[23]

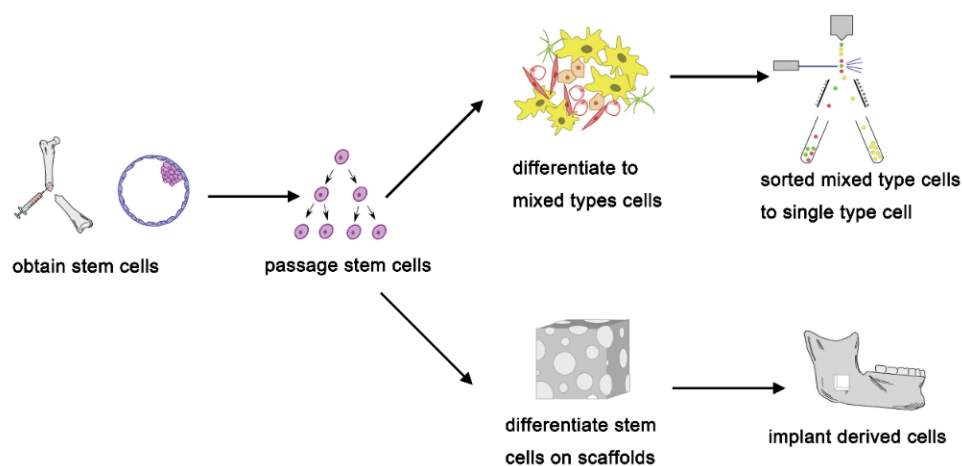


Figure 1. Scheme outlining the potential for stem cells engineering. Stem cells could be passaged and expanded in culture. Afterwards, they can then be either seeded directly on a scaffold and grown in culture to develop a desired tissue prior to implanting in the body, or differentiated in culture and sorted to obtain a purified population of a target cell type before seeding on the scaffold. Reprinted from Ref.^[5] with kind permission from the Elsevier.

1.1.1. Hydrogel

Hydrogels are extremely hydrophilic macromolecular networks, which are mainly prepared from soluble polymers by chemical or physical crosslinking.^[24-26] Since hydrogels are hydrophilic, adequately flexible, tissue-like with a high water content and sensitive to the physiological environments, hydrogels are widely investigated as excellent candidates for stem cells research.^[27] Moreover, many hydrogels exhibit swell and de-swell property in water at reversible way, which is sensitive to specific environmental stimuli, such as temperature, ionic strength and pH.^[28, 29] Thus, hydrogels change along physiological variable are increasingly attractive in several

biomedical applications.^[29]

Various kinds hydrogels could physiologically improve stem cells culture. Those hydrogels could be prepared from synthetic or natural materials or a combination of both. As shown in Figure 2a, Deming et al. developed injectable diblock copolypeptide hydrogels containing hydrophilic component of modified l-methionine to promote neural stem cells transplantation viability and efficiency at the central nervous system (CNS) *in vivo*.^[30] After the injection of the cell-matrix complex into the mouse CNS host tissues *in vivo*, the ionic hydrogels could achieve self-assembly to distinct, well-formed hydrogel networks which is very compatible with the original CNS tissue. The amazing biocompatibility and full degradation *in vivo* suggested that injectable hydrogels are appropriate conveyance for further investigation of neural stem/progenitor cell transplantation in CNS disease or injury models. Mooney et al. prepared injectable, pore formation hydrogels that in accompanied with void-forming and change elasticity (Figure 2b).^[23] Cells were firstly encapsulated to the originally formed hydrogels, then the subsequent degradation of solid phase porogens *in situ* via hydrolysis could create voids within the hydrogels and offer space for stem cells to grow and proliferate when placed in physiologic conditions. The following cell proliferation and migration rate and corresponding the porogens degradation velocity would decrease the hydrogel elasticity and refrain the cells from the confinement of solid porogens. Since the injectable hydrogels could protect the viability and phenotype of the MSCs during the transplantation process, it is believed to be a suitable vehicle to convey the stem cells *in vivo* transplantation in the circumstances of human models. Yu et al. established an approach to prepared PA hydrogels which have linear stiffness gradients spanned both at illness conditions and biologically appropriate ranges.^[31] The first layer of hydrogel were made by the acrylamide and cross-linker in a glass mold with a slop cover on surface, then the second layer of acrylamide was prepared in the mold with the cover of the first slop PA gel to obtain a two layer of ramp-shaped and inversely oriented hydrogel with adjusted stiffness gradient at interface between the cells and matrix. Cryo-SEM images confirm that a pore size grades from biggest to

smallest according to the hydrogels from the soft side to stiff side, which allows the exhibition of a constant increase of stiffness gradient on a single sample without the confusing factor of different samples and cells variety. The gradient hydrogels could be used to investigate the stiffness-dependent stem cells morphology, migration, and differentiation, which is important for further investigation of stem cell therapy.

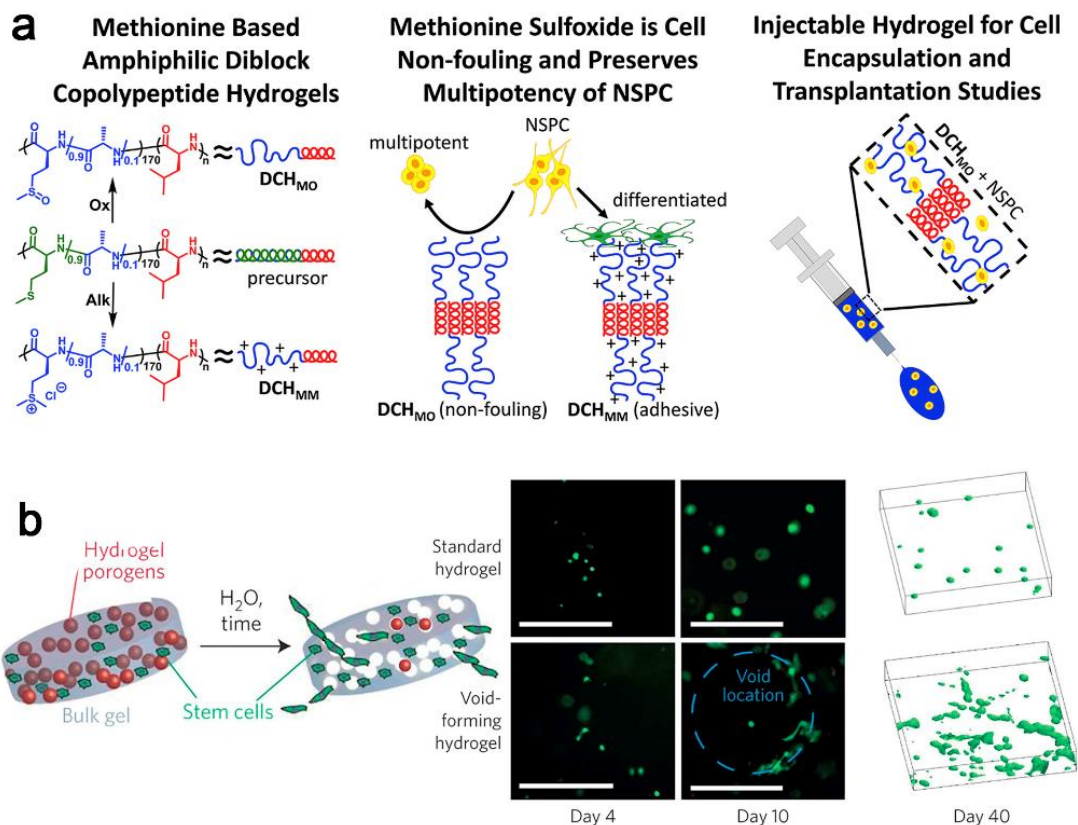


Figure 2. a) Synthesis and application of methionine based amphiphilic diblock copolyptide hydrogels. Reprinted from Ref.^[30] with kind permission from the Elsevier. b) Schematic strategy to create void-forming hydrogels. Void-forming hydrogels (bottom) could offer more space for cells to grow compared with standard hydrogels (top). Reprinted from Ref.^[23] with kind permission from the Nature Publication.

1.1.2. Fibrous Scaffolds

Fibrous scaffolds are meshes made of the weaved or overlapped fibers from numerous

polymers with desired mechanical and chemical properties. These meshes possess big surface area to volume ratio due to the extraordinary porosity and pore interconnectivity, thereby enabling more effective gases, nutrients and wastes exchange for resident stem cells.^[32-34] Meanwhile, the high surface area and porosity enable superior space for cell adhesion, which is significant for cells to proliferate and function. Thus, the ease of fabrication and resulting superb physical and chemical properties makes fibrous scaffolds a promising substrate for stem cell culture.^[33] Fibrous scaffolds can be fabricated using a variety of techniques for example electrospinning, phase separation, template synthesis, drawing, self-assembly and combinations of these.^[35] Each method forms fibers with different diameters from macro ($> 100 \mu\text{m}$) to micro (10-100 μm) to nanometer (5-1000 nm) size. Due to their processability and physical properties, fibrous scaffolds are exciting candidates for stem cells research in numerous tissue repair including bone, cartilage, nerve, and blood vessels.^[35-37]

Chen et al. combined polymer chemistry, electrospinning and soft lithography in fabrication of a synthetic fibrous scaffold with user specified structure and changeable mechanics to explore the mechanism of sensing interaction between the cells and stiffness in desired ECM mimicking architecture (Figure 3a)^[33]. Fiber networks were tuned with diameter, density and anisotropy by electrospinning using basal material methacrylated dextran11 (DexMA) and RGD. The increase of flat hydrogel surfaces stiffness at certain level could promote the MSCs adhesion and proliferation. Higher fiber stiffness allows more easy and active cellular forces to increase the ligand density on cells surface and improve the focal adhesion formation, which could activate related signaling and promote the cells to mobilize and migrate to nearby fibers. As shown in Figure 3b, Luo et al. fabricated polycaprolactone (PCL) electrospun fibrous scaffolds in mesh-like, aligned and random patterns^[34]. The fibrous structure not only played a significant role in promotion of MSCs paracrine function, but also stimulated the cells differentiation with different orientation characteristics. The fibrous topography offered special microenvironment for the modulation of paracrine function in MSCs. Meanwhile, the expression of pro-angiogenic and anti-inflammatory cytokines were

increased on fibrous scaffolds both *in vitro*. Moreover, the medium obtained from fibrous scaffolds cultured MSCs environment could improve the trauma healing, accelerate macrophage gathering and polarization to the recovering phenotype in the rat skin trauma model *in vivo*.

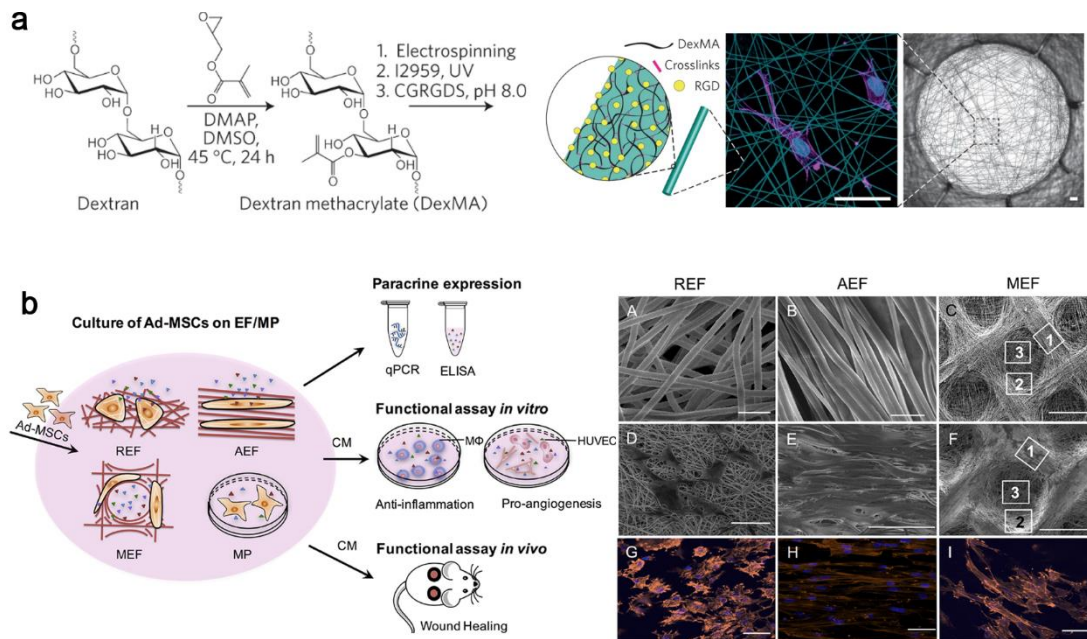


Figure 3. a) Hierarchical overview of fabricating cell-adhesive suspended networks of DexMA fibres. Scale bars, 10 μm. Reprinted from Ref.^[33] with kind permission from the Nature .b) The experimental design to investigate the influence of the fiber morphology and fiber orientation on the paracrine secretion and function of Ad-MSCs. Reprinted from Ref. ^[34] with kind permission from the Elsevier.

1.1.3. Porous Foaming Scaffold

Porous foaming scaffolds have controlled micro-and nano-metric pore sizes, and topographies on the pore surface of foam could promote the adsorption of proteins, to guide specific cell/scaffold interaction, and to stimulate stem cell migration, differentiation, phenotypic expression and the deposition of stem cells.^[38, 39] Meanwhile, multi-scaled pore structures could promote localization of cells and support the transport of fluid and oxygen necessary for cell survival and new tissue synthesis in three dimensions.^[40-42] Considering the surface-to-volume ratio, pore size distribution,

and pore geometry and interconnection, different approaches were investigated for the synthesis of porous scaffolds including porogen leaching, phase separation, gas foaming and solid free form fabrication.^[43] However, each method has intrinsic limitations, for example, leaching techniques and gas foamed scaffolds have intact pore walls with few interconnected holes because of the neighboring particles contact with each other in the scaffold network.^[44] Those closed pores either in the inner or outer interfaces are detrimental for the communication of cytokines, growth factors, nutrients and cells.^[45] Moreover, it is hard to prepare scaffolds with multi-scaled pore distribution under spatial control by utilizing a single method.^[46] Thus, the combination of various processing techniques are the most efficient approach to prepare porous foaming scaffolds with nano or micro meter pore size features.^[47]

Figure 4a exhibits the preparation process of an exceptionally interconnected porous foaming scaffolds with different scale pore structure through the integration of porogen leaching and gas foaming techniques.^[48] Firstly, the biomaterials are mixed with porogens, usually gelatin particles or sodium chloride (Step 1), and the foaming of the polymer/particles system are followed (Step 2). Then, the selective removal of the porogen agent from the foamed matrix permits the final completion of multi-scaled pore structure. For example, Jones et al. synthesized great Ca-Mg silicate porous foaming scaffolds by preceramic polymers combined with phase separation and gas forming methods (Figure 4b).^[49] Wollastonite-diopside and akermanite ceramic porous foam scaffolds were prepared by the liquid silicone pyrolysis after blended with reactive fillers. Through taking control of water evaporation process at 350 °C, the general porous structure could be achieved. Then the samples were heated to 1100 °C to obtain a homogeneously distributed interconnected pore structure (160–180 μm) ceramic scaffolds with high compressive strength (1–2 MPa) and significant porosity over 80%. Cytotoxicity analysis proved the great biocompatibility of Akermanite and wollastonite-diops scaffolds. Moreover, the Mg-containing foams could obviously improve the typical osteogenic markers expression such as osteocalcin, osteopontin and collagen type I compared with Mg-free scaffolds, which suggest the promotion of

osteogenic differentiation potential and offers new platform for the design and process of large scaled clinical scaffolds for bone therapy.

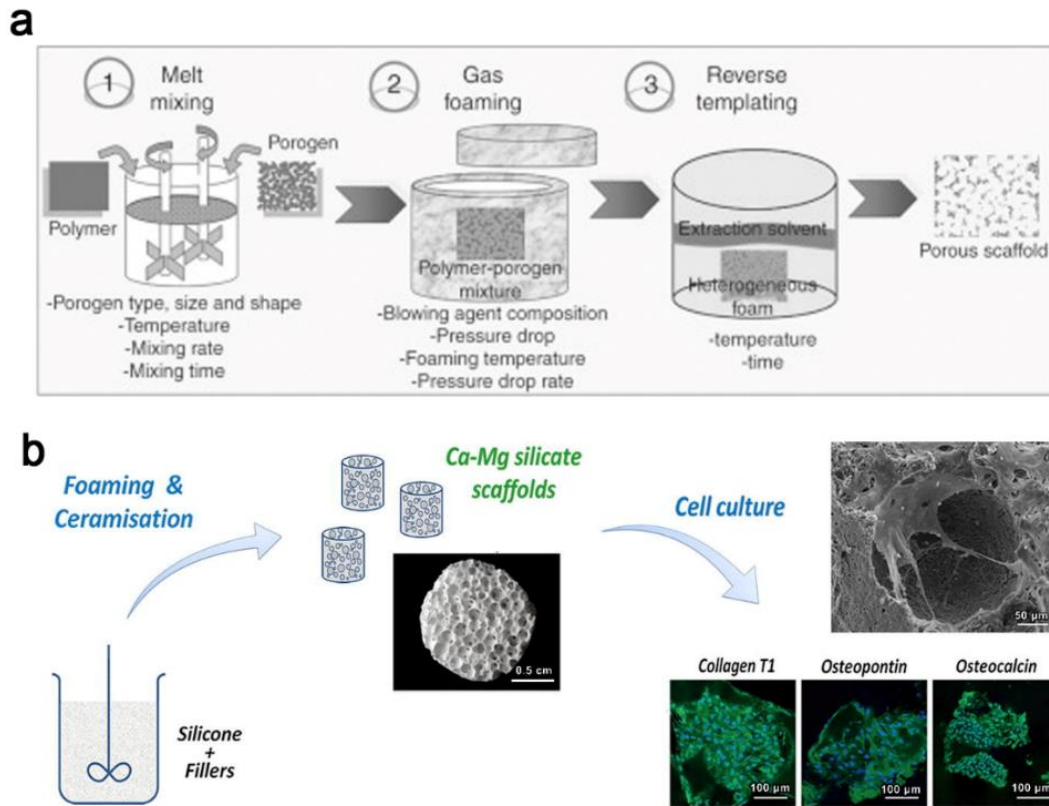


Figure 4. a) Scheme of the combined approach based on gas foaming and porogen leaching suitable for the design and fabrication of multi-scaled porous scaffolds for TE. Reprinted from Ref.^[48] with kind permission from the SAGE. b) Scheme of the preparation process of ceramic foams; the SEM and confocal image of the cells grown on the foams. Reprinted from Ref.^[49] with kind permission from the Elsevier.

1.2. Interaction between Scaffolds and Stem Cells

Stem cell behaviors, for example, the adhesion, proliferation, pluripotency maintenance and differentiation, are guided both by stem cells self-property and external microenvironment.^[50-55] Different element in the stem cell niches and external microenvironment plays pivotal role in their fates. Firstly, the cell-soluble factor interaction, different soluble factors including bioactive molecules, nutrients, cytokines and growth factors could go through the stem cells membrane and change the cell metabolism or even gene information. Secondly, the cell-cell interaction, the connected

cells or meet cell could communicate with each other via homophilic, heterophilic and linker pathway to achieve cell-cell recognition and binding by the cadherin, selectin, Ig-superfamily, integrin and hyaladherin on the cell membrane. Thirdly, the cell-biomaterial interaction, stem cells could sense and react according to the biomaterial's stiffness, conductivity, hydrophilic-hydrophobic property, surface charge and so on.

The physical cues and chemical cues of the scaffolds could trigger the cell-soluble factor interaction, cell-cell interaction and cell-biomaterials interaction by the change of scaffolds material and preparing methods, which could vary the porosity, stiffness, rigidity, conductivity, hydrophilic-hydrophobic property, surface charge of the scaffolds and further alter the stem cell microenvironment and niches. The chemical and physical cues could influence and be influenced by the cell-biomaterials interaction and cell-cell interaction through the adhesion of cells and the secretion of various kinds of proteins such as paracrine signaling hormones in the stem cells niches. Thus, the physical cues and chemical cues could apply influence on stem cell lineage specification towards neural cells, cardiomyogenic, adipogenic, chondrogenic and osteogenic lineages.^[56-61]

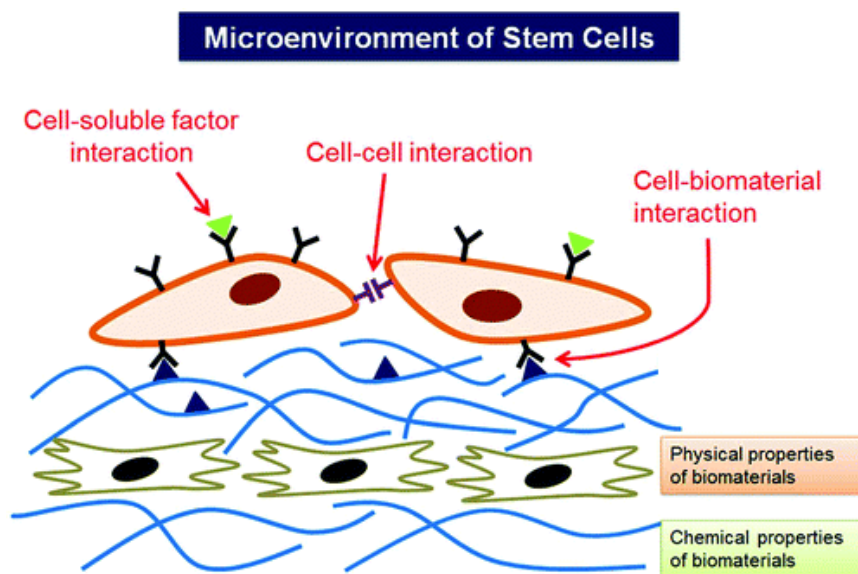


Figure 5. Schematic representation of the microenvironment and niches of stem cells and their regulation by the following factors: soluble factors, such as growth factors or cytokines, nutrients, and bioactive molecules; cell–cell interactions; cell–biomaterial interactions. Physical, and chemical properties of biomaterials also regulate stem cell

fate. Reprinted from Ref.^[62] with kind permission from the ACS Publications.

1.2.1. Physical Cues

Since a variety of microenvironment property contribute to the stem cell behavior regulation, physical cues, for example, scaffolds geometry/topography at the nanoscale, mechanical properties, matrix stiffness or applied forces, electrical property and applied field (EF) stimulation play an important role and are commonly investigated in stem cell fate regulation.^[63-65] Physical cues could activate or stimulate the cell membrane protein, such as receptors and identification proteins, which be transduced to biophysical signals and in turn adjust the signaling cascades to regulate stem cells fate. For example, the modification of actin cytoskeleton leads to the up-grade expression of transcription factors and the remodeling of chromatin enzymes, which could trigger genetic expression and affect the stem cell differentiation fate. This is a common stem cell signal transduction accompanied by change of scaffold mechanical property.^[21, 55]

The mechanical property of scaffolds for stem cells support inform the fundamental insights into the stem cells' mechanobiology for regenerative therapies. Scaffolds with defined mechanical properties such as stiffness and viscoelasticity, could be used to prime stem cells *in vitro* before transplantation to promote proliferation, as well as to particulate stem cell fate *in vivo* following transplantation (Figure 6a).^[66] For example, previous research suggests that synthetic hydrogel with certain elasticity (around 60 kpa) could enhance MSCs osteogenesis either *in vitro* or *in vivo*; The programing of porosity in a viscoelastic alginate system could also facilitate the bone host integration;^[23, 67] The change of matrix stiffness could trigger the hematopoietic multilineage reconstitution and affect the systemic delivery;^[68] Assembled from annealed microgels, the bulk gel scaffold offered proper mechanical support and interconnected multi-scale pores to expedite cell adhesion and migration, which could promote cutaneous-tissue formation and further regeneration *in vivo*.^[69] The synthesized mechanically dynamic hydrogel networks could direct intestinal stem cell proliferation and subsequently lead to potential intestinal, thus providing a suitable

replacement of animal developed material scaffolds in the culture of stem cell developed organoids.^[70] Soft hydrogel at muscle elasticity mimicking scale could obviously promote the muscle stem cell proliferation, and contribute to the extensive muscle regeneration *in vivo*, which suggest the recapitulating the tissue rigidity provide possibility for the stem cell based muscle wasting therapy.^[59, 71]

Electric stimulation (EF) could evoke stem cell response and lead to a series of cascade cellular reaction. After electric stimulation, the major signal pathways include the intracellular calcium ion concentration, cell surface receptors reassembling or clustering, heat shock proteins and reactive oxygen species participation, ATP production, cytoskeletal remodeling and so on could be activated, which plays a pivotal role in direction of stem cell specification and stem cells-based tissue therapy and medicine. The cardiac muscle tissue contraction has unique electrical signal pathways such as gap junction channels, thus the designing of cardiac-mimetic electrical microenvironment during *ex vivo* culture could lead to the progressive generation of functional cardiac tissue. The autonomous beating rate of cardiomyocytes could adapt themselves to the stimulated frequency, and the rate-adaptive behavior could last for long and transferred the surrounding cardiomyocytes. Thus, cardiomyocyte maturation and autonomous beating could be tuned by electrical conditioning treatment, which is useful to treat cell-based arrhythmia for heart therapy. Basu et al. proved the pulsed electrical stimulation could improve the mesenchymal stem cells towards cardio-progenitor phenotype genesis in spite of the MSCs' trans-differentiation difficulty to cardiomyogenic progenitors. (Figure 6b).^[64] The reason in their article might be the paracrine of MSC lead to the cardiomyocytes mimicking structure after the electrical stimulation along with chemical inducers. Lim et al. elucidated that the exogenous EF stimulation is significant in promoting hESCs derived embryoid bodies (EBs) cardiogenesis.^[72] A brief electrical stimulation for 2 weeks could markedly escalate the beating EBs fraction in company with noticeably increase of cardiac gene expression including troponin T, sarcomeric α -actinin, and myosin heavy chain (Figure 6c).^[72] From a tissue engineering perspective, Gordana Vunjak-Novakovic exhibited that stem

cell developed cardiomyocytes cultured in 3D environment with electrical stimulation could improve the connexin expression, modify automaticity, support mature, electromechanically coupled cells regeneration and enhance cardiomyocyte maturation (Figure 6d).^[73]

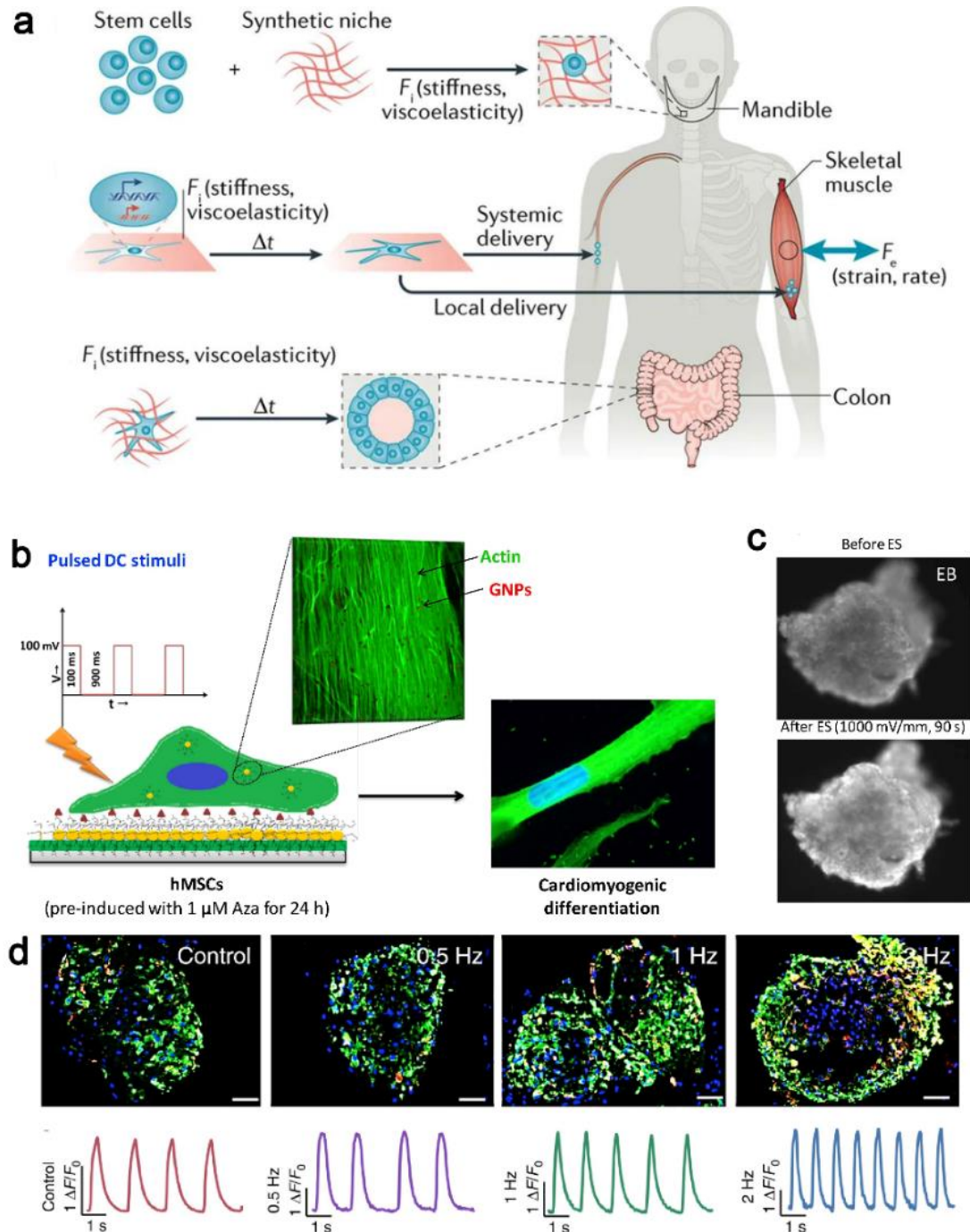


Figure 6. a) Mechanical cues of stiffness and viscoelasticity can also be used regulate stem cells self-organization, differentiation process, which could then be subsequently transplanted for organ repair or replacement. Reprinted from Ref.^[66] with kind

permission from the Nature Publications. b) Electrical field stimulation assisted gold nanoparticles (GNP) actuation and then induced cardiac differentiation of stem cells. Reprinted from Ref. ^[64] with kind permission from the Elsevier. c) Increased ROS production in embryoid bodies after EF application. Reprinted from Ref. ^[72] with kind permission from the Elsevier. d) hESC derived cardiomyocytes adapting their natural beating frequency to the EF stimulation frequency. Frequency dependent change in calcium cycling upon ES is shown in the bottom panel. Reprinted from Ref. ^[73] with kind permission from the Nature Publications.

1.2.2. Chemical Cues

The chemical cues from the cell culture microenvironment, such as cell-adhesive ligands and exogenous growth factors, hormones, hydrophobicity, charge and surface chemistry could affect and regulate the stem cell pluripotency and differentiation fates.^[74] Among them, growth factors are the most common and significant one, which is quite popular in the tissue therapy field, for example cartilage and bone regeneration, cardiac repair and neuronal differentiation.^[75] General growth factors contain fibroblast growth factors (FGF), transforming growth factor (TGF), epidermal growth factor (EGF), hepatocyte growth factor (HGF), insulin-like growth factor (IGF) and platelet-derived growth factor (PDGF).^[75-77] Bone morphogenetic proteins (BMPs), as a family member of TGF, plays a significant role in stem cells differentiation and specification, especially in promoting MSCs towards osteoblasts and chondrocytes.^[78] The paracrine of IGF secreted from MSCs could activate SDF-1alpha/CXCR4 signaling pathway in improving cardiogenesis.^[79] The integration of PDGF and laminin were proved to enhance U-MSCs neural differentiation potential.^[80] HGF could activate Wnt signaling pathway and then promote stem cells differentiation.^[81] Meanwhile, VEGF were investigate to improve stem cells differentiation potential towards vascular endothelial cells.^[79, 82]

Chemicals directed differentiation has obtained much attention due to the precise control, easy delivery, consistent reproducibility and efficient scalability.^[83-86] The

chemical cues method is safe and effective without the necessity of genetic manipulation, such as mandatory gene ectopic expression, virus-mediated gene integration or gene delivery, which is very efficient and convenient in both experimental research and clinical therapy.^[83] Small molecules with multiple properties for example enzyme inhibition, signaling control or epigenetic modulation were combined and utilized to modulate and direct stem cells differentiation.^[83] There are plenty of successful trials been reported in inducing stem cells differentiation with chemicals towards cardiomyocytes,^[87, 88] neurons,^[89, 90] and pluripotent stem cells.^[91] Goldman et al. successfully established protocols in stimulating both hESCs and hiPSCs cells lines to human oligodendrocyte progenitor cells (OPCs) on large scale.^[90] Kim et al. developed highly enriched populations of skeletal muscle-like cells from mouse fibroblasts applying a chemical cocktail method with various modulators including cAMP agonists, TGF- β , glycogen synthase kinase and histone deacetylation inhibitor (Figure 7a).^[92] The combination of chemicals also promote various cell types towards myogenesis differentiation potential, which not only proved the chemical inducted cells differentiation, but also highlighted the significance of signaling pathways in conducting mesodermal lineages cells towards muscles.^[87, 89, 91]

Hydrophobicity and surface chemistry of cell environment could affect cellular internalization of the cell membranes. Lorenz et al. reported that hydrophobic nanoparticles and carboxylated nanoparticles were taken up on a larger scale by MSC.^[93] As shown in Figure 7b, hydrophilic nanoparticles poly(methyl methacrylate) (PMMA) were taken up less by MSCs compared that with hydrophobic poly(lauryl methacrylate) (PLMA), which may due to the hydrophobic interactions between the nanoparticles and serum proteins in the media and cell lipid membranes. Surface chemistry were proved to exert effects on cellular behavior as well. The carboxylated poly(t-butyl methacrylate) (PtBMA) nanoparticles could be taken up by the MSCs on a large scale, which provides a clue and platform for the investigation of delivery of cytokines and growth factors into the cell membranes in the growth microenvironment or scaffolds (Figure 7c).^[93]

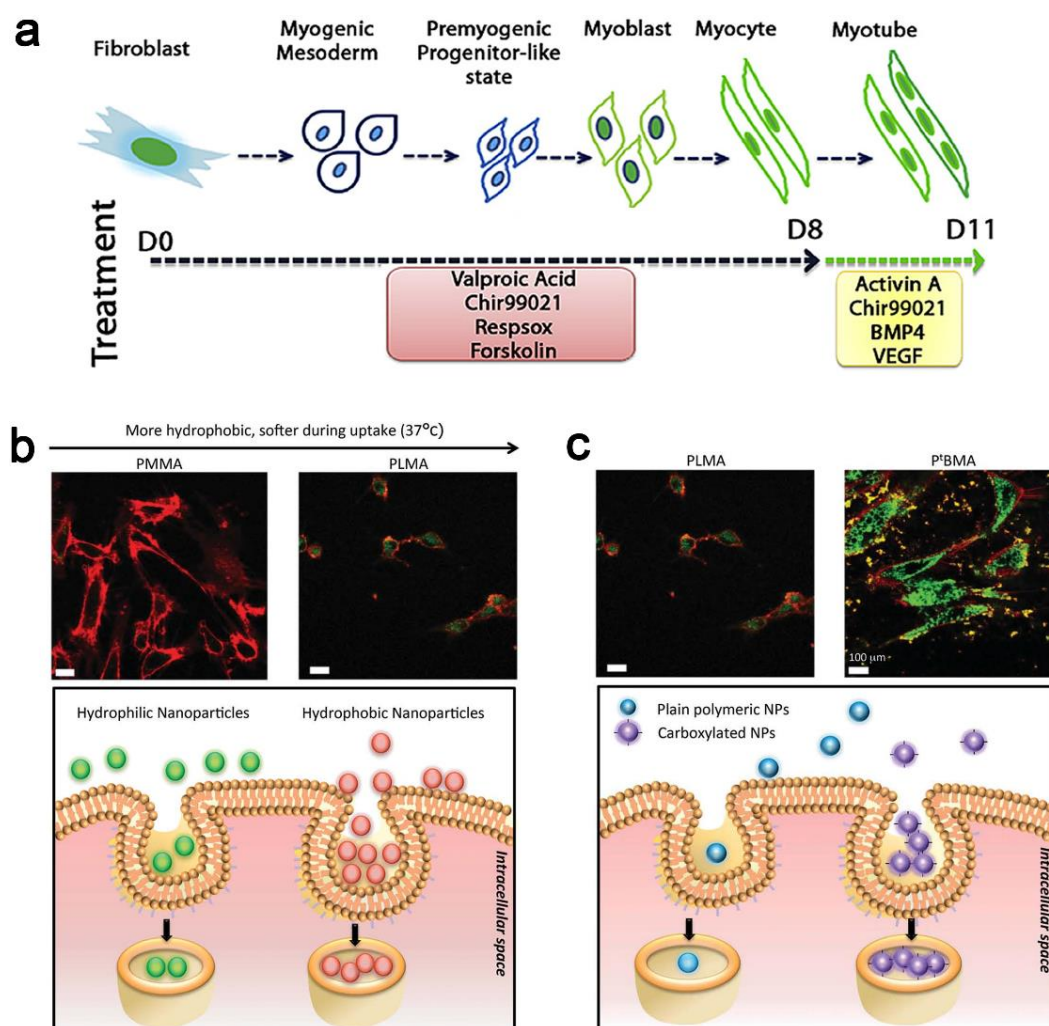


Figure 7. a) Schematic representation of various stages through which CiSMLC pass through during chemical induction from fibroblasts. Overall schema of chemical treatment protocol is also depicted. Reprinted from Ref. ^[92] with kind permission from the Elsevier. b) Effects of hydrophobicity and surface chemistry of nanoparticles on cellular internalization. c) Surface chemistry was also shown to influence cellular uptake. Reprinted from Ref. ^[93] with kind permission from the WILEY-VCH.

1.3. Carbon Nanomaterials

Carbon nanomaterials (CNMs), for example carbon nanotubes (CNTs), graphene sheets and carbon nanodots have special optical properties, high conductivity, outstanding mechanical properties and nano-topography, which play an important role as candidates

of promising scaffolds in stem cells therapy, an interdisciplinary application concentrate on *in vitro* development of biological replacements that could restore organ and tissue (Figure 8). Since synthetic scaffolds for stem cells regeneration are supposed to be ECM mimicking concerning of physical structure and chemical composition,^[94] CNMs not only reinforce the mechanical property of organic/inorganic artificial scaffolds, but also be applied to design stem cell scaffolds as physical cues in regulation of stem cells behavior. Moreover, the high conductivity of CNMs provide and electrically conductive environment for the stem cells and offer a potential to apply electrical stimulation to the stem cells. Thus, multiple CNMs were applied and developed in the functionalization of artificial scaffolds to improve biocompatibility and to regulate stem cells adhesion, proliferation, migration and differentiation.^[95, 96] The interaction between CNMs modified scaffolds and stem cells gained increasing attention in stem cell and tissue therapy and own huge potential in organ repair and replacement.^[97-99]

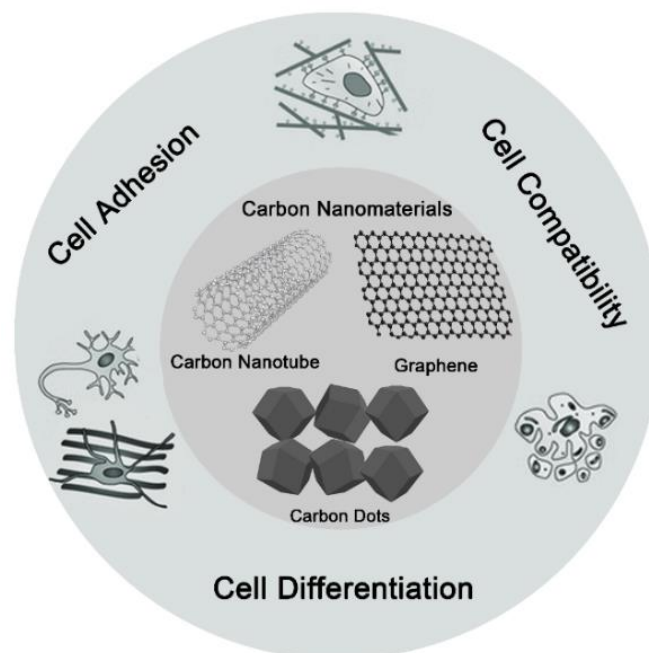


Figure 8. Common CNMs for stem cell therapy, such as CNTs, graphene sheets and carbon dots. Carbon-based nanomaterials affect compatibility, adhesion and differentiation of cells.

1.3.1. Carbon Nanotubes

CNTs have cylinder-like form from graphene sheet rolling with a single wall or multiple

walls, namely single-walled nanotubes (SWNTs) and multi-walled nanotubes (MWNTs), whose length varieties from 100 nm to 1 cm and diameters are around 1-2 nm and 10-100 nm, respectively.^[100, 101] CNTs have special optical properties, high conductivity, outstanding mechanical properties and nano-topography, offering novel insights and clues for designing artificial scaffolds to combine the physical and chemical cues in regulation of stem cells behavior.^[102] Moreover, the hydrophobic property of sp² graphitic structures and corresponding huge surface area offer a desirable plain to absorb small molecules including growth factors, cytokines and hormones, which play an pivotal role in regulation of stem cells specification.^[65]

Since CNTs have plenty of unique properties that are suitable for designing artificial scaffolds for stem cells therapy. Yu et al. employed CNTs to decorated type I collagen hydrogels and the obtained scaffolds could improve the cardiac cell functions.^[103] Khademhosseini et al. developed conductive fiber network hydrogel using hyaluronic acid and nucleic acids functionalized CNT to investigate cardiac tissue engineering.^[104] He fabricated multilayered CNT nanocomposites utilizing layer by layer (LbL) assembly on the substrate of quartz with positively charged poly(dimethyldiallylammonium chloride) and negatively charged MWCNTs (Figure 9a).^[105] The CNT-multilayered nanocomposites could regulate neural stem cells (NSCs) adherence, migration, proliferation and lineage specification. The interactions between CNT multilayers and NSCs could trigger downstream signaling events and activate focal adhesion kinase during the process of synapse formation and neural genesis. CNT nanomaterials offered new insights to modulate stem cell behavior for the future application in neural fields. Khademhosseini et al. incorporated CNT into gelatin methacrylate (GelMA) to form photo-cross-linkable hydrogels and then seeded with engineered functional cardiac patches (Figure 9b).^[100] The CNTs decorated thin film hydrogels with fibrous networks structures and interconnected pores looks analogous to purkinje fiber on heart muscle tissue. The CNTs endowed conductive nanofibrous network structures played a pivotal role in the improvement of cardiac cell adherence, interaction and organization. The engagement of CNTs into biocompatible scaffolds

could improve organization, electroactivity, and mechanical integrity, which is significant in multifunctional cardiac, neural or other muscle scaffolds for in vitro studies or future tissue therapy.

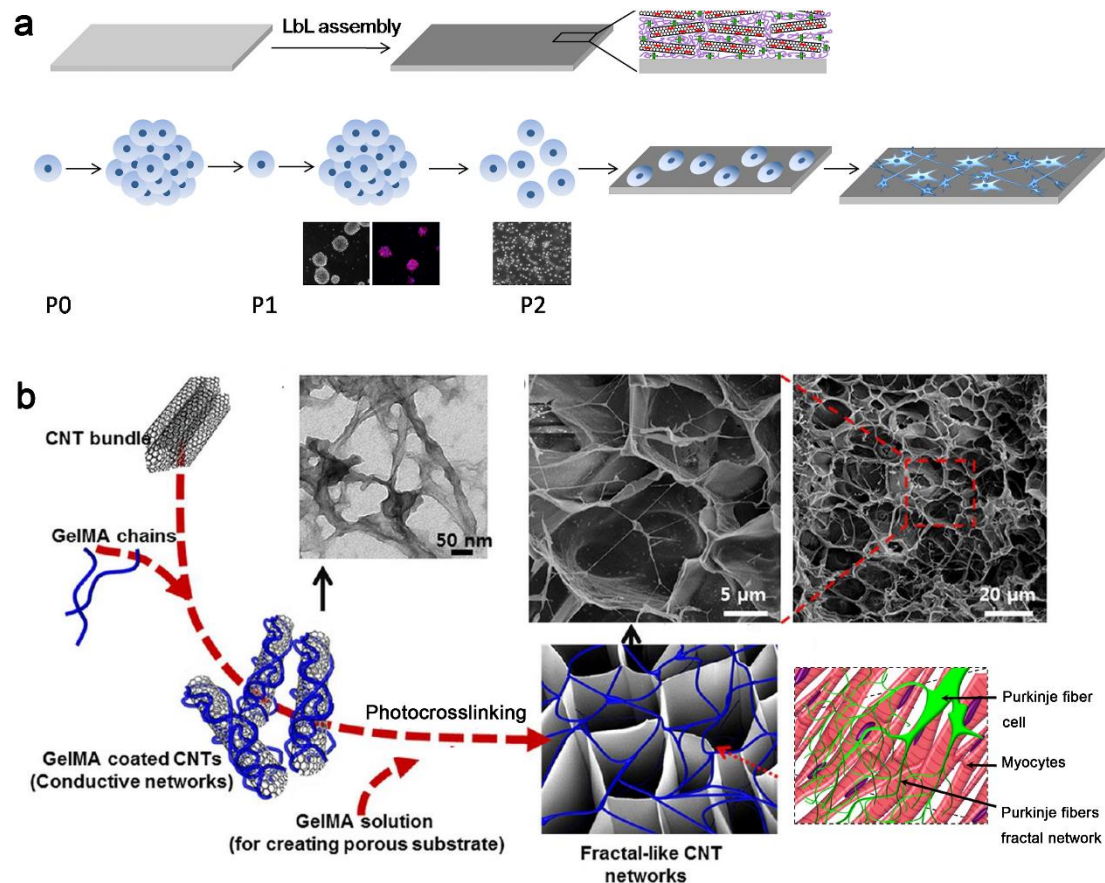


Figure 9. a) Schematic diagram of the NSC differentiation on CNT-multilayered substrates. Neural stem cells were cultured on the CNT-multilayered substrates in the differentiation medium. Reprinted from Ref.^[105] with kind permission from the Elsevier. b) Preparation procedure of fractal-like CNT networks embedded in GelMA hydrogel. Structural images of GelMA-coated CNTs and porous surfaces of CNT-GelMA thin film. Schematic diagram showing the purkinje fiber networks on the surface of the heart muscle fibers. Reprinted from Ref.^[100] with kind permission from the ACS Publications.

1.3.2. Graphene

Graphene made up with sp^2 -bonded carbon atoms in a single layer sheet form, and the common preparation methods include chemical vapor deposition or mechanical/chemical exfoliation of graphite. The graphene group includes chemical

derivatives of graphene, graphene oxide (GO) and reduced graphene oxide (rGO). GO is a highly oxidized product through cruel oxidation of graphite by Hummers method. GO is a highly oxidized product of graphene prepared by harsh oxidation of graphite and rGO is obtained after chemical/thermal reduction of GO. The graphene family dimensional size variety from 10 nm to 20 μm , which have been extensively reported in constructing ECM-mimicking scaffolds serving as physical cues in regulating stem cell properties owing to their controllable nano-topography, high stiffness, and conductivity.^[106, 107] Benefiting from its excellent binding properties to biomolecules, graphene played a pivotal role in concentrating soluble chemical cues (bioactive molecules, nutrients, cytokines and growth factors), which is significant for stem cell growth and differentiation.^[106] The sp^2 graphitic structures and corresponding large surface area provide an excellent platform for grafting of bioactive molecules as well, which is effective for stem cell fate specification with multiple chemical stimuli.^[108]

Deng et al. developed a kind of graphene/Laponite (GL) hybrid materials in a powder (GL-powder) form and a scaffold (GL-scaffold) form and to investigate MSCs towards osteogenic differentiation (Figure 10a).^[109] The GL-scaffold could improve MSCs' homogenous adherence, growth and further proliferation. Moreover, by crushing the GL-scaffold, the obtained GL-powders could improve MSCs towards osteogenic differentiation by increasing the alkaline phosphatase (ALP) activity, promoting calcium mineral deposits and upregulating the osteogenic marker protein for example osteocalcin, osteopontin, Sox9 and Runx2. The lateral MSCs and GL-powder implantation experiment *in vivo* proved that graphene/Laponite could promote the bone formation, which is quite promising in bone tissue engineering therapy. Chen et al. prepared a graphene based conductive and biocompatible scaffolds to comprehensively enhance the differentiation and maturation human iPSC developed cardiomyocytes on large scale (Figure 10b).^[110] Results suggested that graphene sheets could remarkably promote cardiomyocytes differentiation by promoting the electrophysiological or Ca^{2+} handling property, enhancing the conduction velocity and contractile protein organization degree. Through providing electrically active substrates, the graphene-

based scaffolds could facilitate the electrical communication and accelerate differentiation and maturation of hiPSCs towards functional cardiomyocyte, which is a convenient and easy method for homogeneous cardiomyocytes regeneration with surpassing electrophysiological functions and more powerful contractile properties without exogenous molecular treatments or applying external stimulation, providing promising future for cardiac tissue engineering.

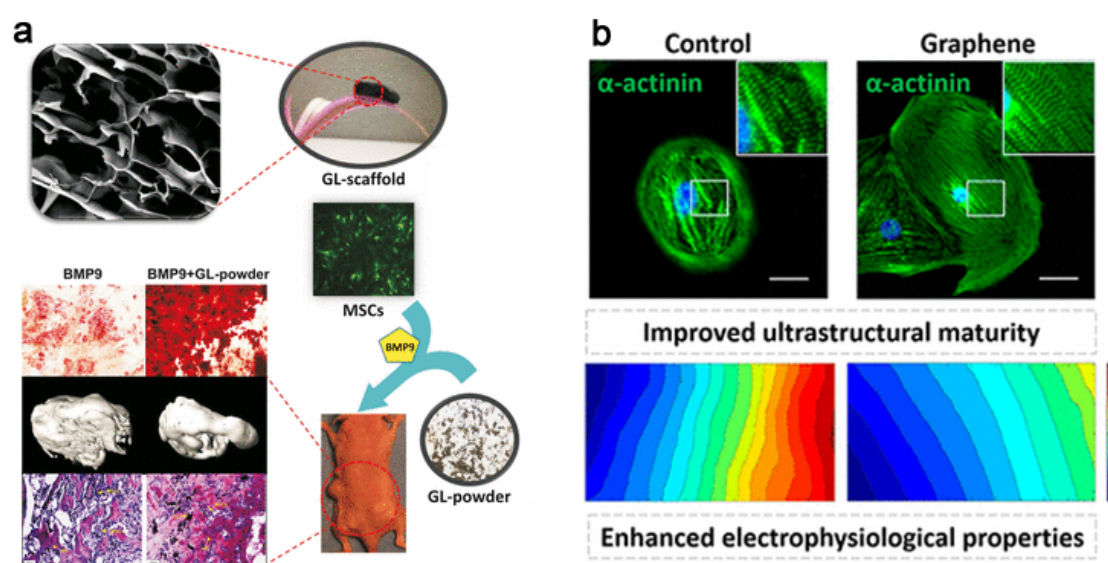


Figure 10. a) novel hybrid materials consisting of gelatin-derived graphene and silicate nanosheets of Laponite are biocompatible and promote osteogenic differentiation of MSCs. Reprinted from Ref.^[109] with kind permission from the ACS Publications. b) Schematic diagram of the graphene sheet and hiPSCs on graphene sheet. Graphene substrate improved cardiomyocyte phenotype. Graphene substrate increased action potential conduction and Ca^{2+} handling properties. Reprinted from Ref.^[110] with kind permission from the ACS Publications.

1.3.3. Carbon Dots

Carbon dots (CDs) combines a series of unique properties, such as low cost, large surface area, surface modification flexibility, high stiffness, and biostability, which could be utilized to affect stem cell growth and differentiation.^[111-113] Moreover, surface modification of carbon dots could change and control the physicochemical properties.

Shao et al. developed CDs and proved to improve osteogenic differentiation of MSCs with increased osteoblast gene markers expression, which suggests that CDs could exert positive effects on bone formation and regeneration.^[114] The metal-organic frameworks derived carbon dots have large surface area, high porosity, particular nanostructures, which could facilitate the adsorption of large amount of small molecules and proteins, thus promoting the interactions between the material and cell membrane.^[115, 116]

Karasik et al. developed a nitrogen-doped carbon dots (NCDs) conjugated with hydroxyapatite (HA) nanoparticles to investigate their effects on osteogenic differentiation potential, which were tested on a zebrafish jawbone model (Figure 11a).^[117] Results suggested that NCD–HA nanoparticles were highly dispersible, stable, and uniformly sized, which were further proved to induce osteoblast proliferation and differentiation. Meanwhile, the bone regenerated very well after NCD–HA nanoparticles implanted in the zebrafish jawbone model, which proved the modified carbon dots nanoparticles were promising candidates for the designing of scaffolds in bone tissue regeneration. Zhang et al. prepared a stable and functional nanovector by conjugating CDs with sulfosuccinimidyl-4-(N-maleimidomethyl) cyclohexane-1-carboxylate (SMCC), a protein crosslinker. The CDs based nanovector is positively charged, well dispersed and exhibited intense fluorescence, which is encouraging to bind and deliver small interfering RNA (Figure 11b).^[118] Results suggested that synthesized CD-SMCC could interfere and transfer the silenced tumor necrosis factor α (TNF α), which played a pivotal role in enhancing MSCs chondrogenesis and cartilage *in vivo* tissue engineering.

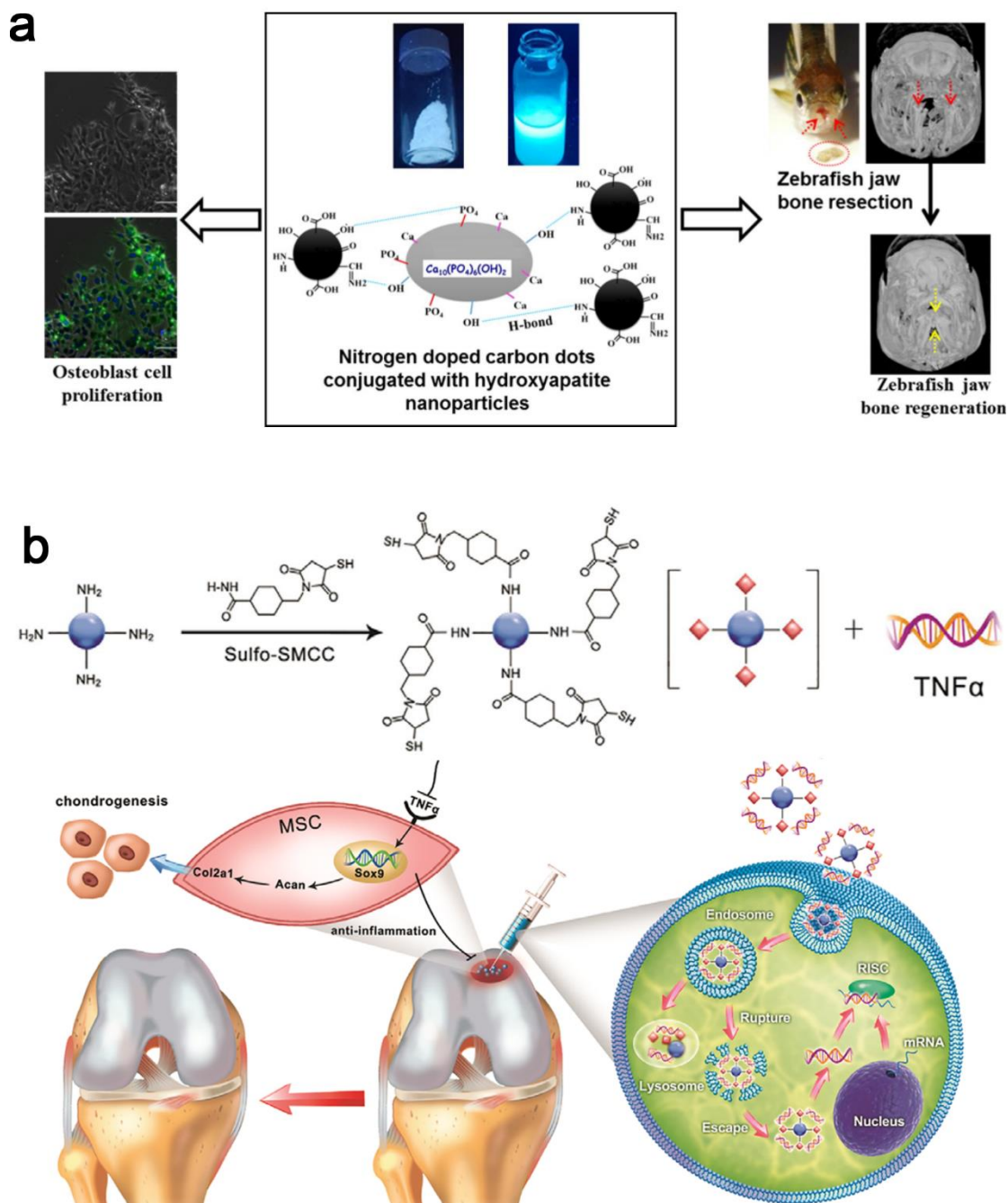


Figure 11. a) Nitrogen-doped carbon dots (NCDs) conjugated with hydroxyapatite (HA) nanoparticles could induce osteoblast differentiation and proliferation *in vivo* and promote bone regeneration ability in a ZF jawbone regeneration model. Reprinted from Ref.^[117] with kind permission from the ACS Publications. b) Schematic illustration of the formation of carbon dot (CD)-succinimidyl-4-(N-maleimidomethyl) cyclohexane-1-carboxylate-silenced TNF α complexes and the CD-based nanocarrier for gene delivery and real-time monitoring of cellular trafficking *in vitro* and *in vivo* for

enhancing cartilage repair. Reprinted from Ref.^[118] with kind permission from the WILEY-VCH.

1.4. The Design of Bioactive Nanostructured Fibrous Stem Cell Scaffolds

The physical and chemical property of scaffolds is critical for stem cell functions including spreading, migration, proliferation and differentiation. Once cells seeded, the derived cells were immersed in countless molecules and paracrine signals to intensify reactions that regulate the cell fate.^[119] The general achievement of stem cells development highly depends on the biocompatible scaffolds characteristics, for example mechanical integrity, cell-recognizable surface chemistries, material degradation, the optimal fluid transport and bioactive molecules delivery, which would further determine cell adhesion, nutrient/waste exchange, protein synthesis, intracellular matrix construction and cell differentiation eventually. Thus, the design and modification of stem cells scaffolds is meaningful and critical for cells transplantation *in vivo* and the tissue repair/regeneration processes. Among a variety of scaffolds modification methods, the scaffolds surface modification and nanoscale element design could adjust to critical parameters for stem cells culture.

The cell adhesion on scaffolds is indirect via a surface layer of coated proteins, and surface hydrophilicity/hydrophobicity is determinant for the coated proteins amount. Thus, the scaffold surface treatments could regulate cells adherence efficiently and conveniently compared to bulk modification.^[120] Plasma treatment in methane, oxygen, nitrogen, air or other gases could endow the scaffold surface with charged groups. Chemical etching, for example HNO₃ on poly(ether urethane) or NaOH on PLGA, γ - or UV-irradiation and peroxide or ozone oxidation could bring in reactive groups as well.^[121-123] Since brutal treatment could lead to polymer degradation and the longtime effects on surface may not be permanent, surface grafting of charged or hydrophilic polymers could be a suitable choice.^[124] Methods focusing on the physical interaction between the serum protein and polymer surfaces are non-specified, more selected effects could be exerted on cells by covalent grafting and conjugating specific

proteins on scaffolds.^[125, 126] Additionally, the LBL method is particularly appropriate for irregularly shaped structures and proteins coating where conventional technique does not fit.^[105] Therefore, surface treatments are mainly focusing on proteins adsorption or conjugation so that they can largely retain their normal functionality and improve stem cells adhesion and proliferation.

Cells are resident in a complicated microenvironment full of physicochemical and topographical cues scales from nanometers to micrometers. The design of nanoscale elements on scaffolds offers the specific binding sites for cytokines and growth factors, which is significant for further cell membrane communication and adhesion.^[127] When cells were seeded on a scaffold, they stretch or withdraw filopodia full of integrin receptors, actively feel the surrounding microenvironment for movement. In order to prove that the variety of nanoscale surface properties could affect stem cells phenotype or activity response directly, numerous researches have been done in incorporating nanometer range features into ECM mimicking stem cell scaffolds.^[128-130] Carbon nanomaterials could be used as nanoscale patterning for fabrication of ECM mimicking stem cell scaffolds, which offers multiple anchoring sites for receptors interaction between multimeric proteins and cells.

2. Scientific Goals

The stem cell culture ECM is complex and dynamic, which provides physical and chemical stimuli to modulate the stem cell adherence, migration, growth, proliferation and differentiation apart from offering mechanical scaffolding and anchorage spots in tissue engineering.^[63, 131] The general achievement of stem cells development highly depends on biocompatible scaffolds characteristics, which could determine cell adhesion, nutrient/waste exchange, protein synthesis, intracellular matrix construction and cell differentiation eventually. The physical and chemical property of scaffolds offer the seeded cells with countless molecules and paracrine signals to intensify reactions that regulate the cell fate.^[132, 133] ^[134] Physical cues mainly include stiffness, nanostructured morphologies, and surfaces charges and chemical cues contain growth factors, hormones and small chemicals.^[135, 136] Thus, the design and modification of stem cells scaffolds combined with chemical and physical cues is meaningful and critical for cells transplantation *in vivo* and the tissue repair/regeneration processes.^[137] The scientific goals of this thesis are mainly to integrate the physical and chemical cues through the incorporation of nanostructured carbon materials into the scaffolds, which is quite promising and interesting in the investigation of interaction between stem cell behavior and ECM environment.

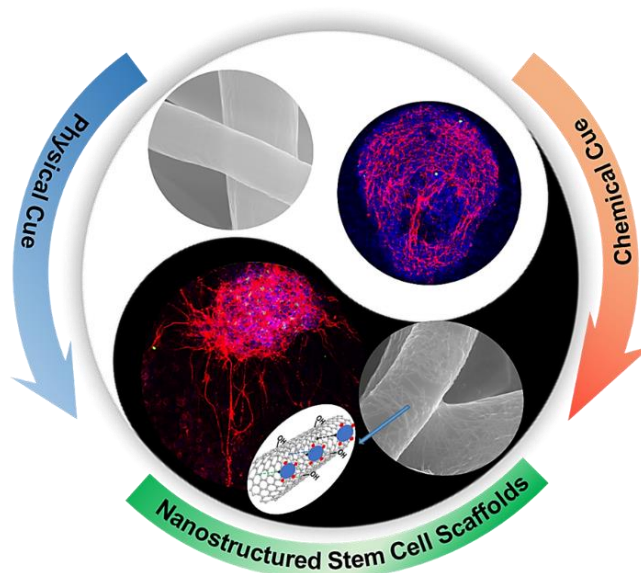
Due to the nanotopography, high stiffness and other physical property, carbon nanomaterials serve as great nanoscale candidate for scaffolds modification in stem cells culture.^[138] However, carbon nanotubes (CNT) could not well dispersed in water, one of the scientific goals is to prepare a good dispersion of CNT with polymers or dispersants. In our first project, the CNTs are functionalized by biocompatible and multivalent hyperbranched polyglycerol sulfate (hPGS) noncovalently.^[126] After air plasma treatment of electrospun fibrous polycaprolactone (PCL) scaffolds, CNT-HPGS nano-dispersant were coated on the surface of PCL fibers to combine the chemical and physical cues. Thus, the promoted protein adhesion property of CNT-HPGS contribute to the stem cells growth microenvironment and provide a novel method to construct functional scaffolds for stem therapy research.

Since the non-covalently modified carbon nano-dispersions were not stable in the first project, the hyperbranched polyglycerol sulfate was covalently grafted onto the graphene oxide (GO) nanosheet in our second project. GO 2D platforms are full of carboxyl, hydroxyl and epoxide groups, which could promote protein adhesion through covalent, electrostatic, and hydrogen bonding.^[106, 139] The sp^2 graphitic structures and large surface area are quite suitable for grafting bioactive molecules. The physical property of graphene oxide and chemical property of HPGS were combined to mediate the IPS cells growth and differentiation.^[1, 37, 140, 141] Then the 2D nanosheets functionalized nanofibrous scaffolds were applied to mediate the proliferation, lineage specification, and differentiation of IPS cells. Results suggest that coated scaffolds could promote IPS neural differentiation and maturity. The scientific goal of this study is to address the stability of the dispersion and promote the stem cell lineage specification maturity, which integrate the chemical and physical cues to facilitate the targeted differentiation of IPS cells. Meanwhile, it presents a novel pathway in designing carbon nanomaterials composites for in vitro regenerative therapies.

In the third project, the physical cues of carbon nanomaterials were motivated by the MOF-derived nanocarbons.^[142] The porous carbon nanostructure could promote the adhesion of proteins and growth factors, moreover, the caging property of the carbon nanostructure achieves the gradual release of chemical cues, which provide a novel pathway for activation of signal pathways and guiding the stem cell differentiation process.^[116] The scientific goal of this study is to design multifunctional stem cell scaffolds that simultaneously enhance osteogenic and anti-infective capabilities.

3. Publications

3.1. A Multivalent Polyanion-Dispersed Carbon Nanotube towards Highly Bioactive Nanostructured Fibrous Stem Cell Scaffolds



Yi Xia, Shuang Li, Chuanxiong Nie, Jianguang Zhang, Suqiong Zhou, Hua Yang, Mingjun Li, Wenzhong Li, Chong Cheng* and Rainer Haag*

Appl. Mater. Today 2019, 16, 518–528

DOI: <https://doi.org/10.1016/j.apmt.2019.07.006>

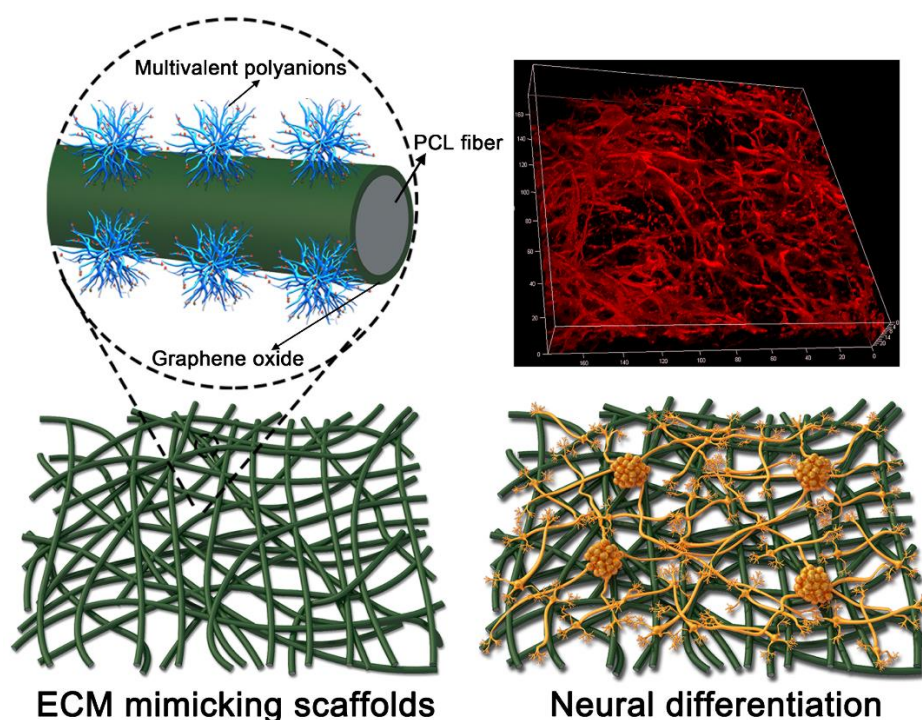
<https://www.sciencedirect.com/science/article/pii/S2352940719305487>

Author contributions:

Yi Xia performed the main experiments, and wrote the manuscript.

Shuang Li conducted the XPS and analyze the data. Chuanxiong Nie conducted the TEM and analyze the data. Yi Xia, Jianguang Zhang, Suqiong Zhou, and Mingjun Li performed the IPS cell experiments. Hua Yang did the modeling and image processing using MATLAB. Yi Xia, Chong Cheng, and Rainer Haag co-wrote the manuscript. Chong Cheng, Wenzhong Li, and Rainer Haag conceived and supervised the project.

3.2. Multivalent Polyanionic 2D Nanosheets Functionalized Nanofibrous Stem Cell-based Neural Scaffolds



Yi Xia, Hua Yang, Shuang Li, Suqiong Zhou, Liyun Wang, Chong Cheng,* and Rainer Haag*

In preparation of submission

Author contributions:

Yi Xia performed the main experiments, and wrote the manuscript.

Hua Yang did the modeling and image processing with MATLAB and data processing with Fuji. Shuang Li and Liyun Wang conducted the XPS and TEM and analyze the data. Suqiong Zhou helped performed the IPS cell experiments. Chong Cheng and Rainer Haag conceived and supervised the project.

Multivalent Polyanionic 2D Nanosheets Functionalized Nanofibrous Stem Cell-based Neural Scaffolds

Yi Xia, Hua Yang, Shuang Li, Suqiong Zhou, Liyun Wang, Chong Cheng, and Rainer Haag**

Keywords

Multivalent polyanions; bio-adhesive graphene nanostructures; nanofibrous scaffolds; stem cells regeneration; biocompatibility and neural differentiation

Abstract

Because developed neural cells are no longer regenerative and proliferative, achieving neural regenerations by using induced pluripotent stem cells (IPS cells) for nerve diseases have recently attracted much attention. Since the IPS cells' growth and differentiation can be manipulated by different physical and chemicals cues, scaffolds combining the beneficial nanostructures and extracellular matrix may become an ideal interface to promote IPS cells' neural differentiation. In this work, a biocompatible and multivalent polyanion, hyperbranched polyglycerol sulfate, was used to modify the graphene oxide to obtain bio-adhesive 2D nanosheets. Then the 2D nanosheets-functionalized nanofibrous scaffolds were applied to mediate the proliferation, lineage specification, and differentiation of IPS cells. Our results suggest that the modified scaffolds could improve the adhesion and proliferation of IPS cells combined with high efficiency in maintaining their stemness. During the neural differentiation process, the scaffolds could promote neural differentiation and their maturity, meanwhile decreasing the lineage specification towards astrocyte. Overall, this study provides new multivalent/bio-adhesive nanofibrous scaffolds that integrating the chemical and physical cues to facilitate the targeted neural differentiation of IPS cells. It shows a novel pathway for the fabrication of carbon nanomaterials composites in regenerative therapies as well.

Introduction

In order to uncover disease mechanisms and develop therapeutic strategies for brain damages and related neurological diseases, developing efficient neural models is significant and urgent.^[2, 145-147] As developed neural cells are no longer regenerative

and proliferative cells, it is necessary to develop an induced cell line for the regeneration of neural models. Induced pluripotent stem cells (IPS cells) are frequently used while obviating the necessity to obtain the tissue from the human brain or take the ethical issues destroying embryos.^[148-150] Moreover, the IPS cells are so sensitive that the cell behavior and cell differentiation fate could easily be affected by the dynamic microenvironment of the extracellular matrix (ECM).^[151, 152] Therefore, stem cell niches and microenvironment mimicking bio-scaffolds would facilitate the large scale of stem cells' production and specially differentiated cell types preparation.^[153-156] ECM-mimicking bio-scaffolds apply the effect on cell behavior mainly through physical cues (i.e., stiffness, nanostructured morphologies, charged surfaces, and magnetic field),^[157-161] and chemical cues (i.e., small chemicals, growth factors, and hormones).^[153, 162, 163] Indeed, both physical and chemical cues can efficiently influence IPS cell's functionalities, including regulation of cell adhesion, proliferation, and differentiation. For instance, the change of physical cues could affect cell-cell interactions and trigger the membrane protein activations. In the meantime, the chemical cues could lead to different integrin activations of cell membranes. The integration of chemical and physical cues utilizing nanostructured scaffolds is fascinating.^[164-167] However, there is only limited knowledge about the regulation of the IPS cells' interfacial interactions and the effect on their neural differentiation.

Carbon nanomaterials have been extensively reported in constructing ECM-mimicking scaffolds serving as physical cues in regulating stem cell properties owing to their controllable nano-topography, high stiffness, and conductivity.^[107, 168-171] Among diverse carbon nanomaterials, graphene oxide (GO) 2D nanosheets are nanomaterials enriched with carboxyl, hydroxyl and epoxide groups on the basal platforms, which is significant in improving interactions between GO and proteins via covalent, electrostatic, and hydrogen bonding.^[152, 168] Benefiting from its excellent binding properties to biomolecules, GO played a pivotal role in concentrating soluble chemical cues (growth factors or cytokines, nutrients, and bioactive molecules), which is significant for stem cell growth and differentiation.^[141] The sp^2 graphitic structures and corresponding large surface area provide an excellent platform for adsorbing bioactive molecules as well, which is sufficient for stem cell fate specification with multiple chemical stimuli.^[172, 173] However, current GO-based neural scaffolds are limited to 2D flat interfaces or nanofibrous composites, and these constructed scaffolds

have shown promising promotion of neural differentiation. Nevertheless, the maintaining of stemness, promotion of cellular adhesion, and inhibition of differentiated astrocyte are quite challenging for these currently designed GO-based neural scaffolds. The heparin-mimicking polyanion, hyperbranched polyglycerol sulfates (HPGS), exhibits multivalent, biocompatible, and bio-adhesive polyether backbones. HPGS can serve as a chemical cue for biomedical scaffolds, exhibits outstanding cell-adhesive activities and attachment property towards proteins in the regulation of cell growth and proliferation.^[174, 175] Thus, it is believed that the HPGS functionalized GO-derived scaffolds may provide ideal physical and chemical cues to mediate IPS-cells' stemness and achieve highly efficient neural differentiation.^[37, 153, 172]

In this work, we used the multivalent, biocompatible, and bio-adhesive HPGS to modify 2D GO nanosheets to fabricate nanostructured fibrous neural scaffolds with combined physical and chemical cues to mediate the IPS cells' proliferation and lineage specification. First, the GO-HPGS nanosheets were prepared by covalently grafting of HPGS on GO. Then 2D nanosheets were coated onto the plasma-treated electrospun polycaprolactone (PCL) nanofibrous scaffolds, namely, PCL-GO-HPGS. Our results suggest that the GO-HPGS modified scaffolds could improve the adhesion and proliferation of IPS cells combined with high efficiency in maintaining their stemness. During the neural differentiation process, the scaffolds could promote neural differentiation and their maturity and meanwhile decrease the lineage specification towards astrocyte. Overall, this study provides a new multivalent/bioadhesive nanofibrous scaffolds for neural regeneration, which integrate the chemical and physical cues to facilitate the targeted differentiation of IPS cells. Furthermore, our design on 2D nanosheet functionalized nanofibrous stem cell-based scaffolds may also provide a new pathway for the fabrication of carbon nanomaterials composites in regenerative therapies as well.

Results and Discussion

Synthesis and characterization of the GO-HPGS nanomaterials

The HPGS, a extracellular-matrix-/heparin-mimetic structure, shows intense multivalent interactions with different proteins and biomolecules, which is crucial in a series of the process, including the adhesion of proteins, recognition of membranes, and

signaling processes in cells.^[176-179] To improve the carbon-to-substrate and carbon-to-carbon interactions, HPGS was directly grafted onto GO nanosheets. Thus, it is believed that the HPGS-modified GO could be used as bio-adhesive and biocompatible nanosheets for the construction of ECM-mimicking scaffolds. As shown in Figure 1a, the azides-functionalized hyperbranched polyglycerol (HPG-N₃, ~11% N₃ substitute to OH groups) was grafted onto GO through covalent conjugations between sp² carbon bonds on GO and the azide group on HPG-N₃ via nitrene cycloaddition reaction at 120 °C. The hydrophobic interactions and hydrogen bonding between the HPG-N₃ and planar GO could significantly improve the amount of grafting HPG on GO. The azide-based nitrene cycloaddition reaction offers an extremely fast and stable method for scalable HPG anchoring.

Then, GO-HPG was sulfated to alter antifouling HPG into multivalent, biocompatible, and bioadhesive HPGS, specifically, GO-HPGS nanosheets. As shown in Figure 1a, the GO-HPGS nanosheets were sulfated from the GO-HPG through the SO₃-pyridine complex. The TEM images, as shown in Figure 1b, suggest the 2D sheet-structure of GO-HPGS, indicating that the high surface/volume ratio property and 2D structure of GO were well maintained. Figure 1c shows the element distribution of the GO-HPGS with high-angle annular dark-field scanning transmission electron microscopy (HAADF-STEM). C, O, S, and Na elements were uniformly distributed on the 2D nanosheet according to the HAADF-STEM image and elemental mapping, which suggests that HPGS are homogeneously grafted onto GO. Figure 1d exhibits the atomic force microscope (AFM) picture for pristine GO-HPGS on freshly cleaved mica. The height distribution in Figure 1e suggests the difference between the two arrows was about 4.11 nm. Figure 1f suggests the calculated thickness distribution of GO-HPGS from 25 nanosheets, and each thickness ranges from 3.9 nm to 4.3 nm. Meanwhile, the calculated thickness distribution of GO (Figure S1, 0.9 nm to 1.2 nm) and GO-HPG (Figure S2, 2.3 nm to 2.5 nm) from 25 nanosheets, which verifies the uniform grafting of HPGS on GO nanosheet.

The Fourier-transform infrared spectroscopy (FTIR) (Figure S3) peaks at 3401.8 (-OH), 3070.1, 2877.2 (-CH-, -CH₂-), 2106.1 (-N₃), 1716.3, 1611.2, 1194.6 (C-O), 1022.0, 929.5 (-SO₃-) cm⁻¹ verified the chemical structure of GO-HPGS. GO-HPGS was further characterized by X-ray photoelectron spectroscopy (XPS, Figure 1g-1i). Figure 1g shows the existence of sulfur element (sulfate groups) and nitrogen element

(conjugated azide) on GO-HPGS nanosheets, which verified the successful grafting of HPG-N₃ on the planar GO. The high-resolution spectra of C1s (Figure 1h) for GO-HPGS indicated the existence of C=C, C-C, C-N, C-O, and C=O peaks. The high-resolution N1s spectra (Figure 1i) show three major nitrogen peaks including 401.7 eV (=N⁺= in residual N₃ groups), 400.8 eV (N= and =N⁻ in residual N₃ groups), and 399.7 eV (cycloaddition-formed N-graphene conjugation).

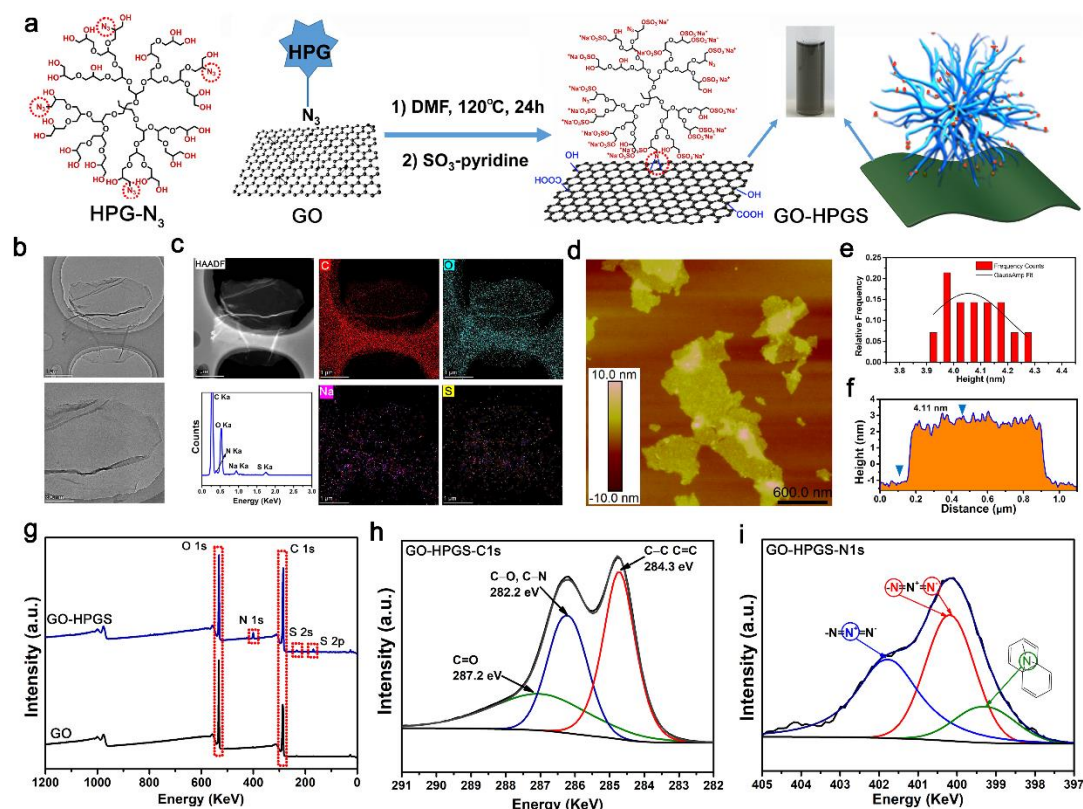


Figure 1. (a) Scheme of the preparation process of 2D nanosheets by utilizing the GO and HPG-azide through nitrene cycloaddition reaction. (b) Typical TEM image of the prepared GO-HPGS nanosheets at different magnifications. (c) HAADF-STEM image, EDS curves, and corresponding elemental mapping of the GO-HPGS nanosheets, which revealed the distribution of C, O, Na, and S. (d) Representative AFM images of GO-HPGS. (e) The calculated thickness distribution of GO-HPGS from 25 nanosheets. Each thickness ranged from 3.9 nm to 4.3 nm, which indicated the obtained GO-HPGS nanosheets were purely single-layer products. (f) The cross-section analyses of GO-HPGS and the height difference between the two arrows were about 4.11 nm. (g) XPS survey scanning spectra for the GO and GO-HPGS, which is corresponding to sulfur and nitrogen. The high-resolution XPS for (h) C1s spectra and (i) N1s spectra for GO-HPGS.

As an amphiphilic carbon nanomaterial, GO is quite promising for functional nerve repair.^[168] GO has a high adsorption ability on growth factors and diverse nutrition proteins through the provision of beneficial chemical cues, which could improve the attachment and spread of IPS cells.^[141] Moreover, due to the hierarchical structures of fibrous neural scaffolds on the microscale and nanoscale, the fibrous scaffolds provide physical cues for neural tissues to adhere and grow. In this work, with the coating of GO-HPGS nanosheets, the nanostructured fibrous scaffold was constructed to offer an appropriate microenvironment for IPS cells' survival and differentiation. The polycaprolactone (PCL) was chosen as the electrospun matrix to build the original fibrous scaffold due to its well-established biocompatible and degradable property, which is pivotal for biomedical applications. Figure 2a exhibits that a syringe with a metal needle was filled with PCL solution, after being applied with a 16 kV high voltage; the solution was split into fibers and fall onto a rotating drum collector. Then, the fibrous scaffolds were treated with 1 min of O₂ plasma to generate radicals on the fiber's surface. Then 1 mg/mL HPGS, GO, and GO-HPGS aqueous solutions were dipped into the plasma-treated fiber mats to prepare the PCL-HPGS, PCL-GO, and PCL-GO-HPGS scaffolds, respectively.

Figure 2b shows the morphologies of the scaffolds under scanning electron microscopy (SEM). The electrospun PCL fiber mats (~50 μm in thickness) composed of crossing fibers with a diameter of around 1 μm. According to the amplified SEM image, the GO and GO-HPGS nanosheets-coated samples had corrugations on the fiber's surface compared with the smooth surface on original PCL fiber. This suggested that the GO and GO-HPGS 2D thin-films were tightly wrapped around the fiber's surface, and a 3D nanofibrous structure could be well-maintained. The energy dispersive spectrometer data (EDS) and element mapping on PCL-GO-HPGS (Figure 2c and Figure S4) indicated the existence of sulfur due to the coating of GO-HPGS. The FTIR data in Figure 2d gives the characteristic peaks for different samples, respectively. There are -OH and -SO₃- peaks on PCL-HPGS, -OH peaks on PCL-GO, and -OH, -N₃, and -SO₃- peaks on PCL-GO-HPGS, which verified the successful coating of the above samples. The water contact angle (Figure 2e) on pure PCL is around 129°. After coating with different samples, the surface was transferred to hydrophilic. As shown in Figure 2f and Table 1, XPS has been further characterized to verify the successful coating of 2D nanosheets onto PCL nanofibers. According to the

XPS survey scanning spectra in Figure 2f, there exists abundant sulfur element on the PCL-HPGS fibers, and nitrogen and sulfur elements on PCL-GO-HPGS fibers, thus suggesting that HPGS and GO-HPGS nanosheets were coated onto PCL fiber, respectively. As shown in Figure 2g and 2i, the contents of element N1s on samples (after immersion in a cell culture medium) increased compared to that in Figure 2f and 2h. Accordingly, it is indicated that these scaffolds could absorb molecules of amino acids based peptides or proteins from the cell culture media, which is critical for regulation and specification of IPS cells' growth and differentiation. After being coated with GO-HPGS nanosheets, the scaffolds exhibited much better absorption ability towards the amino acids based peptides/proteins and other small molecules, which could be further employed to manipulate the IPS cells' fates.

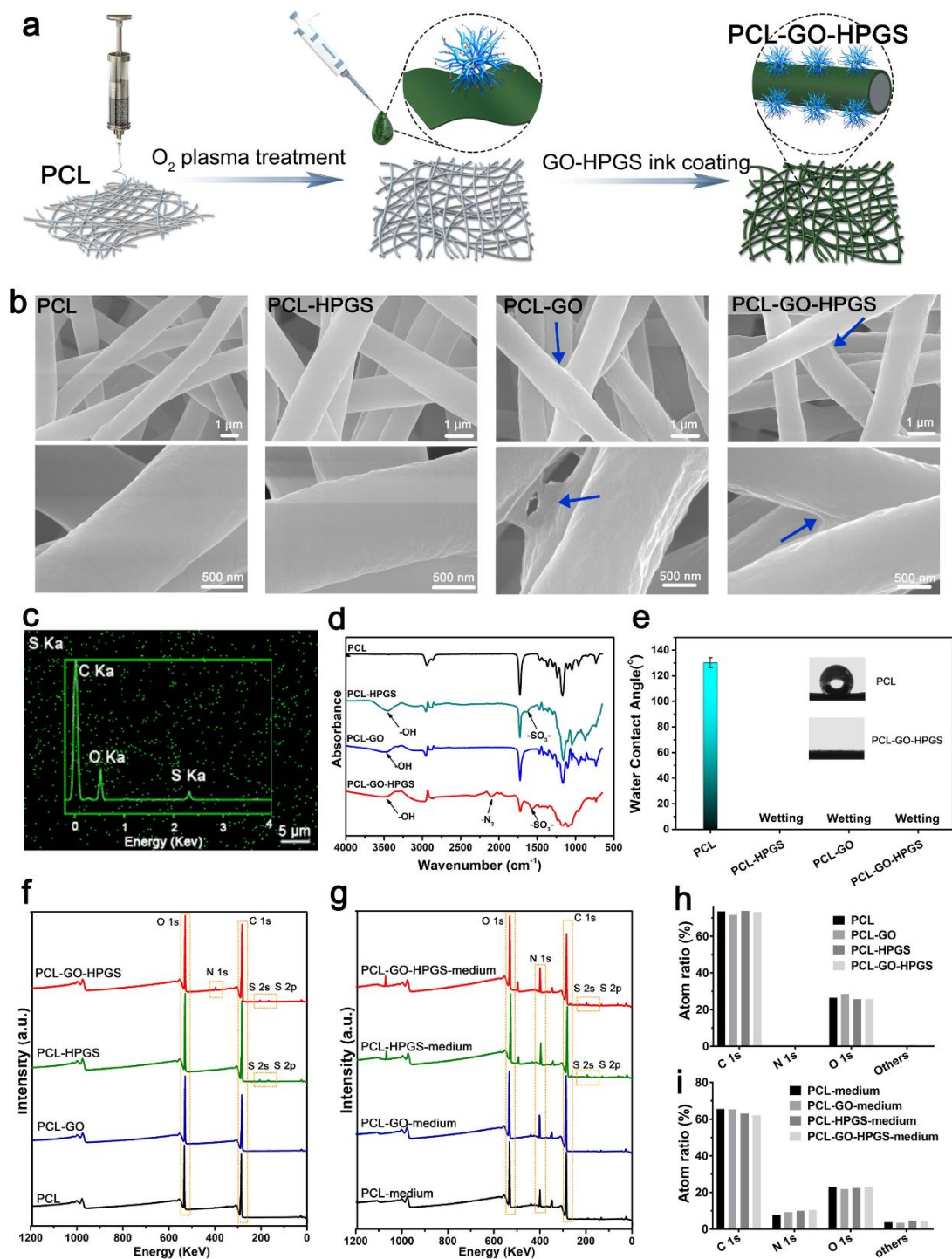


Figure 2. (a) Schematic images for the electrospinning process of PCL fibers and coating process of GO-HPGS nanosheets. (b) SEM pictures of PCL, PCL-HPGS, PCL-GO, and PCL-GO-HPGS samples. The nanosheets are marked with blue arrows. (c) The SEM element mapping and EDS curves of the S element on PCL-GO-HPGS. (d) FTIR spectra for bare and nanosheet-coated PCL fibrous scaffolds. (e) The average static water contact angle of bare, nanosheet-coated PCL fibrous scaffolds. XPS spectra for (f) fibrous scaffolds and (g) medium-immersed fibrous scaffolds. (h) The atom

percentages of C, N, O, and others on fibrous scaffolds and (i) medium-immersed fibrous scaffolds.

Table 1. The surface atomic percentage of the 2D nanosheet-coated PCL fibers with/without immersion of media. The data is according to XPS results.

| Sample | C1s (%) | O1s (%) | N1s (%) | S2p (%) | Others |
|--------------------|---------|---------|---------|---------|--------|
| PCL | 73.58 | 26.42 | - | - | - |
| PCL-HPGS | 74.11 | 25.64 | - | 0.24 | - |
| PCL-GO | 71.82 | 28.18 | - | - | - |
| PCL-GO-HPGS | 73.46 | 25.85 | 0.48 | 0.21 | - |
| PCL-medium | 64.50 | 22.99 | 8.78 | 0.34 | 3.39 |
| PCL-HPGS-medium | 65.37 | 21.84 | 9.32 | 0.40 | 3.07 |
| PCL-GO-medium | 63.30 | 22.41 | 9.98 | 0.31 | 4.00 |
| PCL-GO-HPGS-medium | 62.17 | 23.17 | 10.43 | 0.41 | 3.82 |

In order to evaluate whether the GO-HPGS nanosheets coated scaffolds are suitable for the biological application, the IPS cells were chosen to observe cell viability, adhesion, and proliferation, when grown on different nanofibrous scaffolds. Figure 3a shows the schematic image of cell adhesion properties on PCL and GO-HPGS nanosheet-coated scaffolds. After 1, 3, and 5 days of culture, the CCK-8 assay kit was utilized to evaluate the IPS cell proliferation rate on nanofibrous scaffolds (Figure 3b). After 5 days' culture, cells that proliferated on the GO-HPGS nanosheet-coated scaffolds were around 2-fold as much as that on PCL. The cells on PCL-GO and PCL-HPGS proliferated better than that on PCL as well, which indicated that the coating of GO and HPGS could both promote the proliferation of IPS cells. The LIVE/DEAD cell staining (Figure 3b) on PCL-GO-HPGS on day 3 shows homogeneous and interconnected cells, which was much better than the PCL-GO, PCL-HPGS, and bare PCL, indicating that GO and HPGS had synergistic improvement effect for the growth and proliferation of IPS cells. The lack of bioactive chemical ligands and relatively smooth fiber surface led to poor performance in cell adherence and growth on bare PCL. ECM preserve IPS cells in the niche or assists in starting signal transduction, while the surface coating of GO-HPGS concentrates soluble growth factors or cytokines, which regulates stem cell fate via immobilizing signaling molecules and creating cytokine gradients.^[154]

To investigate the interactions of GO-HPGS-coated fibers with IPS cells, the cell nuclear was stained with DAPI (blue), and the F-actin was stained with phalloidin (red), then the fluorescent images were observed with confocal microscopy. Figure 3d shows that cells grown on PCL-GO-HPGS had much more cell pseudopodium on the surface, which suggests more binding sites for IPS cells to adhere. 2D fractal dimensions (Df) are a dimensionless value in quantifying the complexity of spatial arrangement and complexity for the cell cytoskeleton. MATLAB was utilized to analyze the corresponding Df (Figure 3e) according to F-actin staining. The higher cytoskeleton complexity on GO-HPGS nanosheet-coated surface indicated that the cells have much more adhesion spots due to the corrugations on GO-coated nanotopography structure and the multivalent HPGS's protein binding affinity. The quantitative Df values of whole-cell spheroids on PCL-GO-HPGS were gradually bigger than that on PCL-GO, PGL-HPGS, and bare PCL (Figure 3h). Furthermore, correlative analysis of the cell area showed that the cell-spreading area on GO-HPGS nanosheets coated surface was larger than those on bare PCL, which suggests more anchoring opportunities for cells to facilitate cell motility and adhesion. In general, after the characterization of IPS cells' viability, proliferation, adhesion, and spreading, results indicated that the GO-HPGS-coated fibrous scaffolds achieved significant progress in providing an excellent environment for fragile IPS cells to survive.

During cell adhesion and spreading process, the rearrangement of the actin cytoskeleton would regulate cellular signaling pathways change.^[180] Increased cell spreading is frequently accompanied by yes associate protein (YAP) relocation and following YAP-responsive gene transcription activation.^[180] Its localization in nuclei results in IPS cells could promote cell proliferation.^[181, 182] Meanwhile, activated YAP nuclear translocation could mediate stemness maintenance in IPS cells.^[183, 184] Thus, we further investigated the YAP signal on PCL and PCL-GO-HPGS using immunofluorescence staining (Figure 3f, Figure S5). It is evident that YAP was located in the cytoplasm on PCL, however, more YAP signals exist in nucleus on PCL-GO-HPGS. The YAP nuclear/cytoplasm ratio in Figure 3i also suggests that more YAP is activated into nucleus on PCL-GO-HPGS, which proves that PCL-GO-HPGS could promote IPS cells proliferation and promote the stem cell stemness.

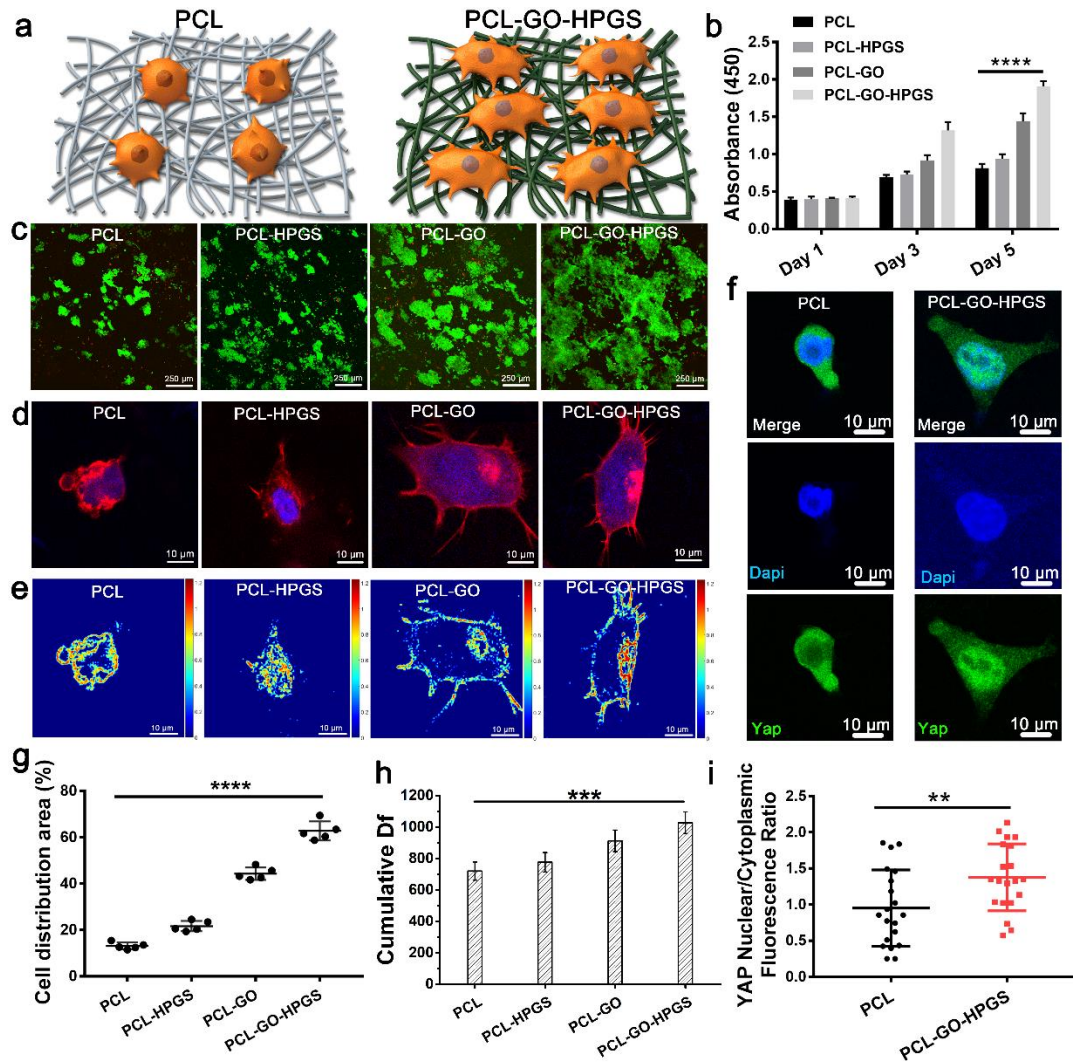


Figure 3. (a) Schematic diagram of cell adhesion on different surfaces. (b) CCK-8 test of IPS cell proliferation after 1, 3, and 5 days of culture on scaffolds. (c) Live-dead staining kit (green: live, red: dead) of IPS cells after 3 days of culture. (d) Single IPS cells' adherence to scaffolds after staining of DAPI (nuclei) and phalloidin (F-actin). (e) 2D fractal dimension (Df) distribution of the F-actin according to the F-actin staining in (d). (f) Immunofluorescence staining of the YAP signal in IPS cells after 3 days (YAP, green; DAPI, blue). (g) Quantitative analysis of the cell spreading area on different samples (n = 50). (h) Statistical quantification of cumulative Df value in every single cell (n = 10). (i) Statistical quantification of the YAP nuclear/cytoplasmic fluorescence intensity ratio; (n = 20). **** p < 0.0001, *** p < 0.001, ** p < 0.01, and * p < 0.05.

Nanog, Sox2, OCT4, and SSEA1 are transcription factors that are pivotal to preserve the stemness of undifferentiated IPS cells, which are involved in the regulation of self-renewal development and the determination of cell fate.^[183, 185] To better indicate the primitiveness and stemness of the reprogrammed cells, we observed the colonies

that stained positive for four primitive stem cell markers, Nanog, Sox2, OCT4, and SSEA1, on day 3 after being cultured in growth medium (Figure 4a). The colony, which was grown on PCL-GO-HPGS, was larger than that on bare PCL, which indicated that GO-HPGS could promote iPSC proliferation. The relative fluorescence intensity in Figure 4b and 4c suggests that PCL-GO-HPGS scaffolds could preserve the stemness very well and even slightly better than pure PCL. The stemness-marker fluorescence intensity of the colonies was consistent with the result of YAP nuclear translocation. The reason could be attributed to the PCL-GO-HPGS scaffold's good adsorption of protein (including the differentiation inhibitor) from the growth medium. Figure 4d and 4f represent the intensity distribution profiles of Nanog and Sox2 from the center to the edge of the cell colonies grown on PCL and PCL-GO-HPGS, Figure 4e and 4g represent OCT4 and SSEA1 on PCL and PCL-GO-HPGS, respectively. The colony radius for PCL is around 80 μm , and PCL is around 120 μm . Meanwhile, the fluorescence intensity at the edge of the colony was stronger than that in the center, which means that the outer cells could absorb more inhibitor from the medium and preserve the stemness better in the growth medium. The colony edge signal on GO-HPGS nanosheet-coated scaffolds was more extensive than that on bare PCL, indicating that GO-HPGS may have accumulated differentiation inhibitors from cell culture media to promote the stemness of IPS cells.

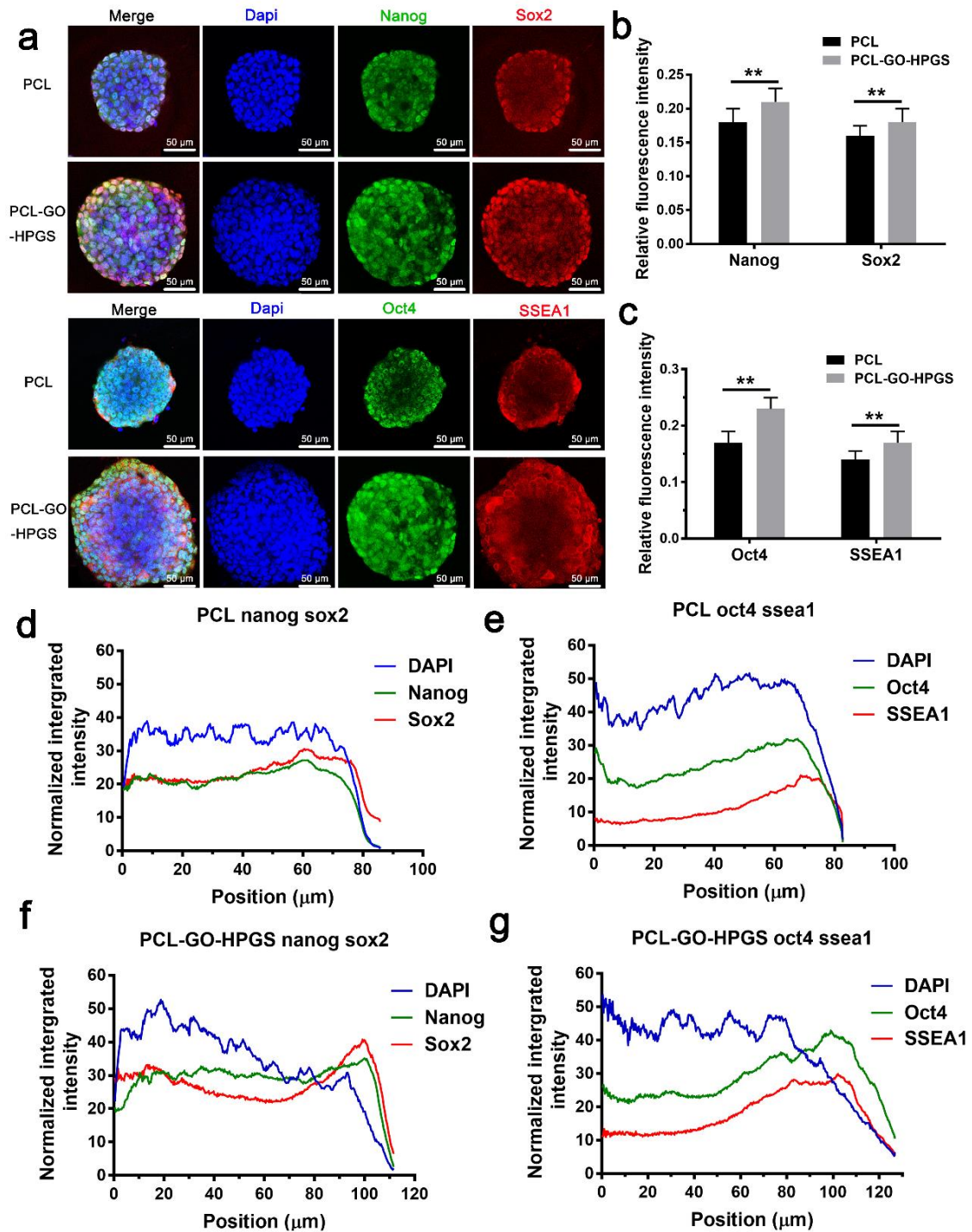


Figure 4. (a) Representative immunofluorescence staining of stemness markers: Nanog (green), Oct4 (green), Sox2 (red), and SSEA1 (red) for IPS cells on PCL-GO-HPGS and PCL. Quantitative analysis for grey intensity of immunofluorescence-stained images to get the average expressions of (b) Nanog and Sox2 (c) Oct4 and SSEA1. Respective intensity distribution profiles of (d) Nanog and Sox2, (e) Oct4 and SSEA1 from the center to the edge of the cell colonies grown on PCL, respectively. The respective intensity distribution profiles of (f) Nanog and Sox2, (g) Oct4 and SSEA1 from the center to the edge of cell colonies grown on PCL-GO-HPGS, respectively. ($n = 30$), *** $p < 0.001$, ** $p < 0.01$, and * $p < 0.05$.

As shown in Figure 5a, the embryonic body was prepared and seeded on nanofibrous scaffolds and then developed towards neurites. As a kind of intermediate filament protein, Nestin, is frequently expressed in nerve cells, which is quite often used in dividing cells during the early stages of development in the radial growth of the axon.^[186, 187] As the same family of intermediate filament protein in the central nerve system, glial fibrillary acidic protein (GFAP) expressed mostly in astrocytes and ependymal cells.^[188] To study the differentiation process of IPS cells on different scaffolds, the GFAP and Nestin were stained and observed after 5 days of culture in the neural differentiation medium (Figure 5b). There were only seeded embryonic bodies on all scaffolds and no obvious neurites and axons could be observed. The relative fluorescence intensity analysis of Nestin in Figure 5c suggests no significant difference between bare PCL and GO-HPGS-coated scaffolds as for the average expression of Nestin. However, when we compared the GFAP expression in Figure 5d, the evolution process towards astrocyte was mainly confined to PCL and PCL-GO. The displayed increased astrocytes could diminish glutamate transporter current and may be detrimental to the development of neurons and axons.^[188] Figure 5e-5h represent the intensity distribution profiles of GFAP and Nestin from the center to the edge of the embryonic body grown on PCL, PCL-HPGS, PCL-GO, and PCL-GO-HPGS, respectively. The embryonic body radius ranges from 40-110 μm . Meanwhile, the fluorescence intensity for the red Nestin at the edge of the colony was more potent than that in the center, which means that the outward cells could absorb more differentiation factors and hormones from the medium. However, the distribution and levels of GFAP signal on PCL-HPGS and PCL-GO-HPGS were quite low, which suggests that the successful coating of HPGS could inhibit the expression of GFAP and then prevent the differentiation potential to astrocyte.

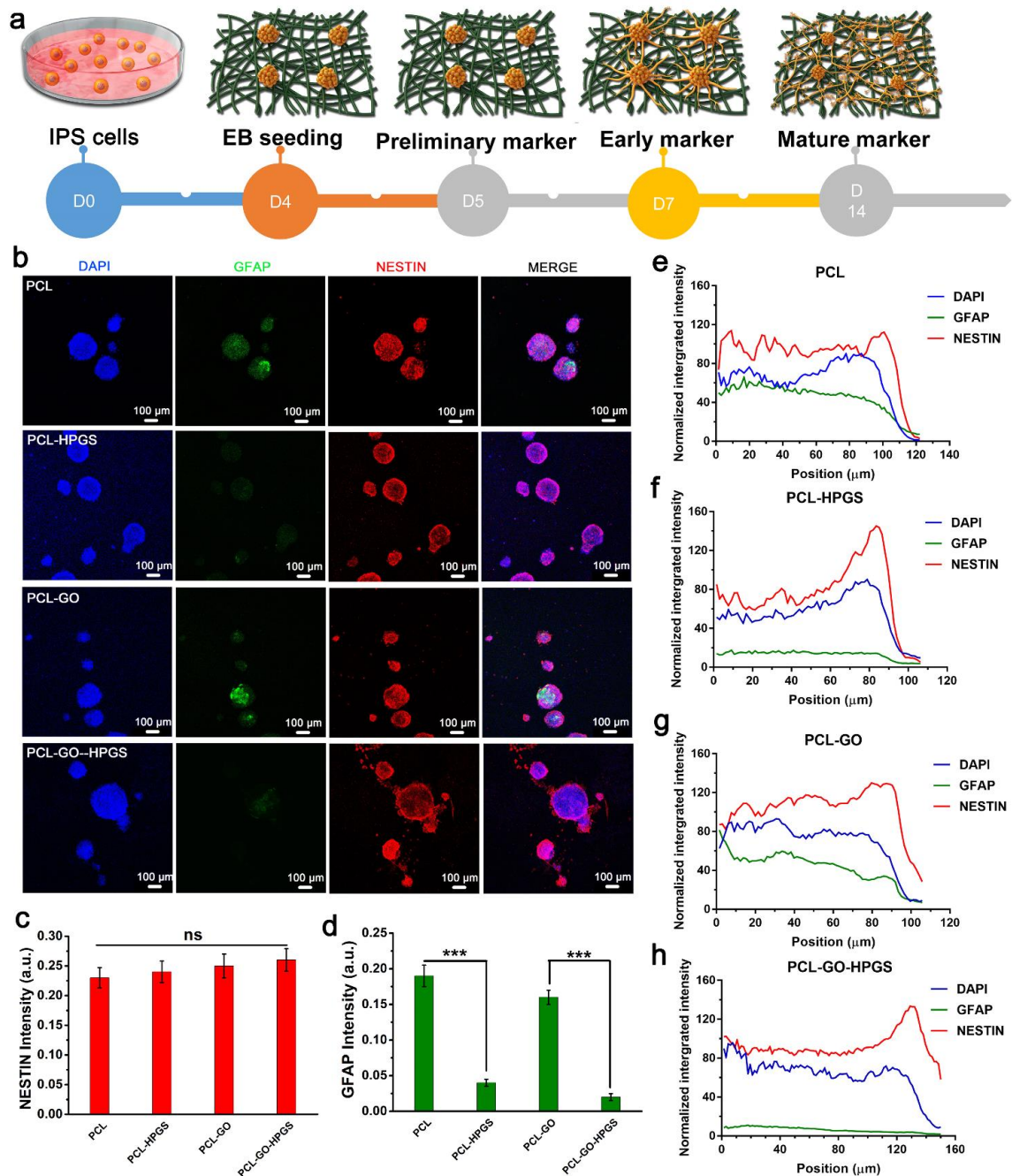


Figure 5. (a) Schematic timeline of the preparation of embryoid bodies (EBs) and the neural differentiation of IPS cells. (b) Immunofluorescence staining of primary neuron marker GFAP and Nestin (blue, DAPI; green GFAP; red Nestin) at 5 days. The average expressions of Nestin (c) and GFAP (d) were quantitatively analyzed from the immunofluorescence-stained images' grey intensity, respectively. Respective intensity distribution profiles of GFAP and Nestin from the center to the edge of the EB grown on PCL (e), PCL-HPGS (f), PCL-GO (g), and PCL-GO-HPGS (h), respectively. (n = 10). *** p < 0.001, ** p < 0.01, and * p < 0.05.

To further evaluate the neural differentiation activities after the embryonic bodies were seeded on GO-HPGS-nanosheet-coated samples. III β -tubulin (Tuj1), as an early neural marker, was investigated. As an exclusively expressed in neurons microtubule component, Tuj1 stands for regenerated axons and neurofilaments.^[189, 190] Figure 6a exhibits immunofluorescence photo of earlier neuron marker protein Tuj1, corresponding 2D fractal dimension (Df), and fluorescence intensity maps after 7 days of culture according to the process in Figure 6a and Figure S6. The immunostaining picture shows higher neurons differentiation rate and more prolonged axon on PCL-GO-HPGS than that on other samples. These neurites, which were spread out very well on PCL, PCL-HPGS, PCL-GO, and PCL-GO-HPGS fibrous structures, were easy to recognize. The statistical analysis of neurites distribution in Figure 6b suggests the PCL-GO-HPGS surface could promote the elongation of neurites. After MATLAB analysis, according to the Tuj1 staining, 2D fractal dimension (Df) and fluorescence intensity map were obtained, which proved that the neurites adhere and elongate quite well on the GO-HPGS nanosheet-coated scaffolds. They also had more dense and longer neurites compared with bare PCL scaffolds. The neurite intersections indicated the apical node and spines of the neurites.

To investigate the number and distribution of spines, the neurite intersections' changes from the EB center to the edge were investigated using image J (Figure 6c). The number of intersections on PCL-GO-HPGS was around 5 times compared with bare PCL. Meanwhile, the intersection number increased from radius 100-400 μm and then decreased to the edge. The number of neurites intersections per area in Figure 6d also suggests that PCL-GO-HPGS had the largest number of apical nodes and spines along with the change from the EB center to the edge. The Df values in Figure 6e suggest the quantification of neurites' spatial arrangement. The neurites on GO-HPGS nanosheet-coated scaffolds have a higher spatial arrangement complexity, for example, branches' types and branches' amounts. As shown in Figure 6f, the relative expression level of Tuj1 on PCL is only half of that on PCL-GO-HPGS. The average neurite number per EB on PCL-GO-HPGS (232 ± 52) was much more massive than that on bare PCL (12 ± 10) (Figure 6g). Besides, the neurite length changed from PCL ($101 \pm 34 \mu\text{m}$) to PCL-GO-HPGS ($345 \pm 109 \mu\text{m}$), which verified that the GO-HPGS nanosheets' coating could significantly improve neurite elongation *in vitro*.

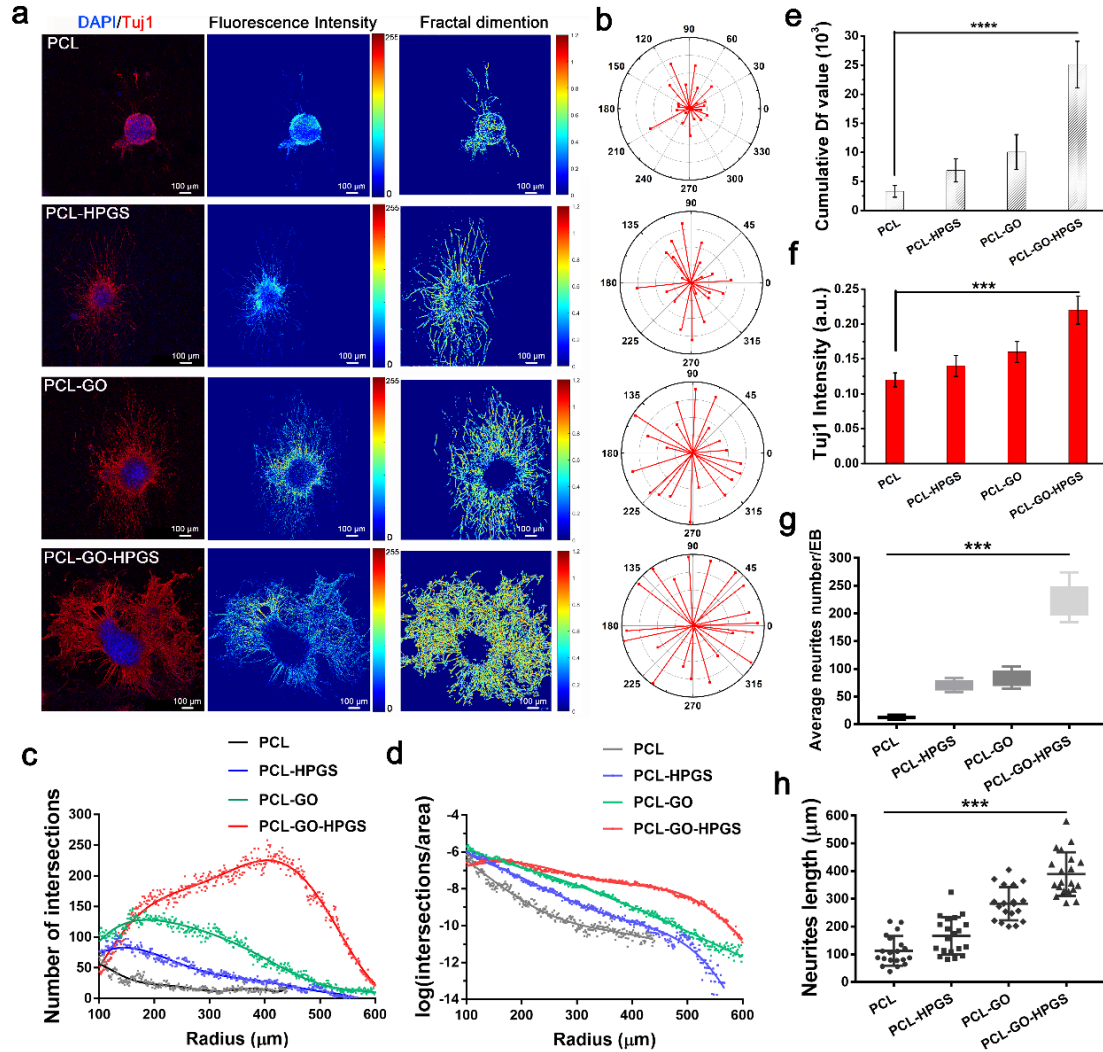


Figure 6. (a) Earlier neuron marker protein Tuj1 (blue, DAPI; red, Tuj1)'s confocal image, 2D fractal dimension (Df) and fluorescence intensity map after 7 days of culture. (b) Top 20 long axons on each sample, the radius and θ ($^\circ$) define the length and the angle of the axons, respectively. (c) The number of neurites' intersections along with the change from the EB center to the edge. Neurite intersections indicated the apical node and spines of the neurites. (d) The number of neurite intersections per area along with the change from the EB center to the edge. (e) The analysis of the quantitative cumulative Df value within a single cell on different samples ($n = 20$). (f) Quantitative analysis, according to the grey intensity, results in the average expression of β III tubulin (Tuj1). (g) The average neurites number per EB on different samples ($n = 20$). (h) The neurite length distribution of different samples ($n = 20$). *** $p < 0.001$, ** $p < 0.01$, and * $p < 0.05$.

As we established a timeline differentiation process for IPS cells from EBs to neural cells, IPS cells were cultured in a suspension of medium to form EBs enriched with neural progenitors. The subsequent adherent culture of EBs on scaffolds resulted in the generation of Tuj1-positive immature neurons at day 5-7, and these cells were

then differentiated into mature neurons with increased positivity for NeuN and microtubule-associated protein 2 (MAP2) after 1 week.^[191] NeuN is a protein mainly expressed in neural nuclei, and MAP2 is a pivotal microtubule protein during the neuritogenesis-microtubule assembly process.^[192] Figure 7a exhibits a few axonal/microtubule sprouting after 14 days of differentiation on bare PCL. However, well-grown neural microtubules and microfilaments could be observed spreading on GO-HPGS nanosheet-coated scaffolds, which suggests that GO-HPGS nanosheets could promote mature neurites' formation. The relative fluorescence intensity in Figure 7c indicates the increased average NeuN and MAP2 expression on PCL-GO-HPGS scaffolds. The fluorescence co-localization analysis in Figure 7b suggests the distribution of MAP2 (red) and NeuN (green) signals in fluorescence microscopy images, which can be used to determine whether two probes co-distributed with one another.^[193] It is evident that the distribution of red signal and green signal on PCL-GO-HPGS was most discrete, which is in line with the Manders' co-localization coefficients (MCC) in Figure 7d and Pearson's correlation coefficient (PCC) in Figure 7e. The smaller the value of the coefficient means the less co-localization is related. Since NeuN protein was mainly expressed in the nuclear, the less co-localization of MAP2 with NeuN on PCL-GO-HPGS suggests more expression of MAP2 in axonal microtubule, which proved more mature neurites on PCL-GO-HPGS than on bare PCL.

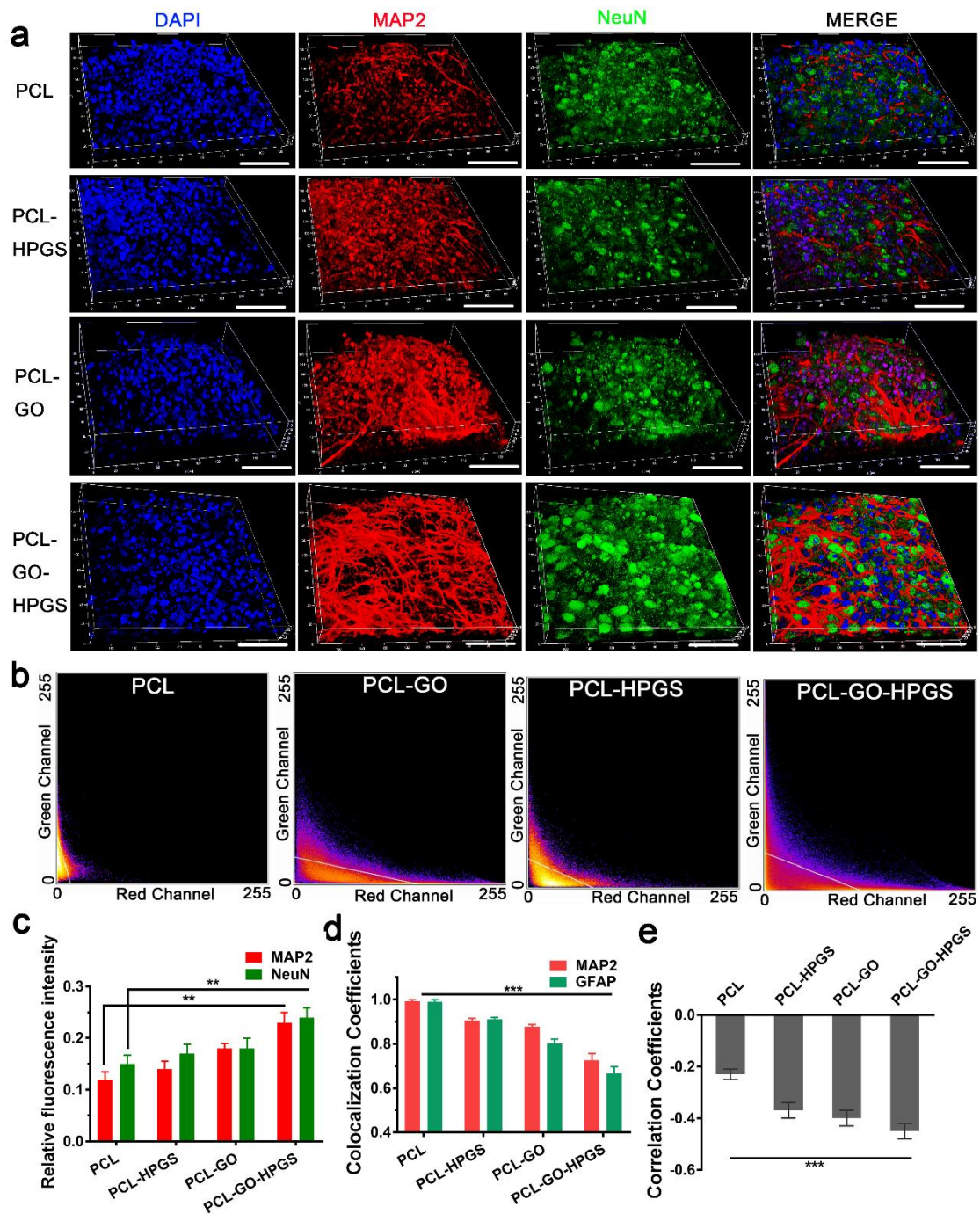


Figure 7. (a) Confocal image of mature neuron marker protein NeuN and MAP2 at day 14 on different samples (blue, DAPI; green, NeuN; red, MAP2). (b) The co-localization map of NeuN and MAP2 protein according to Figure 7a. (c) The quantitative intensity of NeuN and MAP2 according to the immunofluorescence-stained images. (d) MCC of MAP2 and NeuN, MCC is the percentage of co-localized protein in the total amount expressed protein. (e) Pearson's correlation coefficient (PCC) of MAP2 and NeuN protein, the smaller the value, the less co-localization related. *** $p < 0.001$, ** $p < 0.01$, and * $p < 0.05$.

Conclusion

In summary, we have prepared a biocompatible and multivalent polyanion to modify the GO to obtain bioadhesive 2D nanosheets and the 2D nanosheet-coated nanofibrous scaffolds, which exhibited combined physical and chemical cues to promote IPS cells towards neural differentiation. The prepared ECM-mimicking PCL-GO-HPGS scaffolds exhibited high efficiency in promoting the IPS cells' adhesion and proliferation. Meanwhile, the PCL-GO-HPGS scaffolds could keep the seed IPS cells in a good stemness state in the growth medium. Furthermore, we have also validated that the introduced HPGS on the scaffold surface could decrease the differentiation chance towards astrocyte and GO coating could promote the neural differentiation efficiency and maturity. Benefiting from both advantages of HPGS and GO, the scaffolds could promote neural differentiation and decrease the lineage specification towards astrocyte. Overall, this study provides a new way to design multivalent/bioadhesive nanofibrous scaffolds for neural regeneration, which would integrate the chemical and physical cues to facilitate the targeted differentiation of IPS cells. Our design on 2D nanosheet functionalized nanofibrous stem cell-based scaffolds may also provide a new pathway for the fabrication of carbon nanomaterials composites in regenerative therapies as well.

Experimental Section

Materials, preparation, and characterization of methods, stem cell culture and staining experiments, and statistical analysis are all shown in the Supporting Information.

References

- [1] R. G. Canter, J. Penney, L.-H. Tsai, *Nature* **2016**, 539, 187.
- [2] B. De Strooper, E. Karran, *Cell* **2016**, 164, 603.
- [3] L. A. Rocha, D. Silva, S. Barata-Antunes, H. Cavaleiro, E. D. Gomes, N. A. Silva, A. J. Salgado, *Adv. Funct. Mater.* **2020**, 1909083.
- [4] M. J. Landry, K. Gu, S. N. Harris, L. Al-Alwan, L. Gutsin, D. De Biasio, B. Jiang, D. S. Nakamura, T. C. Corkery, T. E. Kennedy, C. J. Barrett, *Macromol. Biosci.* **2019**, 19, 1900036.
- [5] K. J. Brennand, A. Simone, J. Jou, C. Gelboin-Burkhart, N. Tran, S. Sangar, Y. Li, Y. Mu, G. Chen, D. Yu, S. McCarthy, J. Sebat, F. H. Gage, *Nature* **2011**, 473, 221.

- [6] G. Lee, E. P. Papapetrou, H. Kim, S. M. Chambers, M. J. Tomishima, C. A. Fasano, Y. M. Ganat, J. Menon, F. Shimizu, A. Viale, V. Tabar, M. Sadelain, L. Studer, *Nature* **2009**, *461*, 402.
- [7] M. C. N. Marchetto, C. Carromeu, A. Acab, D. Yu, G. W. Yeo, Y. Mu, G. Chen, F. H. Gage, A. R. Muotri, *Cell* **2010**, *143*, 527.
- [8] L. Hou, J. Kim, J. Coller, V. Natsu, N. Huang, *Circulation Research* **2016**, *119*, A357.
- [9] M. L. Lovett, T. J. F. Nieland, Y.-T. L. Dingle, D. L. Kaplan, *Adv. Funct. Mater.* **2020**, *n/a*, 1909146.
- [10] A. Higuchi, Q.-D. Ling, Y. Chang, S.-T. Hsu, A. Umezawa, *Chem. Rev.* **2013**, *113*, 3297.
- [11] A. Higuchi, Q.-D. Ling, Y.-A. Ko, Y. Chang, A. Umezawa, *Chem. Rev.* **2011**, *111*, 3021.
- [12] S. Gao, M. X. Chen, P. Wang, Y. Li, Z. G. Yuan, W. M. Guo, Z. Z. Zhang, X. L. Zhang, X. G. Jing, X. Li, S. Y. Liu, X. Sui, T. F. Xi, Q. Y. Guo, *Acta Biomater.* **2018**, *73*, 127.
- [13] X. Sun, Y. Wang, Z. Y. Guo, B. Xiao, Z. Sun, H. Y. Yin, H. Y. Meng, X. Sui, Q. Zhao, Q. Y. Guo, A. Y. Wang, W. J. Xu, S. Y. Liu, Y. J. Li, S. B. Lu, J. Peng, *Adv. Healthcare. Mater.* **2018**, *7*, 1800276.
- [14] X. Xue, Y. Sun, A. M. Resto-Irizarry, Y. Yuan, K. M. Aw Yong, Y. Zheng, S. Weng, Y. Shao, Y. Chai, L. Studer, J. Fu, *Nat. Mater.* **2018**, *17*, 633.
- [15] J. Zhang, C. Cheng, J. L. Cuellar-Camacho, M. Li, Y. Xia, W. Li, R. Haag, *Adv. Funct. Mater.* **2018**, *28*, 1804773.
- [16] M. J. Landry, F.-G. Rollet, T. E. Kennedy, C. J. Barrett, *Langmuir* **2018**, *34*, 8709.
- [17] H. Chen, J. Sun, Z. Wang, Y. Zhou, Z. Lou, B. Chen, P. Wang, Z. Guo, H. Tang, J. Ma, Y. Xia, N. Gu, F. Zhang, *ACS Appl. Mater. Interfaces* **2018**, *10*, 44279.
- [18] Y. Xia, J. Sun, L. Zhao, F. Zhang, X.-J. Liang, Y. Guo, M. D. Weir, M. A. Reynolds, N. Gu, H. H. K. Xu, *Biomaterials* **2018**, *183*, 151.

- [19] K. Alberti, R. E. Davey, K. Onishi, S. George, K. Salchert, F. P. Seib, M. Bornhäuser, T. Pompe, A. Nagy, C. Werner, P. W. Zandstra, *Nat. Methods* **2008**, *5*, 645.
- [20] M. X. Chen, Z. X. Feng, W. M. Guo, D. J. Yan, S. Gao, Y. Y. Li, S. Shen, Z. G. Yuan, B. Huang, Y. Zhang, M. J. Wang, X. Li, L. B. Hao, J. Peng, S. Y. Liu, Y. X. Zhou, Q. Y. Guo, *ACS Appl. Mater. Interfaces* **2019**, *11*, 41626.
- [21] J. Xue, T. Wu, Y. Dai, Y. Xia, *Chem. Rev.* **2019**, *119*, 5298.
- [22] J. Xue, T. Wu, J. Li, C. Zhu, Y. Xia, *Angew. Chem. Int. Ed.* **2019**, *58*, 3948.
- [23] J. Xue, J. Xie, W. Liu, Y. Xia, *Acc. Chem. Res.* **2017**, *50*, 1976.
- [24] J. Xue, C. Zhu, J. Li, H. Li, Y. Xia, *Adv. Funct. Mater.* **2018**, *28*, 1705563.
- [25] C. Cheng, S. Li, A. Thomas, N. A. Kotov, R. Haag, *Chem. Rev.* **2017**, *117*, 1826.
- [26] Z. Zhang, L. H. Klausen, M. Chen, M. Dong, *Small* **2018**, *14*, 1801983.
- [27] Y. Xia, S. Li, C. Nie, J. Zhang, S. Zhou, H. Yang, M. Li, W. Li, C. Cheng, R. Haag, *Appl. Mater. Today* **2019**, *16*, 518.
- [28] C. X. Nie, L. Ma, S. Li, X. Fan, Y. Yang, C. Cheng, W. F. Zhao, C. S. Zhao, *Nano Today* **2019**, *26*, 57.
- [29] L. Ma, M. Zhou, C. He, S. Li, X. Fan, C. Nie, H. Luo, L. Qiu, C. Cheng, *Green Chem.* **2019**, *21*, 4887.
- [30] C. J. Wan, L. Q. Zhu, Y. H. Liu, P. Feng, Z. P. Liu, H. L. Cao, P. Xiao, Y. Shi, Q. Wan, *Adv. Mater.* **2016**, *28*, 3557.
- [31] C. Cheng, J. Zhang, S. Li, Y. Xia, C. Nie, Z. Shi, J. L. Cuellar-Camacho, N. Ma, R. Haag, *Adv. Mater.* **2018**, *30*, 1705452.
- [32] C. Cheng, S. Li, Y. Xia, L. Ma, C. Nie, C. Roth, A. Thomas, R. Haag, *Adv. Mater.* **2018**, *30*, 1802669.
- [33] F. Paulus, D. Steinhilber, P. Welker, D. Mangoldt, K. Licha, H. Depner, S. Sigrist, R. Haag, *Polym. Chem.* **2014**, *5*, 5020.
- [34] Q. Ran, X. Xu, P. Dey, S. Yu, Y. Lu, J. Dzubiella, R. Haag, M. Ballauff, *J. Chem. Phys.* **2018**, *149*, 163324.
- [35] J. Zhao, M. Tang, J. Cao, D. Ye, X. Guo, J. Xi, Y. Zhou, Y. Xia, J. Qiao, R. Chai, X. Yang, J. Kang, *Adv. Sci.* **2019**, *6*, 1802136.

- [36] C. Fasting, C. A. Schalley, M. Weber, O. Seitz, S. Hecht, B. Kokschi, J. Dervede, C. Graf, E.-W. Knapp, R. Haag, *Angew. Chem. Int. Ed.* **2012**, *51*, 10472.
- [37] Y. Xia, C. Cheng, R. Wang, H. Qin, Y. Zhang, L. Ma, H. Tan, Z. Gu, C. Zhao, *Polym. Chem.* **2014**, *5*, 5906.
- [38] J. Vonnemann, S. Liese, C. Kuehne, K. Ludwig, J. Dervede, C. Böttcher, R. R. Netz, R. Haag, *J. Am. Chem. Soc.* **2015**, *137*, 2572.
- [39] M. F. Gholami, D. Lauster, K. Ludwig, J. Storm, B. Ziem, N. Severin, C. Böttcher, J. P. Rabe, A. Herrmann, M. Adeli, R. Haag, *Adv. Funct. Mater.* **2017**, *27*, 1606477.
- [40] S. Dupont, L. Morsut, M. Aragona, E. Enzo, S. Giulitti, M. Cordenonsi, F. Zanconato, J. Le Digabel, M. Forcato, S. Bicciato, N. Elvassore, S. Piccolo, *Nature* **2011**, *474*, 179.
- [41] W. Deng, F. Shao, Q. He, Q. Wang, W. Shi, Q. Yu, X. Cao, C. Feng, S. Bi, J. Chen, P. Ma, Y. Li, A. Gong, S. Tong, J. Yu, M. Spector, X. Xu, Z. Zhang, *Adv. Mater.* **2019**, *31*, 1806861.
- [42] B. Zhao, X. Wei, W. Li, R. S. Udan, Q. Yang, J. Kim, J. Xie, T. Ikenoue, J. Yu, L. Li, P. Zheng, K. Ye, A. Chinnaiyan, G. Halder, Z.-C. Lai, K.-L. Guan, *Genes & Development* **2007**, *21*, 2747.
- [43] C. M. Madl, B. L. LeSavage, R. E. Dewi, K. J. Lampe, S. C. Heilshorn, *Adv. Sci.* **2019**, *6*, 1801716.
- [44] I. Lian, J. Kim, H. Okazawa, J. Zhao, B. Zhao, J. Yu, A. Chinnaiyan, M. A. Israel, L. S. B. Goldstein, R. Abujarour, S. Ding, K.-L. Guan, *Genes & Development* **2010**, *24*, 1106.
- [45] Y. Li, H. Feng, H. Gu, D. W. Lewis, Y. Yuan, L. Zhang, H. Yu, P. Zhang, H. Cheng, W. Miao, W. Yuan, S.-Y. Cheng, S. M. Gollin, T. Cheng, *Nat. Commun.* **2013**, *4*, 2174.
- [46] H. Zheng, W.-M. Yu, J. Shen, S. Kang, D. Hambardzumyan, J. Y. Li, Y. Shen, A. M. Kenney, J. Chen, C.-K. Qu, *Sci. Adv.* **2018**, *4*, eaat2681.
- [47] J. Chen, S. Boyle, M. Zhao, W. Su, K. Takahashi, L. Davis, M. DeCaestecker,

- T. Takahashi, M. D. Breyer, C.-M. Hao, *Journal of the American Society of Nephrology* **2006**, *17*, 1283.
- [48] A. A. Sosunov, E. Guilfoyle, X. Wu, G. M. McKhann, J. E. Goldman, *J. Neurosci.* **2013**, *33*, 7439.
- [49] J. Lu, X. Zhong, H. Liu, L. Hao, C. T.-L. Huang, M. A. Sherafat, J. Jones, M. Ayala, L. Li, S.-C. Zhang, *Nat. Biotechnol.* **2016**, *34*, 89.
- [50] P. A. Nistor, P. W. May, F. Tamagnini, A. D. Randall, M. A. Caldwell, *Biomaterials* **2015**, *61*, 139.
- [51] G. Kouroupi, E. Taoufik, I. S. Vlachos, K. Tsioras, N. Antoniou, F. Papastefanaki, D. Chroni-Tzartou, W. Wrasidlo, D. Bohl, D. Stellas, P. K. Politis, K. Vekrellis, D. Papadimitriou, L. Stefanis, P. Bregestovski, A. G. Hatzigeorgiou, E. Masliah, R. Matsas, *PNAS* **2017**, 201617259.
- [52] B. Ji, H. Kaneko, T. Minamimoto, H. Inoue, H. Takeuchi, K. Kumata, M.-R. Zhang, I. Aoki, C. Seki, M. Ono, M. Tokunaga, S. Tsukamoto, K. Tanabe, R.-M. Shin, T. Minamihisamatsu, S. Kito, B. J. Richmond, T. Suhara, M. Higuchi, *J. Neurosci.* **2016**, *36*, 11544.
- [53] K. W. Dunn, M. M. Kamocka, J. H. McDonald, *Am. J. Physiology-Cell Physiology* **2011**, *300*, C723.

Supporting Information

Multivalent Polyanionic 2D Nanosheets Functionalized Nanofibrous Stem Cell-based Neural Scaffolds

Yi Xia, Hua Yang, Shuang Li, Suqiong Zhou, Liyun Wang, Chong Cheng, and Rainer Haag**

1.1 Materials

All chemicals were purchased from Sigma (Steinheim, Germany) unless stated, including dimethylformamide (DMF, CAS: 68-12-2), pyridine (CAS: 110-86-1), trimethylamine (Et₃N, CAS: 121-44-8), methanesulfonyl chloride (MsCl, CAS: 124-63-0), NaN₃ (CAS: 26628-22-8), SO₃ pyridine complex (CAS: 26412-87-3), NaNO₃ (CAS: 7631-99-4), KMnO₄ (CAS: 7722-64-7), ascorbic acid (CAS: 50-81-7), and graphite flakes (CAS: 7782-42-5). The mica wafers are commercially available. Dialysis was performed in benzoylated cellulose tubes from Sigma-Aldrich (D7884, width: 32 mm, molecular weight cut-off (MWCO) 2000 g·mol⁻¹). The deionized water used was purified using a Millipore water purification system with a minimum resistivity of 18.0 MΩ·cm. Dialysis was performed in benzoylated cellulose tubes from Sigma-Aldrich (category number: D7884, width: 32 mm, molecular weight cut-off (MWCO) 2000 g·mol⁻¹).

1.2 Characterization Methods

Fourier-transform infrared spectroscopy (FTIR): FTIR spectra were recorded using a JASCO spectrometer. Ultrasonic bath (Model: SONOREX, RK255 HZ, made in Germany) was used to disperse materials in solvents.

Water contact angle (WCA): Static contact angle measurements were performed by using a contact angle goniometer (Data Physics Instruments, Germany) with the sessile drop method. A liquid drop of 2 μL Milli-Q water was placed on the substrate

and allowed to equilibrate for 15 s at room temperature. At least eight measurements were averaged on every five parallel samples to get a reliable value.

Atomic force microscopy (AFM): The AFM results were recorded by a Multimode Nanoscope V scanning probe microscopy (SPM) system (Bruker, USA) in the air under ambient conditions. The commercially available AFM cantilever tips with a force constant of ~ 48 N/m and resonance vibration frequency of ~ 330 kHz were used, and the scanning rate was set at 0.8 Hz. The AFM samples for nano-dispersion were prepared by dropping aqueous dispersion (~ 0.01 mg/mL, sonicated for 5 minutes with an ultrasonic bath cleaner) on a freshly cleaved mica surface and dried under vacuum at 60 °C. The AFM mode and Peak Force QNM was used in order to control better the force with which the tip interacted with the surface. PPP-NCLR-20 probes with force constant 21-98 N/m (silicon, resistivity: 0.01-0.02 $\Omega\cdot\text{cm}$ Bruker) were used for the ambient measurement.

Scanning electron microscope (SEM): The morphology of the nano-dispersion coated substrates was observed by ultrahigh-resolution FE-SEM (Hitachi SU8200). The samples were dried in an oven and then attached to the sample supports using carbon tape. All the samples were coated with gold with about 1 nm.

Transmission electron microscopy (TEM): Droplets (~ 5 μL , ~ 0.02 mg/mL) of the sample solution were placed on ultrathin carbon film on copper grids (Ted Pella, Inc. USA), and the supernatant liquid was removed by blotting with a piece of filter paper. The grids were allowed to air dry at least 40 min and were subsequently transferred into a TEM machine, Tecnai G2 F20 S-TWIN transmission electron microscope (FEI Ltd., USA), and operated at 200 kV. The high-angle annular dark-field scanning transmission electron microscopy (HAADF-STEM) has been performed by the same machine.

X-ray photoelectron spectroscopy (XPS): XPS was measured on K-AlphaTM + X-ray Photoelectron Spectrometer System (Thermo Scientific) with Hemispheric 180 ° dual-focus analyzer with 128-channel detector. X-ray monochromator is micro-focused for Al-K α radiation. For the measurement, the powder samples were pressed and loaded

on carbon taps, then pasted onto the sample holder for measurement. The data was collected with an X-ray spot size of 400 μm , 20 scans for the survey, and 50 scans for the regions. Survey spectra were run in the binding energy range of 0-1000 eV, and high-resolution spectra of C1s, N1s, O1s, and S2p were collected. The XPS spectra of nano-compounds and scaffolds were conducted by a similar method.

1.3 Preparation and Characterization of GO-HPGS Nanosheets

Synthesis of graphene oxide (GO)

GO was prepared from natural graphite flakes by a modified Hummers' method.^[139] 2.5 g graphite and 1.875 g NaNO_3 were placed in a flask. Then, 75 mL H_2SO_4 was added with stirring in an ice-water bath, and 10 g KMnO_4 were slowly added over about 1 h. The mixture was stirred in the ice water bath for 2 h, which was followed by a vigorously stirring for 12 h at 60 °C. Then, the mixture was slowly diluted with DI water (700 mL), and the excess KMnO_4 was decomposed by H_2O_2 (30 wt.%, 15 mL). The insoluble precipitations were removed by centrifugation. The resultant GO solution was filtered and washed with HCl (10 wt.%, 1 L) and DI water for several times to remove the metal ions. The pristine brown GO solution was dialyzed with deionized water for 1 week before removing any residual salts and acids.

Synthesis of HPG covalently functionalized graphene oxide (GO-HPG)

First, the hyperbranched polyglycerol (HPG) (molecular weight of $M_n = 7200$ $\text{g}\cdot\text{mol}^{-1}$, PDI < 1.2, and a degree of branching of $\sim 50\%$) was polymerized by a one-step ring-opening anionic polymerization (ROAP), as mentioned in our earlier reports.^[143, 144] The synthesized HPG was dissolved in dry DMF (50 mL) and 10 mL pyridine. Then Et_3N (0.7 mL, 4.965 mmol, 1.5 eq.) was added and cooled to 0 °C. And then, the MsCl (0.659 mL, 8.512 mmol, 1.5 eq.) in dry pyridine (20 mL) was added dropwise through a syringe at 0 °C. After stirring the solution for 1 h at 0 °C, it was allowed to reach room temperature (r.t.) and was stirred for 16 h to obtain HPG-Ms. The obtained HPG-Ms was dissolved in 80 mL dry DMF upon ultrasonication in a one-necked flask with a

reflux condenser and magnetic stirrer. After the addition of NaN₃ (sodium azide, 5 eq.), the resulting suspension was heated at 70 °C for 3 days to get azide-functionalized hyperbranched polyglycerol (HPG-N₃) as reported in our earlier paper.^[108]

To avoid the strong electrostatic repulsion between highly negatively charged HPGS and graphene oxide (GO), we used the electrically neutral HPG-N₃ to functionalize GO. The HPG-N₃, ~11% azide-grafting ratio, was first anchored onto the GO surface via covalent conjugation and multi-noncovalent interactions. The covalent conjugation was generated between the azide group on HPG and residual sp² bonds on GO through [2+1] nitrene cycloaddition reaction at 120 °C.

Synthesis of the sulfated GO-HPG (GO-HPGS)

To achieve the extracellular-matrix/heparin mimetic structures, the GO-HPG was consecutively post-sulfated to convert bioinert HPG into cell adhesive-sulfated HPGS, namely, GO-HPGS. The above-yielded GO-HPG (600 mg) was re-dispersed in dry DMF at a concentration of 1 mg/mL. Then this solution was heated to 60 °C with vigorous stirring. Then 6.45 g SO₃·pyridine complex in 200 mL DMF was added into GO-HPG slowly for 2 h. The reaction was maintained in 60 °C for 48 h. After the reaction, the extra amount of SO₃·pyridine complex was removed by centrifugation 5 times, and the product was alternatively washed by acid and basic solution for 2 cycles.^[108]

Synthesis of the hyperbranched polyglycerol sulfates (HPGS)

The above-obtained HPG was dissolved in anhydrous DMF (50.0 mL) and heated to 60 °C. A freshly prepared solution of SO₃ pyridine complex (9.88 g) in anhydrous DMF (65.0 mL) was added over a period of 2 h. The mixture was stirred for 2 h at 60 °C, then for 2 d at room temperature, and was subsequently quenched with water (50 mL). The pH was immediately adjusted to 8 by the addition of 1(N) NaOH. The solvents were evaporated, and the residue was alternatively subjected to dialysis in water for 1 week. Evaporation of the solvent gave the title compound in 88% yield.

Degree of sulfation \approx 80% from CHNS analysis. The obtained HPGS were characterized by NMR and FTIR.^[108]

1.4 Fabrication of GO-HPGS nanosheet-coated polycaprolactone (PCL) fibers

Fabrication of electrospun PCL fibers

PCL (80 kDa, Sigma) was dissolved in 1,1,1,3,3,3-hexafluoro-2-propanol (HFIP) to prepare a 10% (1 g in 10 mL, w/v) polymer solution. The polymer solution was placed into a syringe with a metal needle and then electrospun onto an aluminum foil-wrapped drum collector, which was positioned horizontally, at a flow rate of 2 mL/h. 18 kV voltage was applied with a high voltage power supply, and a 12 cm working distance was utilized. The PCL fibers were dried under vacuum overnight and then peeled off from the aluminum foil for further usage.

Generating GO-HPGS nanosheets coated with PCL fibers (PCL-GO-HPGS)

PCL fibers were treated with O₂ plasma for 1 min to transfer the hydrophobic polymer surface to hydrophilic and generate free radicals for covalent bonding with GO-HPGS nanosheets. The O₂ plasma-treated PCL fibers were dipped into GO-HPGS nanosheets at a concentration of 1 mg/mL. The coated substrates were then vacuumed dried overnight. The HPGS- and GO-coated membranes were fabricated by the same method. The obtained fibers were then characterized by SEM, EDS Mapping, XPS, and WCA.

1.5 Stem cell culture and bioactivity characterizations

Cell culture

Mouse-induced pluripotent stem cells (IPS) were purchased from Lonza, USA. The necessary approval before carrying out IPS-related experiments was obtained from the Department of Biology, Chemistry, and Pharmacy, Freie Universität Berlin. The culture plates were coated with laminin (R&D Systems, USA) solution at the concentration of 5 $\mu\text{g}/\text{cm}^2$ in PBS. The cells were cultured in IPS Feeder-free Culture Medium-ESGRO Complete PLUS Clonal Grade Medium (MERCK), containing selective GSK3 β

inhibitor supplement (MERCK). The cells were maintained at 37 °C in a saturated humidity atmosphere containing 95% air and 5% CO₂. The cells were passaged and collected with Accutase (Thermo Fisher) after reaching 70-80% confluency.

Cytocompatibility

The harvested cells were seeded on PCL, PCL-HPGS, PCL-GO, and PCL-GO-HPGS samples at the density of 1×10^4 cells/cm². The viability of cells was assessed after 3 days of culture using a Calcein AM/Ethidium homodimer-1 dye (LIVE/DEAD Cell Viability Assay, Life Technologies) under the protocol instruction from the manufacturer. After 30 minutes of sample incubation with the reagents at 37 °C, they were washed with DPBS. The fluorescence microscope (Zeiss Z1 Microscope) was used to obtain the images. Live and dead cells appeared as green and red, respectively.

The proliferation of IPS was evaluated by the cell counting kit-8 (CCK-8, Thermo Fisher) on day 1, day 3, and day 5, respectively. 10 µL of the CCK-8 solution was added to each well of 96-well plates, and cells were incubated at 37 °C for 4 h. The absorbance intensity of each sample was determined at a wavelength of 450 nm using a microplate reader (infinite M200PRO, TECAN, Switzerland). All experiments were repeated three times, and six parallel replicates were read for each sample.

Cell morphology

The cellular spreading morphology and skeleton were stained with phalloidin-647/DAPI; the cells were washed with DPBS before fixing the sample with 4% paraformaldehyde for 20 min. 0.1% Triton X-100 in DPBS was used for 30 min to permeabilize the cell membrane. The samples were then incubated with Alexa Fluor 647 phalloidin at 1:400 and DAPI at 1:200 dilutions in DPBS each for 45 min sequentially. Following three additional washings with PBS, the samples were observed under an inverted confocal microscope (Leica SP8, Germany).

1.6 Stem cell differentiation and characterizations

IPS cells' neural differentiation

The collected IPS cells were cultured on non-treated cell culture dishes in neuron

differentiation medium (Thermo Fisher) at 2×10^5 cells/mL. We incubated the cells in a 37 °C, 5% CO₂ incubator to allow them to form embryoid bodies (EBs). On the next day, we fed EBs with fresh differentiation medium by transferring EBs into a 15-ml conical tube and spinning the tube at 200 x g for 1 minute. We re-suspended the EBs in a fresh IPS cells' differentiation medium and re-plated them in a new non-treated cell culture dish. The next day, we divided the EBs into 4 new dishes with fresh differentiation medium supplemented with 0.5 μM retinoic acid (Sigma-Aldrich) and 200 ng/mL Sonic Hedgehog C25II Recombinant Mouse Protein (Thermo Fisher). After 7 days, we stained the cells with previous neuron marker β III tubulin (TUJ1). After 12 days of differentiation, cells expressed mature neuron marker microtubule-associated protein 2 (MAP2) and NeuN.

Immunofluorescence staining

The samples were then fixed in 4% paraformaldehyde and permeabilized with 0.1% Triton X-100 in PBS. The non-specific binding epitopes were blocked with 5% (w/v) BSA (bovine serum albumin). The primary antibodies Anti-YAP (1:400, mouse; Thermo Fisher), Anti-Nanog (1:200, rabbit; Abcam), Anti-Oct4 (1:200, rabbit; Abcam), Anti-Sox2 (1:400, mouse; Thermo Fisher), Anti-SSEA1 (1:400, mouse; Thermo Fisher), Anti-GFAP (1:400, rabbit; Cell Signalling), Anti-Nestin (1:400, mouse; Novus), Anti-β III tubulin (TUJ1) (1:400, mouse; Thermo Fisher), Anti-microtubule-associated protein 2 (MAP2) (1:400, mouse; Thermo Fisher) and Anti-NeuN (1:400, rabbit; Thermo Fisher) were dissolved in 5% (w/v) BSA. The samples were incubated with the primary antibodies at 4 °C overnight. Following 3 to 4 times intensive washing (0.5 wt% Tween-20 in PBS), the secondary antibody labeling was performed with goat anti-mouse IgG conjugated to Alexa Fluor Plus 647 (Thermo Fisher) and goat anti-rabbit IgG conjugated to Alexa Fluor Plus 488 (Abcam). After repeated washing in PBS and nuclear counterstaining with DAPI, the neural markers were then visualized under a confocal microscope (Leica SP8, Germany). All images were taken under the same exposure conditions for analyzing the relative fluorescence intensity.

Image analysis

Cell spreading area, the shape factor, and volume were quantified based on F-actin staining and nucleus form z-direction confocal imaging. The focal adhesion analysis was performed based on vinculin staining. The fluorescent intensity and contrast were drawn along the representation morphology of each cell under the 8-bit greyscale images. The area and integrated densities were measured by the calibrate function. At least 200 cells were evaluated for each independent sample. For measurements of YAP nucleus localization in scaffolds, the images were thresholded on each color channel to determine the nucleus and cytoskeleton area outside of the nucleus. The YAP nucleus localization ratio was calculated according to Equation 1.

$$\text{Nuclear YAP (nuclear/cytoplasmic)} = \frac{\frac{\text{Nuclear YAP intensity}}{\text{Area of nucleus}}}{\frac{\text{Cell YAP intensity} - \text{Nuclear YAP intensity}}{\text{Area of cell} - \text{Area of nucleus}}} \quad (1)$$

All the above-mentioned images were presented as maximum intensity and analyzed by Fiji software (based on ImageJ), and we determined the 2D fractal dimension organization with a custom-developed MATLAB program (MATLAB, Natick, MA) divided images into a series of regions of 100 pixels² spaced at 20 pixels, individually averaged to filter out noise throughout the cell study.

Corresponding 2D fractal dimensions (Df)

Df was analyzed by MATLAB of the F-actin staining images. Interrogation windows are used to digitally subdivide cytoskeletal images. To characterize the cytoskeleton spatial arrangement and density, box-counting was utilized to infer a fractal dimension (Df). Df is a dimensionless value to quantify the complex arrangement of the cell cytoskeleton. Automated partitioning and analysis of whole-cell images using MATLAB for subcellular quantification of the cytoskeleton structure process are as follows: custom algorithm automatically partitions cytoskeletal images into the relevant biological regions, from which a mask is generated and data extracted can be specific to these regions. (a) Initially, images of the cytoskeleton were imported

for processing, which included a series of segmentation procedures to outline the shape of the cell. (b) Each cytoskeleton image was then scanned using non-overlapping interrogation windows, within each, fractal analysis is performed through a box-counting method, quantifying the actin arrangement as defined by an edge detection filter. The regional mask was then used to differentiate perinuclear, cytosolic, and peripheral actin quantity and actin arrangement information from the raw cytoskeleton image and a resultant 2D array of fractal dimension values, respectively. (c) A user-defined set distance is then used to redefine these boundaries, and pixels between the new and original boundaries form the masks required. This is repeated for each paired cytoskeleton image for the entire live imaging dataset. MATLAB commands used for the entire process are noted under the title of each step, and custom codes are further denoted with a “.m.”

Statistical Analysis

All data were expressed as the means \pm standard deviations (s.d) with independent experiments. The statistical analysis was performed using one-way analysis of variance (ANOVA) with the Tukey honestly significant difference *post hoc* test using origin 9.0 software. The data was indicated with (*) for $p < 0.05$, (**) for $p < 0.01$, and (***) for $p < 0.001$.

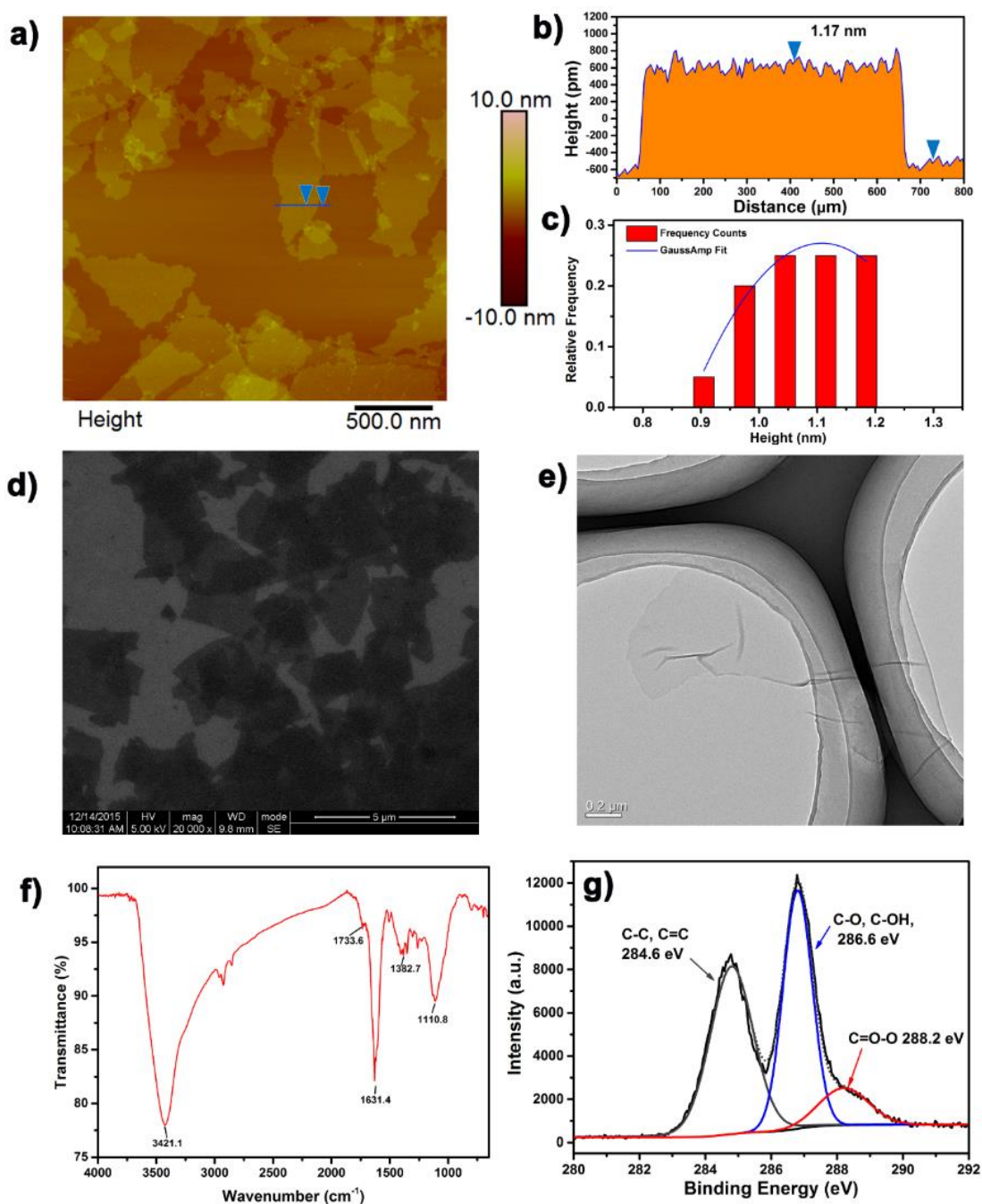


Figure S1. (a) AFM images for pristine GO on freshly cleaved mica. (b) The average height difference between the two arrows was about 1.17 nm. (c) The calculated thickness distribution of GO from 25 nanosheets. Each thickness ranged from 0.9 nm to 1.2 nm, which indicated all of the obtained GO nanosheets were purely single-layer products. (d) An SEM image of the fabricated GO on a Si/SiO₂ wafer (the black spots depict GO). (e) TEM image of GO nanosheets with highly flexible structures. (f) The

FTIR spectrum of GO powder, $\nu_{\max}/\text{cm}^{-1}$: 3421.1 (-OH), 1733.6 (-COOH), 1631.4, 1382.7, 1110.8 (C-O). (g) The high-resolution C1s spectrum of GO powder. Binding energies at 284.6, 286.6, and 288.2 eV were assigned to the carbon skeleton (C-C/C=C), hydroxyl group (C-OH), and epoxide group (-C-O-C-), and carboxyl group (-O-C=O), respectively.

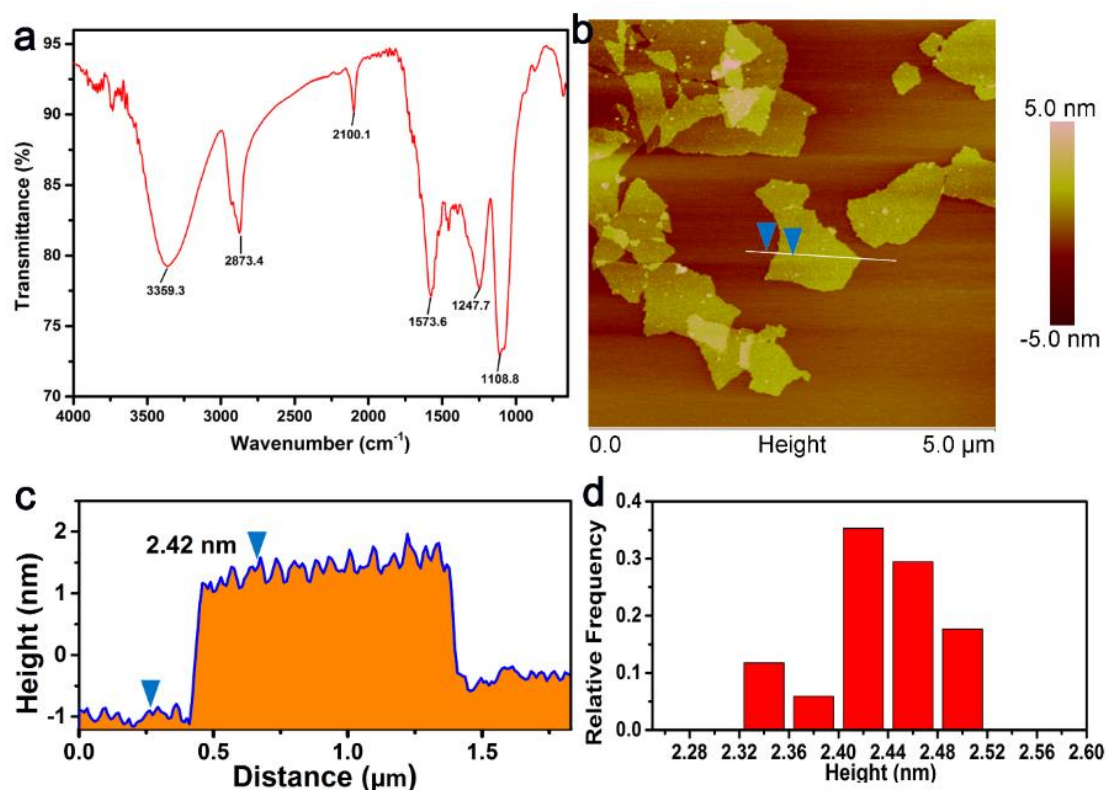


Figure S2. (a) The FTIR spectrum of GO-HPG powder, $\nu_{\max}/\text{cm}^{-1}$: 3359.3 (-OH), 2873.4 (-CH-, -CH₂-), 2100.1 (-N₃), 1573.6, 1247.7, 1108.8 (C-O). (b) AFM image for pristine GO-HPG on freshly cleaved mica. (c) The average height difference between the two arrows was about 2.42 nm. (d) The calculated thickness distribution of GO-HPG-N₃ from 25 nanosheets. All the thicknesses ranged from 2.32 nm to 2.52 nm, which indicated all of the obtained GO-HPG nanosheets were purely single-layer products, i.e., a monolayer coating of HPG on GO nanosheets.

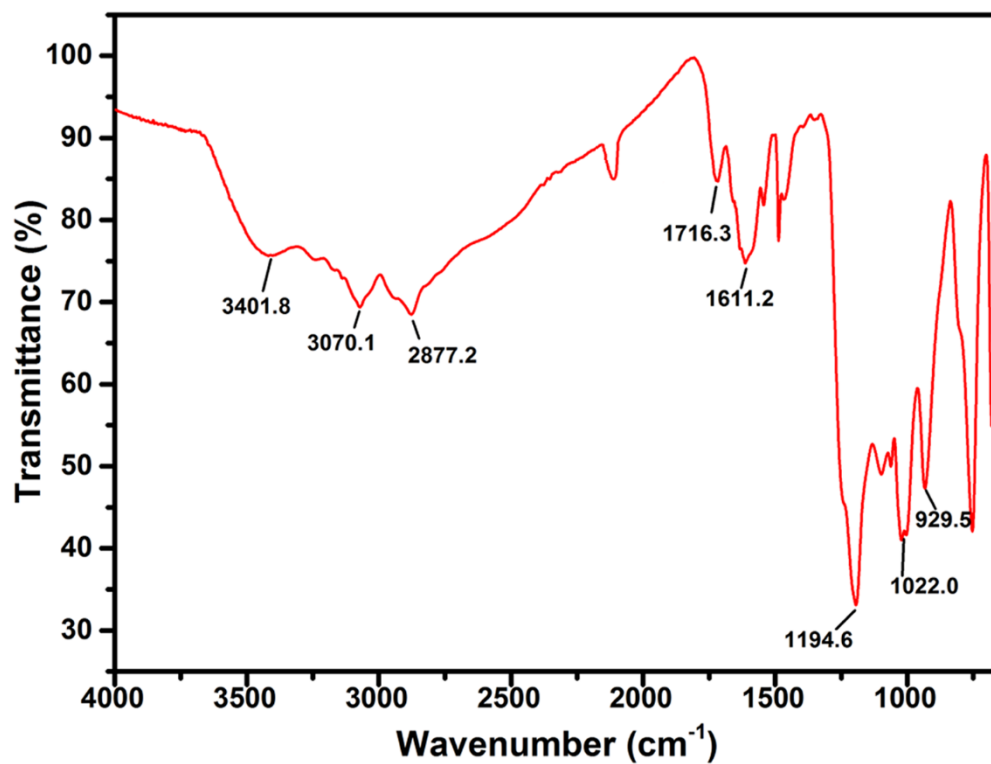


Figure S3. (a) The FTIR spectrum of GO-HPGS powder, $\nu_{\max}/\text{cm}^{-1}$: 3401.8 (-OH), 3070.1, 2877.2 (-CH-, -CH₂-), 2106.1 (-N₃), 1716.3, 1611.2, 1194.6 (C-O), 1022.0, 929.5 (-SO₃⁻).

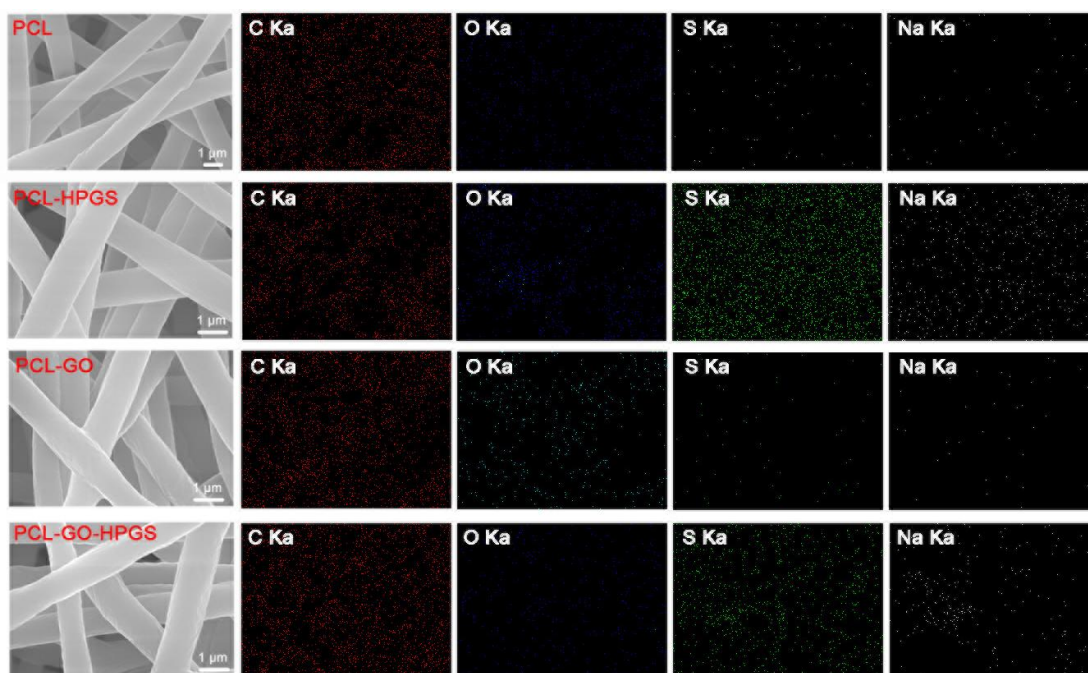


Figure S4. The SEM and element mapping of C, O, S, Na on the surface of PCL, PCL-HPGS, PCL-GO, and PCL-GO-HPGS.

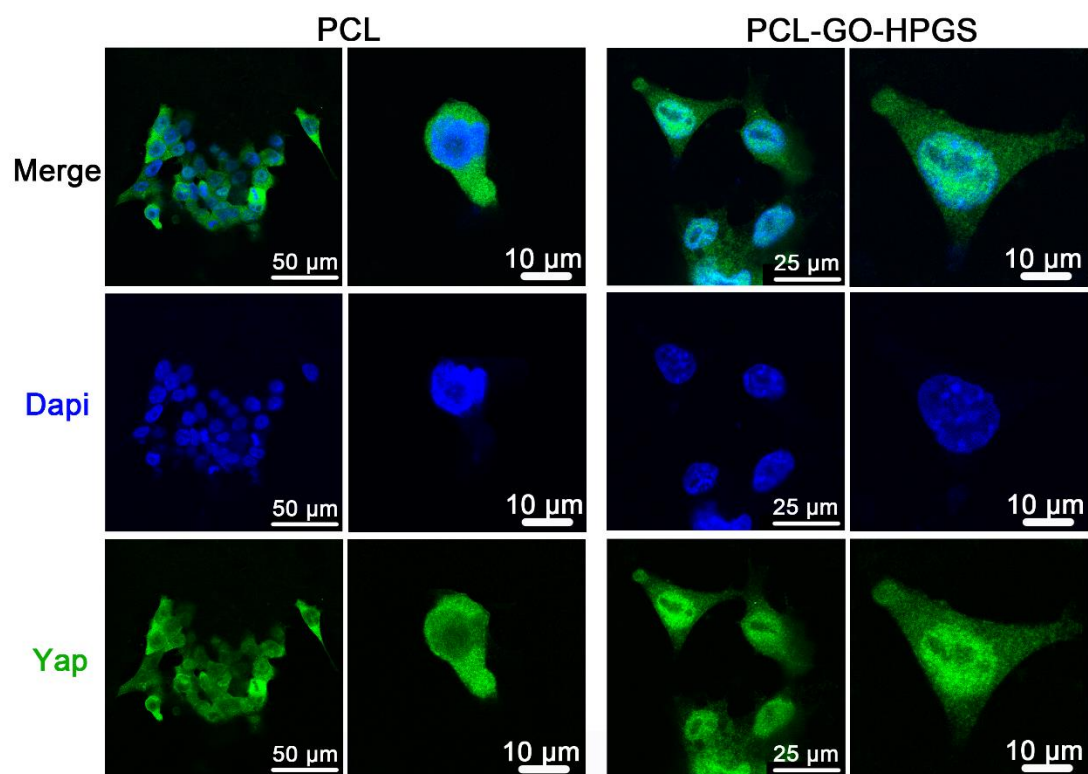


Figure S5. Immunofluorescence staining of the YAP signal in IPS cells after 7 days of culture (DAPI, blue; YAP, green) on PCL and PCL-GO-HPGS membrane.

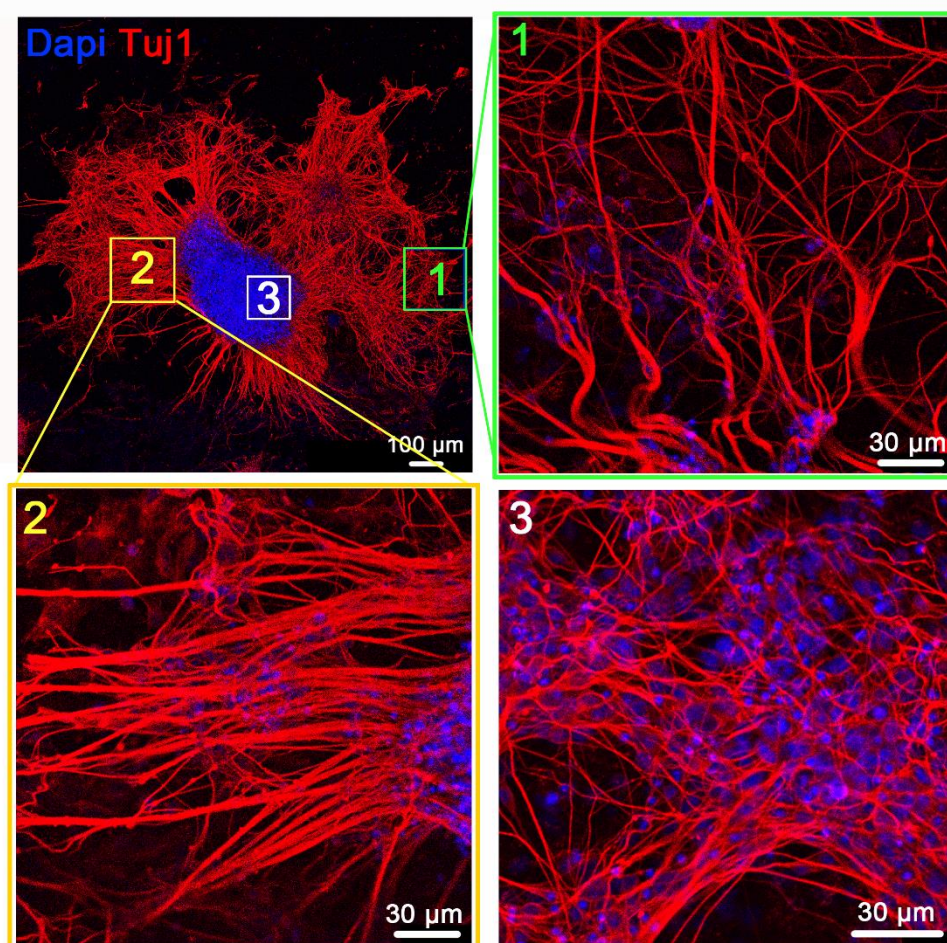
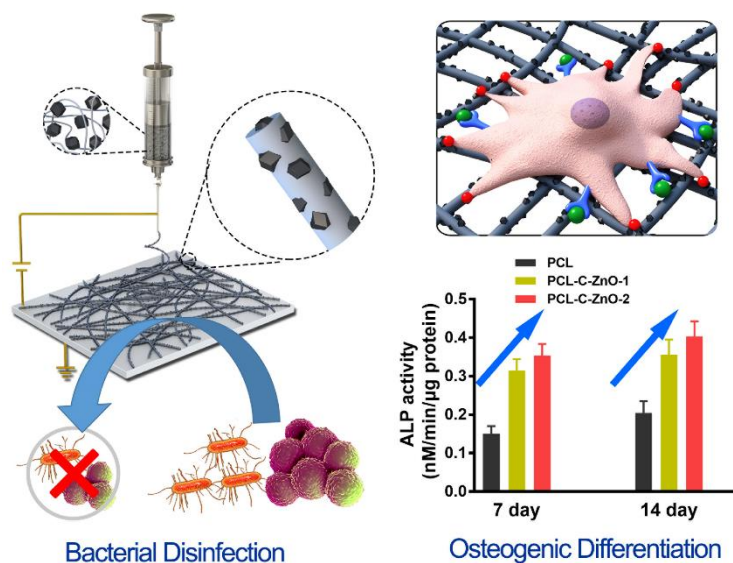


Figure S6. Immunofluorescence of earlier neuron marker protein Tuj1 (blue is DAPI, red is earlier neuron marker Tuj1) after 7 days of differentiation on PCL-GO-HPGS membrane. (1), (2), and (3) are the amplified neurites' images.

References

- [1] C. Cheng, S. Li, S. Nie, W. Zhao, H. Yang, S. Sun, C. Zhao, *Biomacromolecules* **2012**, 13, 4236.
- [2] a) Q. Wei, T. Becherer, P.-L. M. Noeske, I. Grunwald, R. Haag, *Advanced Materials* **2014**, 26, 2688; b) Q. Wei, K. Achazi, H. Liebe, A. Schulz, P.-L. M. Noeske, I. Grunwald, R. Haag, *Angewandte Chemie International Edition* **2014**, 53, 11650.
- [3] C. Cheng, J. Zhang, S. Li, Y. Xia, C. Nie, Z. Shi, J. L. Cuellar-Camacho, N. Ma, R. Haag, *Advanced Materials* **2018**, 30, 1705452.

3.3. ZnO/Nanocarbons-Modified Fibrous Scaffolds for Stem Cell-based Osteogenic Differentiation



Yi Xia, Xin Fan, Hua Yang, Ling Li, Chao He, Chong Cheng,* and Rainer Haag*

Small 2020, 16, 2003010

DOI: <https://doi.org/10.1002/sml.202003010>

<https://onlinelibrary.wiley.com/doi/full/10.1002/sml.202003010>

Author contributions:

Yi Xia performed the main experiments, and wrote the manuscript.

Xin Fan conducted the antibacterial experiments and analyzed the release of Zn ions data. Hua Yang did the modeling and image processing using MATLAB. Ling Li, Chao He, Chong Cheng conducted the XPS, XRD, and TEM tests. Chong Cheng and Rainer Haag conceived and supervised the project.

ZnO/Nanocarbons-Modified Fibrous Scaffolds for Stem Cell-Based Osteogenic Differentiation

Yi Xia, Xin Fan, Hua Yang, Ling Li, Chao He, Chong Cheng,* and Rainer Haag*

Currently, mesenchymal stem cells (MSCs)-based therapies for bone regeneration and treatments have gained significant attention in clinical research. Though many chemical and physical cues which influence the osteogenic differentiation of MSCs have been explored, scaffolds combining the benefits of Zn²⁺ ions and unique nanostructures may become an ideal interface to enhance osteogenic and anti-infective capabilities simultaneously. In this work, motivated by the enormous advantages of Zn-based metal–organic framework-derived nanocarbons, C-ZnO nanocarbons-modified fibrous scaffolds for stem cell-based osteogenic differentiation are constructed. The modified scaffolds show enhanced expression of alkaline phosphatase, bone sialoprotein, vinculin, and a larger cell spreading area. Meanwhile, the caging of ZnO nanoparticles can allow the slow release of Zn²⁺ ions, which not only activate various signaling pathways to guide osteogenic differentiation but also prevent the potential bacterial infection of implantable scaffolds. Overall, this study may provide new insight for designing stem cell-based nanostructured fibrous scaffolds with simultaneously enhanced osteogenic and anti-infective capabilities.

1. Introduction

Because various degenerative bone diseases and inflammatory joint disturb many people all over the world, there is currently an urgent need for the supply of osteogenic and anti-infective scaffolds that provide bone regenerative therapies in the clinic.^[1–8] Mesenchymal stem cells (MSCs) are frequently investigated to differentiate to different kinds of cell lineage, including osteoblasts, they are considered as a good candidate for bone therapy.^[1,4,9–13] Meanwhile, MSCs' differentiation can be driven by the chemical and physical cues at material/cellular interfaces, thus providing a controllable protocol to manipulate the differentiation of MSCs without using complex bio-factors or cellular reprogramming processes.^[14–17] Indeed, chemical cues (metal ions, small molecules, and synthetic extracellular matrix) and phys-

ical cues (stiffness, micro-/nanotopography, and physical adhesion property) can efficiently influence MSCs' functionalities, including regulation of cell adhesion, proliferation, and differentiation.^[18–29] For instance, forces originated from the cell–material interface could change the cell membrane and subsequently affect the cell cytoskeleton, owing to the physical and mechanical interactions between the cells membrane the intracellular mechanoresponsive elements.^[20,30–33] Continuous immersion in Yes-associated protein (YAP) activation culture environments could decrease the human mesenchymal stem cells (hMSCs) multiple differentiation potency and promote osteogenesis.^[19,23]


Due to a variety of unique properties, carbon nanomaterials have been widely investigated as physical cues in tissue scaffolds to regulate stem cell behavior.^[22,34–40] For MSCs, it is suggested that carbon nanomaterials can provide binding sites with high stiffness to cell membrane receptors, and large adsorption and accumulation of nutrients,^[37,38] which may promote the fast formation of focal adhesion (FA). Then it triggers the rearrangement of F-actin and nuclear translocation of the YAP signal, finally improving the nuclear envelope protein Lamin A/C expression and activating the Runt-related transcription factor 2 (RUNX-2) pre-osteogenic marker expression, which eventually enhances the osteogenic differentiation.^[23,41–46] Among diverse kinds of carbon nanomaterials, the Zn-based metal–organic frameworks (MOFs)-derived nanocarbons (C-ZnO) have attracted much interest in the biomedical field.^[47] On the one hand, the large surface area and particular nanostructures of C-ZnO can facilitate the interactions between

Y. Xia, X. Fan, L. Li, Dr. C. He, Prof. C. Cheng
 College of Polymer Science and Engineering
 State Key Laboratory of Polymer Materials Engineering
 Sichuan University
 Chengdu 610065, China
 E-mail: chong.cheng@scu.edu.cn

Y. Xia, X. Fan, Prof. R. Haag
 Department of Chemistry and Biochemistry
 Freie Universität Berlin
 Takustrasse 3, Berlin 14195, Germany
 E-mail: haag@chemie.fu-berlin.de

H. Yang
 Institute of Mechanics
 Chair of Continuum Mechanics and Constitutive Theory
 Technische Universität Berlin
 Einsteinufer 5, Berlin 10587, Germany

L. Li
 Department of Ultrasound
 West China Hospital
 Sichuan University
 Chengdu 610065, China

 The ORCID identification number(s) for the author(s) of this article can be found under <https://doi.org/10.1002/smll.202003010>.

© 2020 The Authors. Published by Wiley-VCH GmbH. This is an open access article under the terms of the Creative Commons Attribution License, which permits use, distribution and reproduction in any medium, provided the original work is properly cited.

DOI: 10.1002/smll.202003010

the material and cell membrane.^[48–52] On the other hand, the Zn²⁺ ions do not only show strong inhibition on the growth of bacteria but also stimulate mineralization and osteoblast proliferation by improving anabolic influence on bone metabolism, thus promoting osteogenic differentiation of MSCs.^[51,53] Therefore, it is suggested that the C-ZnO-based nanocarbons that combine benefits of Zn²⁺ ions and unique nanostructures may become ideal candidates to construct favorable stem cells scaffolds with simultaneously enhanced osteogenic and anti-infective capabilities.

In this work, motivated by their advantages of Zn-based MOF-derived nanocarbons,^[47,52,54,55] we have constructed C-ZnO nanocarbons-modified fibrous scaffolds for stem cell-based osteogenic differentiation. Although ZIF-8 is size-morphology tunable and could contain multiple metal ions, they are not quite stable, especially in the acidic environment. Thus, the ZIF-8 nanostructure was carbonized and oxidized to obtain C-ZnO nanocarbons. The fibrous scaffolds were fabricated via electrospinning of a carrier polymer with C-ZnO nanoadditives. The expression of alkaline phosphatase (ALP) and bone sialoprotein (IBSP), and the calcium deposition test indicate that the engineered scaffolds show better osteogenic properties. The results of enhanced cell spreading area, vinculin expression, and F-actin rearrangement suggest the cell membrane and cytoskeleton sensed the physical cues of the nanostructured scaffolds. The following nuclear translocation of YAP, improved expression of Lamin A/C and RUNX-2 signaling emphasized the role of the C-ZnO in the regulation of cell–matrix interactions during promoting osteogenic differentiation. These detailed investigations confirm that the carbon nanostructures facilitate the adsorption and concentration of nutrients, which offer preferable environments for the growth and differentiation of MSCs. Meanwhile, the caging of ZnO nanoparticles can allow the slow release of Zn²⁺ ions, which not only activates various signaling pathways to guide osteogenic differentiation but also prevents the potential bacterial infection of implantable scaffolds. Overall, this study may provide new insight for designing stem cells-based nanostructured fibrous scaffolds with simultaneously enhanced osteogenic and anti-infective capabilities.

2. Results and Discussion

2.1. Preparation and Characterization of the C-ZnO Nanoparticles

ZIF-8 nanoparticles were prepared using 2-methylimidazole and Zn(NO₃)₂·6H₂O. Then, the ZIF-8 nanoparticles were then carbonized for 2 h at 800 °C with the protection of argon and oxidized for 2 h at 300 °C in air to obtain the C-ZnO nanoparticles (Figure 1a). Scanning electron microscopy (SEM) image in Figure 1b and the energy-dispersive X-ray spectroscopy (EDS) in Figure 1c suggest that C-ZnO nanoparticles are well prepared. Meanwhile, the size and morphology are relatively uniform and homogenous. Transmission electron microscope (TEM) image in Figure 1d exhibits that the sizes are around 50 nm. Moreover, the amplified high-resolution TEM in Figure 1e suggests that abundant ultra-small ZnO nanoparticles (yellow circles) homogeneously distribute on the carbon matrix. Figure 1f presents the high-angle annular

dark-field scanning TEM (HAADF-STEM) picture of C-ZnO and relative elemental mapping data, which proved the homogenous distribution of C, N, O, and Zn elements on nanocarbon. No big ZnO particles can be noticed from the images.

Further characterization of nanocarbons composition and chemical structure was performed by X-ray photoelectron spectroscopy (XPS) and the X-ray diffraction (XRD). The XRD in Figure 1g suggests that the ZIF-8 was successfully prepared. After carbonization and oxidation processes, no obvious peak for ZnO could be noticed, thus indicating that the ZnO doping provides amorphous structures. Moreover, the XPS survey scan in Figure 1h proved the existence of C, N, O, and Zn peaks. The high-resolution XPS C 1s spectra were fitted to four peaks (Figure 1i), which were corresponding to 288.0 eV (O=C–N, O=C–O), 286.5 (C=N, C=O), 285.1 (C–N, C–O), and 284.0 (C–C, C=C). The high-resolution XPS O 1s spectra in Figure 1j were fit to 532.9 (O–C), 531.6 (O=C), and 530.5 eV (O–Zn). As with previous report, Figure 1k shows two characteristic peaks at 1044.7 and 1021.7 eV in the Zn 2p spectra.^[54] Figure 1l suggests the measured atom ratio of C, N, O, and Zn are 62.04, 18.35, 12.55, and 7.04 at%, respectively. According to the data above, it is believed that C-ZnO nanocarbons were successfully synthesized.

Previous literature has already proven that poly(ϵ -caprolactone) (PCL) electrospun fibers were outstanding matrix for osteogenic tissue engineering.^[5,7,56] C-ZnO nanoparticles were incorporated into the fibrous scaffolds to investigate their interactions with hMSCs. As shown in Figure 2a, the obtained PCL/C-ZnO solutions were well dispersed and sucked into a syringe, then the fibers were collected on an aluminum foil when a certain voltage applied between the needle and substrate. As shown in Table S1 in the Supporting Information, the membrane scaffolds were prepared in hexafluoroisopropanol at the concentration of 10%, w/v PCL and 0%, 1%, 2%, and 5%, w/v C-ZnO nanoparticles.

To investigate the difference between bare ZnO nanoparticles and the C-ZnO, the ZnO-blended PCL (PCL-ZnO) with a similar amount of ZnO as that of PCL-ZnO-2 was fabricated. The morphology of the fibrous membrane is shown in Figure 2b and Figure S4 in the Supporting Information. The SEM data suggest that the fibrous scaffolds were composed of randomly overlaid fibers. The digital pictures of the prepared membrane suggest that after being mixed with C-ZnO nanoparticles, the color of the scaffold turns black. Meanwhile, with the increased concentration of the C-ZnO, the membrane scaffolds grow darker. As is shown on amplified SEM images, obvious C-ZnO nanoparticles could be observed on the fiber, which suggests that the C-ZnO nanoparticles were successfully blended into the fibers. The morphology of the scaffolds proved that the C-ZnO nanoparticles were uniformly distributed throughout fibers, and part of nanocarbons was observable on the fiber surface. As shown in Figure 2c, the diameter distribution of the prepared fibers suggests that after the concentration of nanocarbons reaches 2%, w/v, the fiber sizes decreased. The energy dispersive spectrometer data (EDS) and element mapping in Figure 2d,e suggest the abundant existence of Zn after the incorporation of C-ZnO nanoparticles. The water contact angle (WCA) in Figure S6 in the Supporting Information suggests that the pristine PCL fiber membrane is around 131.2°.

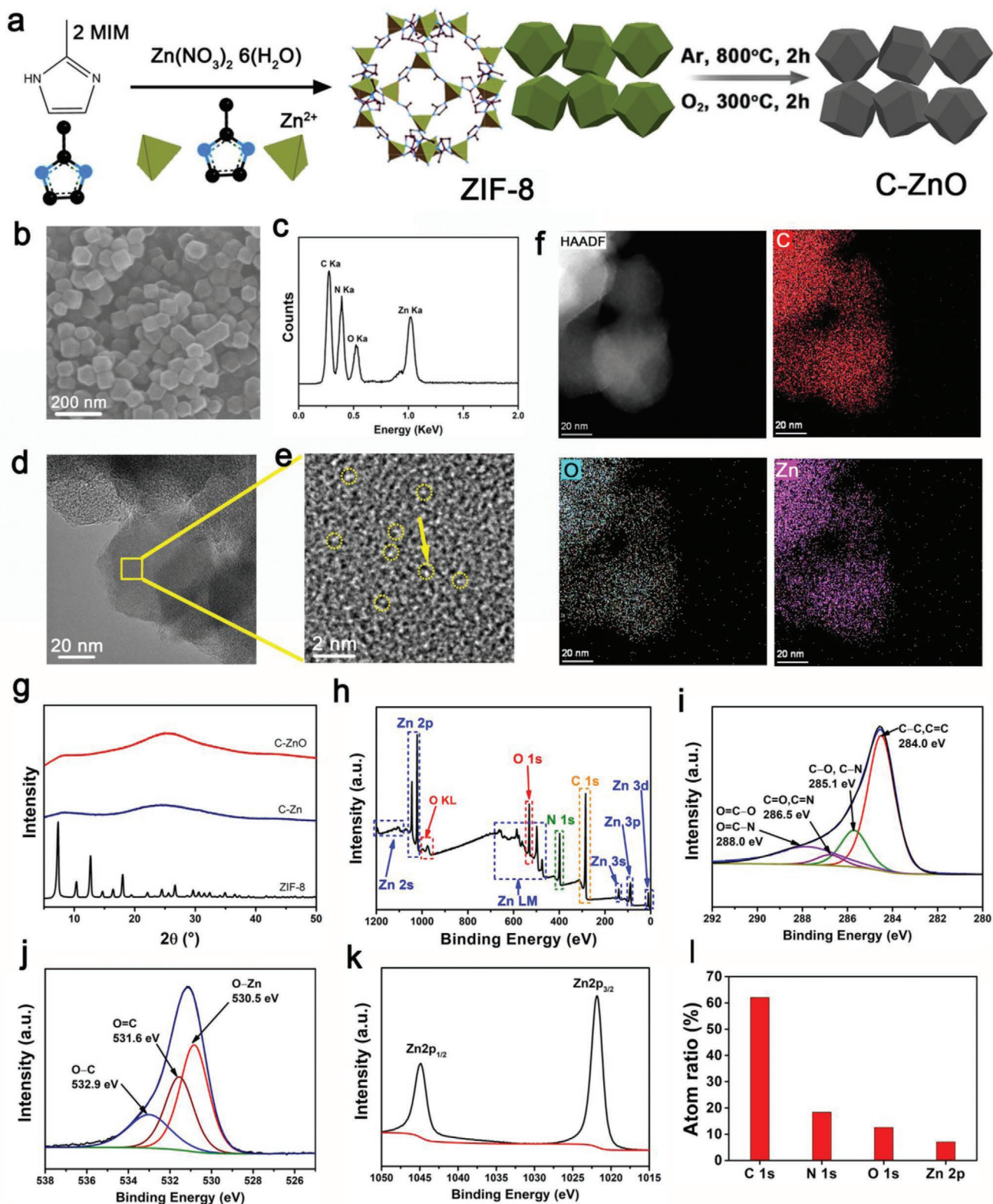


Figure 1. a) The ZIF-8 and C-ZnO preparation process scheme. b) Typical SEM image of the prepared C-ZnO nanoparticles. c) EDS curves of the C-ZnO particle. d) TEM image of the C-ZnO. e) High-resolution TEM image of the C-ZnO. f) HAADF-STEM image and elemental mapping of the C-ZnO. g) XRD spectra of ZIF-8, C-Zn, and C-ZnO nanoparticles. h) XPS survey scanning spectra for C-ZnO. The high-resolution XPS i) C 1s spectra, j) O 1s spectra, and k) Zn 2p spectra for C-ZnO. l) The atom percentages of C, N, O, and Zn in C-ZnO nanoparticles.

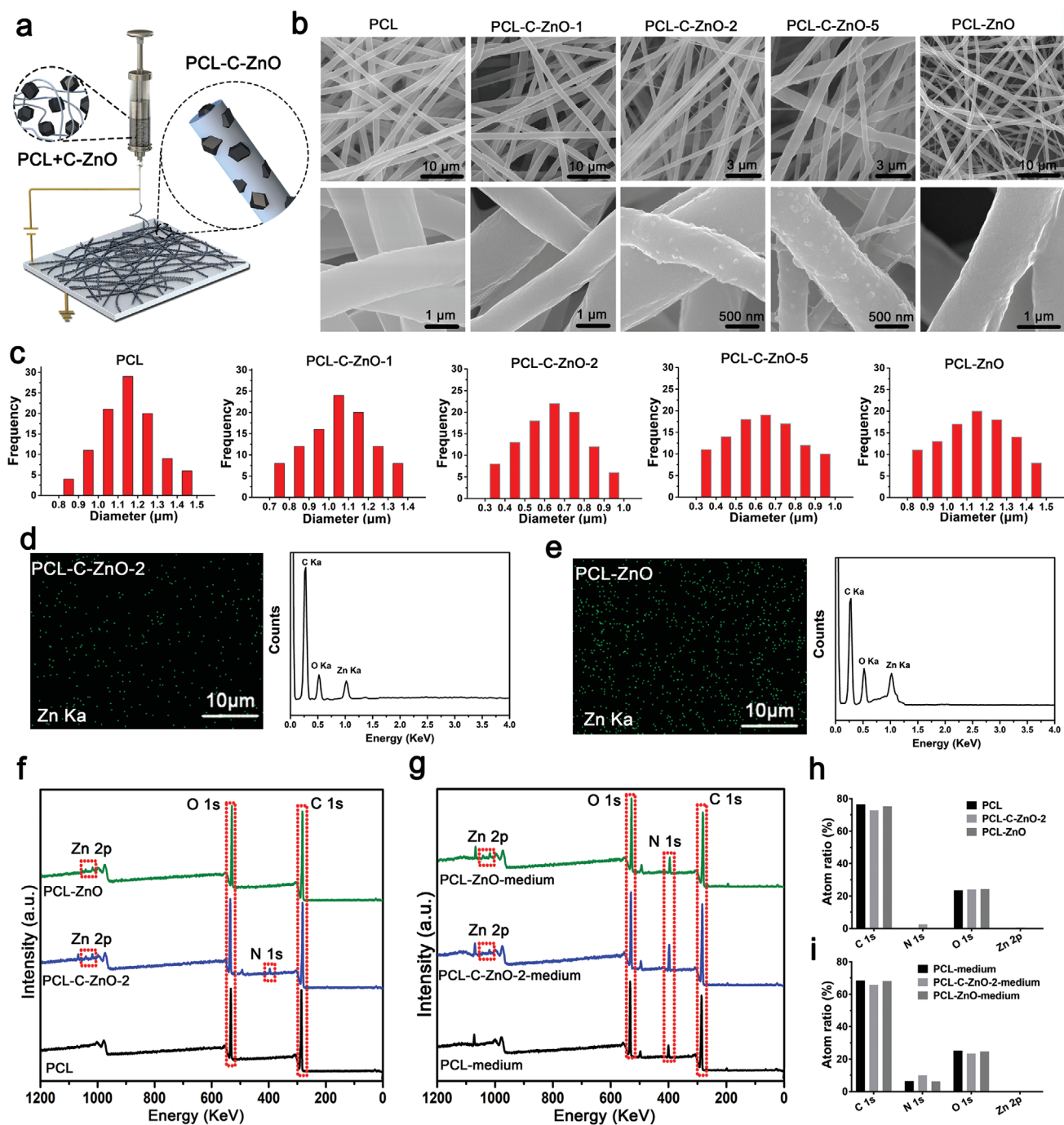


Figure 2. a) Schematic image for the preparation of PCL-C-ZnO nanofibrous scaffolds. b) SEM images for the electrospun bare PCL and PCL-C-ZnO scaffolds. c) The diameter distribution of the electrospun fibers ($n = 100$ fibers were quantified). d,e) The SEM element mapping and EDS curves of the PCL-C-ZnO and PCL-ZnO, respectively. XPS survey scanning spectra for f) fibrous scaffolds and g) cell culture medium immersed scaffolds. h) The atom percentages of C, N, O, and Zn on scaffolds and i) cell culture medium immersed scaffolds.

After the incorporation of C-ZnO nanoparticles, the WCA did not show any significant change between different samples.

To further prove the successful incorporation of C-ZnO and ZnO nanoparticles into PCL fibers, XPS was performed and exhibited in Figure 2f,h. According to the XPS survey scanning spectra, the nitrogen and zinc elements peaks indicate that the nanocarbons are successfully blended into the PCL-C-ZnO

fibers. Meanwhile, the zinc element on PCL-ZnO indicates that ZnO nanoparticles have been successfully coated into PCL fiber. After immersion in the cell culture medium, those contents of N 1s (Figure 2g,i) increased significantly compared to the original membrane nitrogen contents (Figure 2f,h). It is proposed that membranes could absorb diverse nitrogen-containing nutrients such as proteins, peptides, or amino acids

Table 1. Atomic compositions of the nanocarbon-incorporated PCL scaffolds before and after immersed in the cell culture medium, and the data are obtained from the XPS.

| Sample | C 1s [%] | O 1s [%] | N 1s [%] | S 2p [%] | Zn 2p [%] | N/C ratio [%] |
|--------------------|-------------|-------------|-------------|-------------|--------------|------------------|
| PCL | 76.42 | 23.58 | 0 | 0 | 0 | 0 |
| PCL-C-ZnO-2 | 72.92 | 23.91 | 2.56 | 0 | 0.6 | 3.51 |
| PCL-ZnO | 75.25 | 24.39 | 0 | 0 | 0.37 | 0 |
| PCL-medium | 68.37 | 25.17 | 6.46 | 0 | 0 | 9.45 |
| PCL-C-ZnO-2-medium | 65.68 | 23.43 | 10.14 | 0.31 | 1.34 | 15.44 |
| PCL-ZnO-medium | 68.19 | 24.69 | 6.35 | 0.28 | 0.48 | 9.32 |

from the media. As shown in **Table 1**, Compared to the pure PCL membrane, there is no apparent change in the content of N 1s on PCL-ZnO, which means the incorporation of ZnO nanoparticles could not improve the adhesion property. However, the higher content of N 1s on PCL-C-ZnO suggests that nanocarbons could contribute to a higher absorption amount of these nutrient molecules, which could exert beneficial effects on the MSCs growth and differentiation.

The MSCs proliferation activity and viability on the scaffolds were evaluated by cell counting kit-8 (CCK-8) analysis and lived/dead assay kit. The lived/dead cell in **Figure 3a** exhibits that the hMSCs are viable on all samples from the vertical pictures under the confocal microscopy after 3 days of culture. The statistical analysis of the cell numbers on the membrane in **Figure 3b** indicates that the live cell numbers on scaffolds did not change much after incorporation of C-ZnO nanoparticles until the concentration of 2%, w/v. However, the cell number on sample PCL-C-ZnO-5 decreased around 40% compared with pure PCL, which suggests that the increase of Zn²⁺ concentration exerted a negative effect on cell proliferation due to the potential oxidative stress caused by the ZnO.^[5] Meanwhile, all samples exhibited similar cell viability except PCL-C-ZnO-5 (**Figure 3c**). Additionally, the proliferation of hMSCs on scaffolds evaluated by a CCK-8 assay kit (**Figure 3d**) was similar to the results of the live/dead assay. On the first day, cells adhere well on all scaffolds; after 5 days of culture, the proliferation of cells on the PCL-C-ZnO-5 is less than PCL. Meanwhile, PCL-ZnO cell proliferation rate was less than PCL-C-ZnO-2 although the total amount of ZnO was the same, which indicated that the C-ZnO nanoparticles could reduce the release rate of Zn²⁺ ions, which may benefit the cell growth process. In summary, after incorporation of C-ZnO nanocarbons at the concentration of 2%, the hMSCs seeded on scaffolds could survive and proliferate much better than the other samples.

The osteogenic induction function of the scaffolds was further investigated in osteogenic induction media. The ALP expression at previous status was related to bone type matrix deposition, and the subsequent upregulation of other advanced osteoblastic markers was related to bone mineralization. Since the ALP activity is the strongest after 2 weeks of culture, ALP live staining after 14 days of culture was performed and observed with confocal microscopy, whereby the green fluorescence signal indicated the ALP activity. As shown in **Figure 3e**, ALP activity is the strongest on the surface of PCL-C-ZnO-2

compared with other samples. From the relative fluorescence intensity data in **Figure 3g**, it is evident that the incorporation of C-ZnO could improve the ALP expression in cells. Meanwhile, the lower ALP activity on PCL-C-ZnO-5 may mainly due to the fewer cellular metabolism activity compared with sample PCL-C-ZnO-2, which is following the results of cell proliferation. As the ALP activity on PCL-ZnO is less intense compared to PCL-C-ZnO-2, it indicates that the nanocarbon can promote the osteogenic induction as well.

We further used the ALP activity assay kit to quantify the osteogenic marker ALP expression on 7 and 14 days. As is shown in **Figure 3h**, the ALP activity increased after 2 weeks of culture compared to 1 week, which is in accordance with the literature.^[12,19] Meanwhile, the ALP activity on the sample PCL-C-ZnO-2 is also the strongest both at 7 days and 14 days. IBSP is an essential constituent in the bone since it is found to take part in around 8% of noncollagenous proteins in the bone extracellular matrix. The IBSP staining after 21 days is shown in **Figure 3f**; blue is DAPI (4',6-diamidino-2-phenylindole) and the green is the IBSP marker. The relative fluorescence intensity in **Figure 3g** suggests that the PCL-C-ZnO-2 exhibits the best performance compared with other samples. Calcium deposition amount of the MSCs is a significant landmark for the osteogenesis mineralization process, and we tested the calcium deposition on different samples after culturing for 14 and 21 days. **Figure 3i** suggests that the calcium deposition amount results are similar to the ALP and IBSP results. After incorporation of 2% C-ZnO nanocarbons into the fibrous structure, the ALP activity, IBSP expression, and calcium deposition were increased significantly compared with PCL and PCL-C-ZnO-5.

According to the biocompatibility test and osteogenic differentiation results, we found that the scaffolds with 2%, w/v C-ZnO nanocarbons presented the best performance compared with other samples. Therefore, PCL-C-ZnO-2 was chosen to perform the following osteogenic differentiation analysis. As is known that an extracellular matrix environment stimulates a series of cell signals reactions, which could modulate FA formation and cytoskeleton rearrangements. FAs and cytoskeleton protein on the cell-scaffolds interface play a pivotal role in cell motility, spreading, and differentiation via the FA kinase-signaling pathway. Confocal image of immunofluorescence staining with FAs protein (vinculin) and cytoskeleton protein (F-actin) is shown in **Figure 4a**. Blue is nuclear, red is F-actin, and the green represents the vinculin. It is shown that the cell spheroids exhibited highly spread morphologies on PCL-C-ZnO compared with pure PCL and PCL-ZnO. The cytoskeleton protein (F-actin) presents a linear microfilament structure, which supports the whole cell structure. The amplified F-actin (red) and vinculin (green) confocal images in **Figure 4b** suggest that the vinculin protein grows along the cytoskeleton microfilament, which is crucial during the cell spreading. As shown in the schematic illustration in **Figure 4c**, due to larger surface area and the corresponding more binding sites, the carbon nanomaterial structure on fibrous surfaces could improve cell adhesion. The vinculin intensity value along the white line is shown in **Figure 4d**, and the high-value peaks suggest the expression of vinculin protein, the cell vinculin expression signal on PCL-C-ZnO-2 is much more frequent and stronger than that on PCL and PCL-ZnO, which indicates that the incorporation of carbon

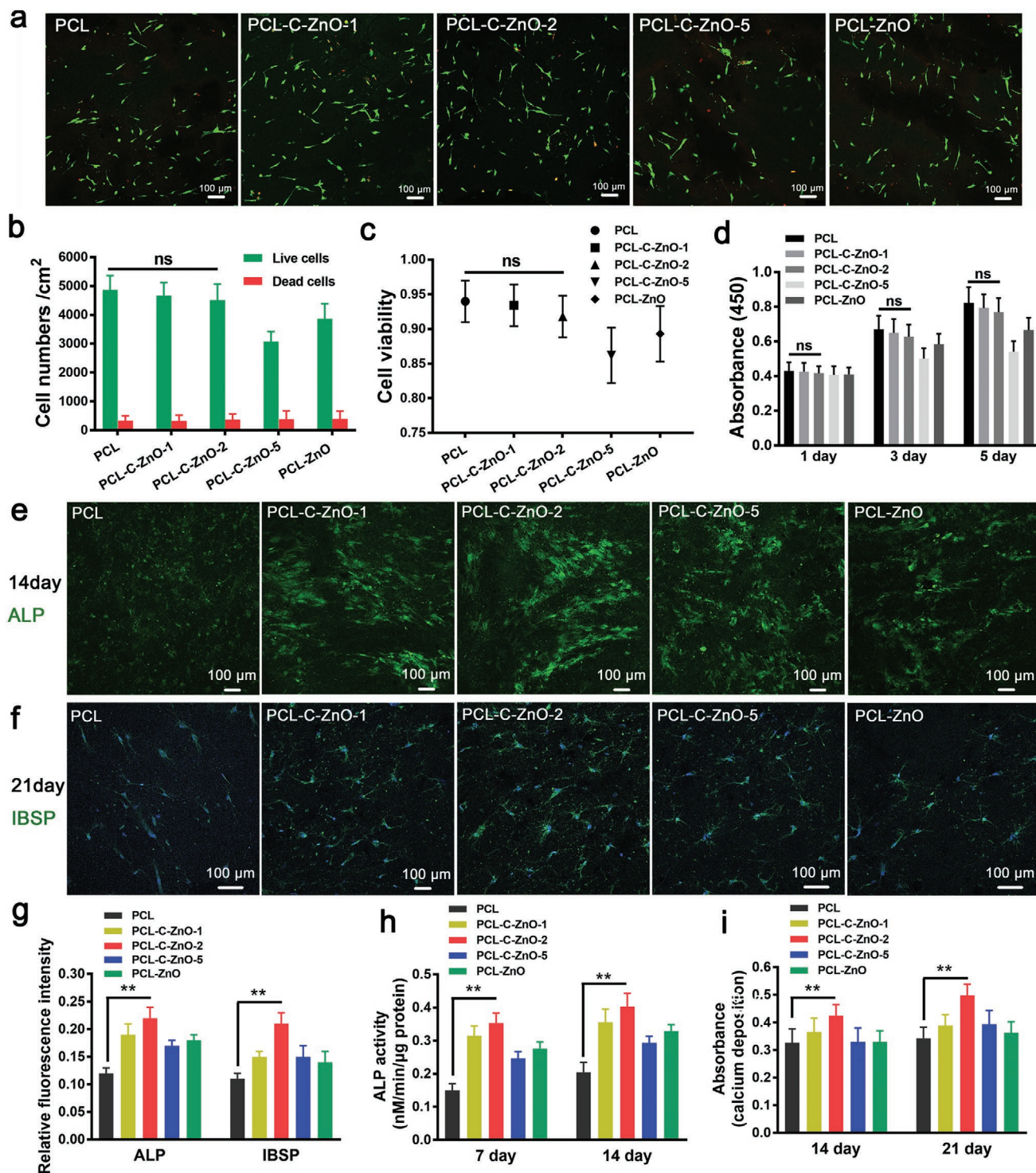


Figure 3. a) Confocal image of live/dead cells (green: live, red: dead) of hMSCs after seeding on different samples for 3 days. b) Quantitative analysis of cell numbers on the scaffolds from the confocal image after 3 days. Statistical quantification of the cell numbers on the surface, n is the number of confocal pictures analyzed (mean \pm SD, $n = 10$). c) Cell viability quantitative analysis according to the live/dead cell numbers (mean \pm SD, $n = 10$). d) The absorbance of live cells after 1, 3, and 5 days culture using the CCK-8 assay kit (mean \pm SD, $n = 6$). e) ALP live-staining of hMSCs after being incubated on the scaffolds for 14 days. f) Fluorescence staining image of mature osteogenic marker IBSP after 21 days of culture on scaffolds (blue is DAPI and green is IBSP). g) The average expressions of ALP and IBSP were quantified according to the fluorescence-stained image intensity (mean \pm SD, $n = 10$). h) Quantitative analysis of ALP activity of hMSCs with osteogenic induction medium for 7 days and 14 days, respectively; the ALP activity was normalized against the $\mu\text{mol}/\text{assay time}/\text{mg}$ protein (mean \pm SD, $n = 6$); i) quantitative analysis of calcium deposition assay with osteogenic induction medium after 14 days and 21 days of culture, respectively (mean \pm SD, $n = 6$), ** $p < 0.01$. NS, not significant.

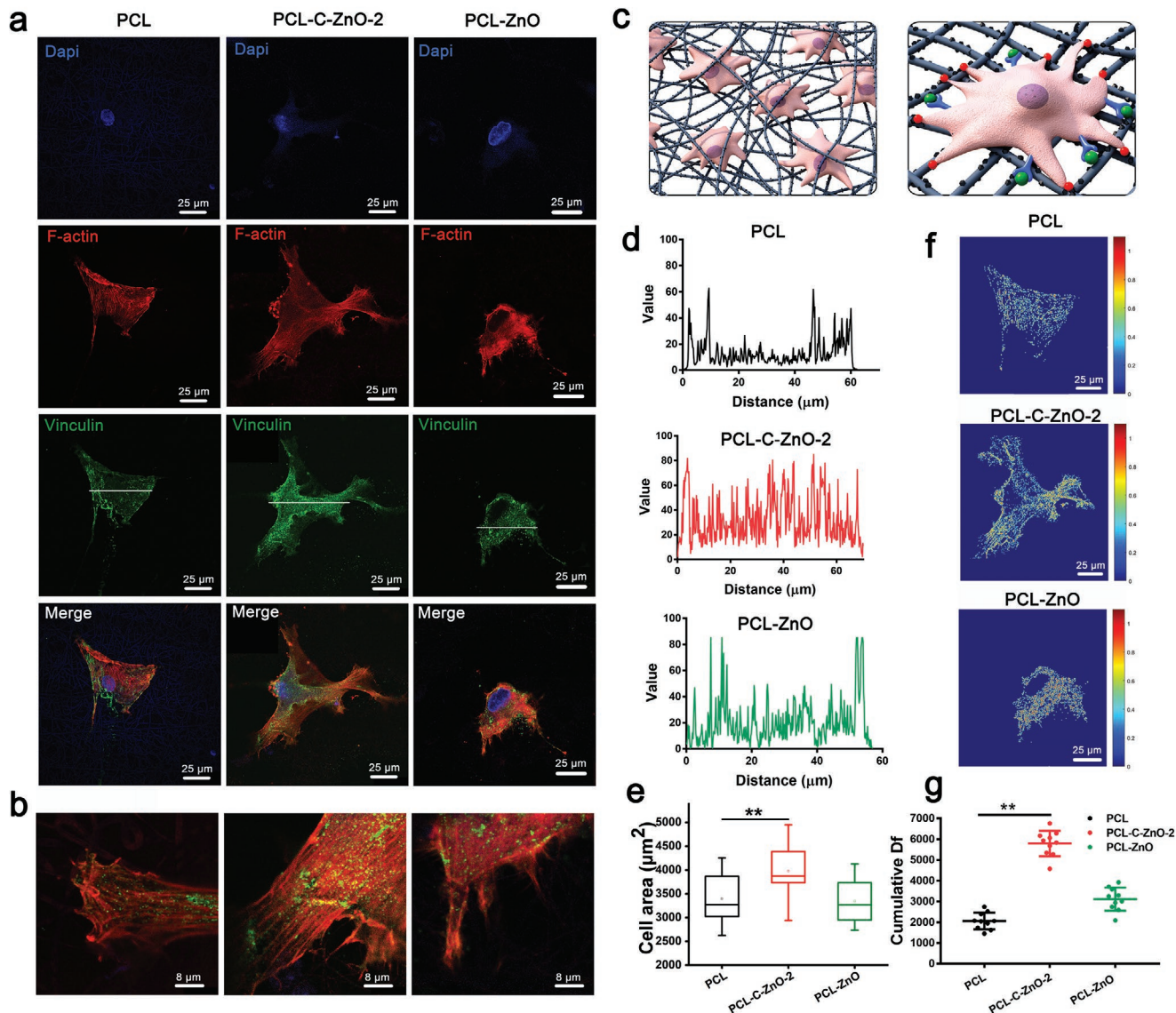


Figure 4. a) Confocal image of hMSCs growth on samples in growth medium; cells were stained with nuclei (blue), vinculin (green), and F-actin (red). b) Amplified confocal cell images in (a). c) Schematic illustration of scaffolds with nanoscale architectures on the fiber surface have larger surface area and thus providing more binding sites for protein to adsorb. d) The vinculin intensity distribution profiles along the white line based on the immunostaining image in (a) on sample PCL, PCL-C-ZnO-2, and PCL-ZnO, respectively. e) Quantitative analysis of the cell spreading area on different samples ($n = 50$). f) Matlab analysis of the 2D fractal dimension (Df) based on F-actin staining. g) Statistic quantification of the cell area according to the F-actin staining and cumulative Df value of a cell ($n = 10$). ** $p < 0.01$.

nanomaterials can offer more binding sites for FAs to promote cell adhesion and motility. According to the SEM images of MSCs on scaffolds (Figure S8, Supporting Information), there is more pseudopodium on the surface of PCL-C-ZnO-2 compared with bare PCL scaffold, which proves that C-ZnO nanocarbons-modified fibrous scaffolds could improve the cells adhesion.

Moreover, correlative cell area analysis (Figure 4e) showed that the hMSCs grown on a carbon nanomaterials-incorporated surface were more significant than those on pure PCL. FAs' size markedly increased on PCL-C-ZnO-2 suggesting that the cell size and shape are related to cell-scaffolds interaction and cell-cell interaction. So fractal dimension analysis was utilized

to quantify cytoskeletal spatial arrangement and density changes on different surfaces.^[12,57,58] Figure 4f suggests that the cytoskeleton arrangement was described by a fractal dimension (Df). Through investigation and quantification analysis of the cytoskeleton distribution, the Df values on PCL-C-ZnO-2 were significantly higher than those on PCL (Figure 4g). Moreover, no obvious differences were observed between PCL and PCL-ZnO. Results suggested that the cell spheroids on carbon nanomaterials-modified PCL fibers could quickly facilitate the mature FA formation and promote the cytoskeleton rearrangement, which improves the cell adhesion to the scaffolds and cell motility, thus could further lead to increase of the osteogenic differentiation.^[43]

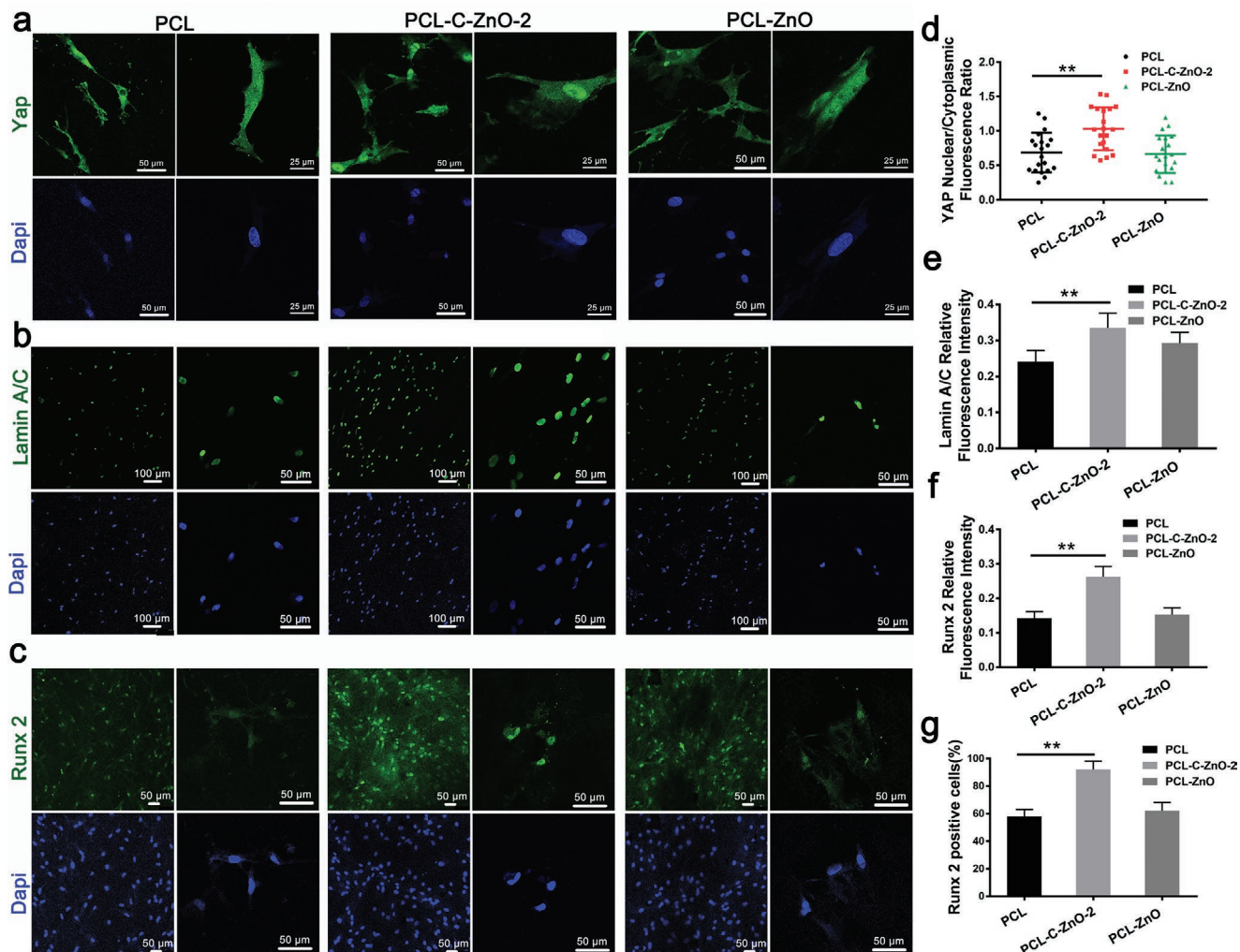


Figure 5. a) Immunofluorescence staining of the YAP signal in hMSCs for 7 days (DAPI, blue; YAP, green). b) Immunofluorescence staining of the Lamin A/C in hMSCs for 7 days (DAPI, blue; RUNX2, green). c) Immunofluorescence staining of the RUNX2 in hMSCs for 7 days in osteogenic culture medium (DAPI, blue; RUNX2, green). d) Quantitative analysis of the YAP nuclear/cytoplasmic fluorescence intensity ratio ($n = 20$). e) Relative fluorescence intensity analysis of Lamin A/C (mean \pm SD, $n = 50$); f) relative fluorescence intensity analysis of RUNX2 (mean \pm SD, $n = 50$); g) quantitative analysis of the RUNX2-positive cells percentage on different scaffolds (mean \pm SD, $n = 50$); ** $p < 0.01$, significant difference.

Many studies have shown that the cytoskeletal tension could trigger the translocation of subcellular transcriptional coactivator YAP, the successive activation of genetic signaling pathway could lead to the osteogenic specification. In this article, the role of YAP location was investigated using immunofluorescence staining of YAP in hMSC spheroids; **Figure 5a** suggests that the YAP signal on the PCL-C-ZnO-2 was more concentrated in nuclear. The statistical analysis of the nuclear/cytoplasmic ratio in **Figure 5d** suggests that the YAP protein on PCL-C-ZnO-2 was twofold more concentrated than that on PCL and PCL-ZnO, which suggested that carbon nanomaterials played an important role in the translocation of nuclear YAP. However, no obvious differences were observed between PCL and PCL-ZnO. Moreover, Lamin A/C, a protein found in the inner nuclear envelope, played a pivotal role in the interaction between nuclear events and cytoplasmic signaling. Previous results suggest that the cytoskeleton rearrangement and FA changes could alter the signal of nuclear envelope protein Lamin A/C.

This protein was stained and observed in **Figure 5b**, whereby it is found that the nuclear of the cells grown on different samples was mostly round and no obvious nuclear morphology changes could be observed. However, the relative fluorescence intensity in **Figure 5e** suggests that the increased expression of Lamin A/C on PCL-C-ZnO-2, which proves the incorporation of nanocarbons could trigger the nuclear envelope protein change. In addition, the pre-osteogenic biomarker RUNX2 was stained and observed with confocal microscopy. The fluorescent images in **Figure 5c** exhibited that the pre-osteogenic marker RUNX2 can be co-activated with YAP and Lamin A/C on PCL-C-ZnO-2. Meanwhile, the quantitative immunostaining analysis in **Figure 5f** suggests that the relative fluorescence intensity for RUNX2 on PCL-C-ZnO-2 was much stronger than that on PCL. Moreover, **Figure 5g** indicates that almost 100% of hMSCs are RUNX2 signal positive after 7 days of culture on PCL-C-ZnO; however, the RUNX2 positive cells on PCL are only around 60%. In the collection, results suggest that YAP subcellular

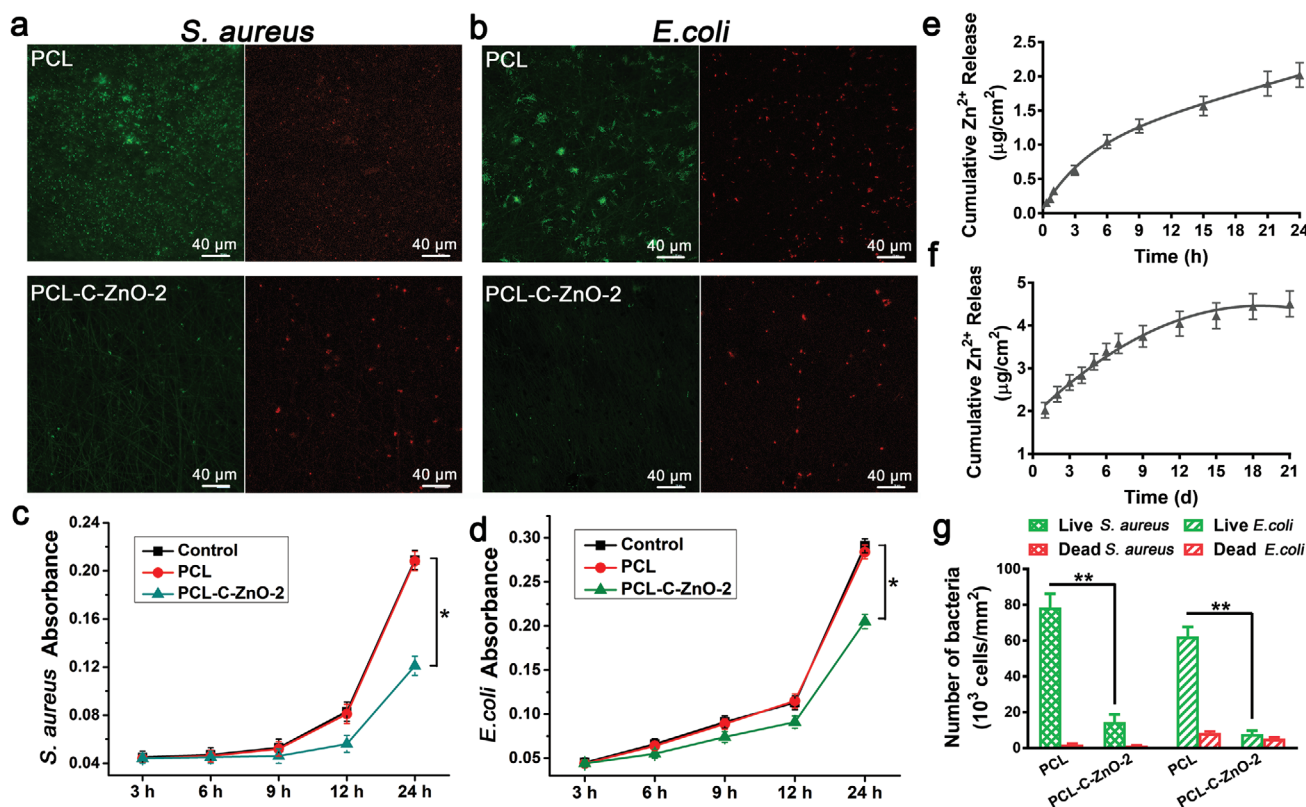


Figure 6. Live/dead staining images (red: dead, green: live) for a) *S. aureus* and b) *E. coli* after incubated with PCL and PCL-C-ZnO-2, respectively. c,d) Real-time OD₆₀₀ values with *S. aureus* and *E. coli*, respectively (mean ± SD, n = 5). e,f) Zn²⁺ ions short-term and long-term release of the PCL-C-ZnO-2. g) Quantitative analysis of live/dead bacteria numbers on the membrane. The numbers were estimated from fluorescent photographs (mean ± SD, n = 5). *p < 0.05, **p < 0.01.

localization and activity and nuclear envelope protein Lamin A/C could be influenced by carbon nanomaterials and used further to promote the expression of intranuclear RUNX2 transcription, which leads to the pre-osteogenic differentiation.

Bacterial infections accompany with scaffolds contamination are a crucial complexity primarily due to the improper delivery methods of biofactor and bacterial infections related to surgery. Supplementary implant scaffolds that could combine bacterial inhibition and osteogenic induction are of both clinical and scientific importance. In order to further investigate the antibacterial property of the C-ZnO nanocarbons modified with PCL scaffolds, gram-negative *E. coli* (ATCC 6538) and Gram-positive *S. aureus* (ATCC 25922) were chosen to perform the bacterial inhibition tests of the engineered membrane. The live/dead staining results of *S. aureus* after 12 h of incubation in Figure 6a suggest that many live bacteria grow on PCL. However, few bacteria were found on PCL-C-ZnO-2. Figure 6b shows the live/dead staining image of *E. coli* cultured on PCL-C-ZnO-2 after 6 h of incubation, it is obvious that the incorporation of C-ZnO nanoparticles endows the membrane with bacterial inhibition properties. However, bare PCL failed to show any antibacterial property, as the live bacteria grow quickly on the surface. Meanwhile, the statistical analysis of live dead cell numbers on the scaffolds in Figure 6g suggests that live *S. aureus* and *E. coli* numbers on PCL are around fourfolds and fivefolds larger than that on PCL-C-ZnO-2, respectively.

To further investigate the antibacterial property in medium, we tested the bacterial growth concentration along with time. As is shown in Figure 6c,d, when co-cultured with PCL-C-ZnO-2, the concentration increased along with bacterial growth in the medium, which was much slower than that with PCL and pure medium. After co-culture for 24 h, the amount of *S. aureus* and *E. coli* in PCL co-cultured medium was around two-folds and 1.5-folds more significant than that in PCL-C-ZnO-2 co-cultured medium, respectively. The bacterial concentration in the sample co-cultured medium suggests that PCL-C-ZnO-2 has not only bacterial inhibition properties on its surface but also exhibits antibacterial property in the surrounding environment. To verify the release capabilities of Zn²⁺ ions, the long-term and short-term release of Zn²⁺ ions of PCL-C-ZnO-2 were characterized (Figure 6e,f). During the first 6 h, Zn²⁺ ions release was very fast and the subsequent release rates were slowing down moderately. The release of Zn²⁺ ions plays a pivotal role in both bacterial killing and osteogenic differentiation.

3. Conclusion

In summary, we have constructed a novel nanocarbon-structured fibrous scaffold for stem cell-based osteogenic differentiation, which combines both physical characteristics (nanotopography) and chemical characteristics (gradual

release of the Zn²⁺ ions) in promoting osteogenic differentiation. The C-ZnO-modified scaffolds show enhanced expression of ALP, IBSP, vinculin, and a larger cell spreading area. The following nuclear translocation of YAP, improved expression of Lamin A/C and RUNX-2 signaling indicate the important role of the C-ZnO nanocarbons in promoting osteogenic differentiation. Meanwhile, the caging of ZnO nanoparticles can allow the slow release of Zn²⁺ ions, which not only activate various signaling pathways to guide osteogenic differentiation but also prevent the potential bacterial infection during implantable applications. Overall, this study may provide new insight for designing stem cells-based nanostructured fibrous scaffolds with simultaneously enhanced osteogenic and anti-infective capabilities.

Supporting Information

Supporting Information is available from the Wiley Online Library or from the author.

Acknowledgements

This work was financially sponsored by the National Key R&D Program of China (2019YFA0110600, 2019YFA0110601) and Deutsche Forschungsgemeinschaft (DFG) through grants from the Collaborative Research Center (SFB) 765. Y.X. and X.F. acknowledge the support from China Scholarship Council (CSC). C.C. acknowledges the support of the State Key Laboratory of Polymer Materials Engineering (No. sklpme2019-2-03), the Science and Technology Project of Sichuan Province (nos. 2020YFH0087 and 2020YJ0055), Fundamental Research Funds for the Central Universities, Thousand Youth Talents Plan, Alexander von Humboldt Fellowship, Special Funds for Prevention and Control of COVID-19 of SKLFPM, Donghua University (YJ202005) and Sichuan University (2020scunCoV-YJ-20005), and DRS POINT Fellowship. L.L. thanks the support of Key Laboratory of Emergency and Trauma, Ministry of Education (No. KLET-201907). Dr. Pamela Winchester is sincerely acknowledged for language polishing the manuscript. The authors acknowledge the assistance of the Core Facility BioSupraMol in Freie Universität Berlin and the bacterial lab at Sichuan University. The authors also acknowledge their laboratory members for their generous help. Open access funding enabled and organized by Projekt DEAL.

Conflict of Interest

The authors declare no conflict of interest.

Keywords

anti-infective surfaces, carbon nanomaterials, metal-organic frameworks, nanostructured fibrous scaffolds, osteogenic surfaces, stem cells

Received: May 13, 2020

Revised: July 4, 2020

Published online: August 19, 2020

[1] C. M. Madl, S. C. Heilshorn, H. M. Blau, *Nature* **2018**, *557*, 335.

[2] A. Trounson, C. McDonald, *Cell Stem Cell* **2015**, *17*, 11.

- [3] S. Pina, J. M. Oliveira, R. L. Reis, *Adv. Mater.* **2015**, *27*, 1143.
- [4] C. M. Curtin, G. M. Cuniffe, F. G. Lyons, K. Bessho, G. R. Dickson, G. P. Duffy, F. J. O'Brien, *Adv. Mater.* **2012**, *24*, 749.
- [5] A. Nasajpour, S. Ansari, C. Rinoldi, A. S. Rad, T. Aghaloo, S. R. Shin, Y. K. Mishra, R. Adelung, W. Swieszkowski, N. Annabi, A. Khademhosseini, A. Moshaverinia, A. Tamayol, *Adv. Funct. Mater.* **2018**, *28*, 1703437.
- [6] K. Huo, X. Zhang, H. Wang, L. Zhao, X. Liu, P. K. Chu, *Biomaterials* **2013**, *34*, 3467.
- [7] H. Yoshimoto, Y. M. Shin, H. Terai, J. P. Vacanti, *Biomaterials* **2003**, *24*, 2077.
- [8] N. S. Yadavalli, D. Asheghali, A. Tokarev, W. Zhang, J. Xie, S. Minko, *Small* **2020**, *16*, 1907422.
- [9] X. Wang, B. Ding, B. Li, *Mater. Today* **2013**, *16*, 229.
- [10] T. C. von Erlach, S. Bertazzo, M. A. Wozniak, C.-M. Horejs, S. A. Maynard, S. Attwood, B. K. Robinson, H. Autefage, C. Kallepitis, A. del Río Hernández, C. S. Chen, S. Goldoni, M. M. Stevens, *Nat. Mater.* **2018**, *17*, 237.
- [11] M. F. Pittenger, A. M. Mackay, S. C. Beck, R. K. Jaiswal, R. Douglas, J. D. Mosca, M. A. Moorman, D. W. Simonetti, S. Craig, D. R. Marshak, *Science* **1999**, *284*, 143.
- [12] J. Zhang, H. Yang, B. E. Abali, M. Li, Y. Xia, R. Haag, *Small* **2019**, *15*, 1901920.
- [13] Y. Hou, W. Xie, L. Yu, L. C. Camacho, C. Nie, M. Zhang, R. Haag, Q. Wei, *Small* **2020**, *16*, 1905422.
- [14] L. Li, J. Eyckmans, C. S. Chen, *Nat. Mater.* **2017**, *16*, 1164.
- [15] J. E. Frith, G. D. Kusuma, J. Carthew, F. Li, N. Cloonan, G. A. Gomez, J. J. Cooper-White, *Nat. Commun.* **2018**, *9*, 257.
- [16] X. Zhang, J. Nie, X. Yang, Z. Liu, W. Guo, J. Qiu, S. Wang, X. Yu, Y. Guan, H. Liu, L. Li, *Appl. Mater. Today* **2018**, *10*, 164.
- [17] E. S. Place, J. H. George, C. K. Williams, M. M. Stevens, *Chem. Soc. Rev.* **2009**, *38*, 1139.
- [18] A. Higuchi, Q.-D. Ling, Y. Chang, S.-T. Hsu, A. Umezawa, *Chem. Rev.* **2013**, *113*, 3297.
- [19] J. Zhang, C. Cheng, J. L. Cuellar-Camacho, M. Li, Y. Xia, W. Li, R. Haag, *Adv. Funct. Mater.* **2018**, *28*, 1804773.
- [20] C. Yang, M. W. Tibbitt, L. Basta, K. S. Anseth, *Nat. Mater.* **2014**, *13*, 645.
- [21] J. Lee, A. A. Abdeen, D. Zhang, K. A. Kilian, *Biomaterials* **2013**, *34*, 8140.
- [22] K. Alberti, R. E. Davey, K. Onishi, S. George, K. Salchert, F. P. Seib, M. Bornhäuser, T. Pompe, A. Nagy, C. Werner, P. W. Zandstra, *Nat. Methods* **2008**, *5*, 645.
- [23] S. W. Crowder, V. Leonardo, T. Whittaker, P. Papathanasiou, M. M. Stevens, *Cell Stem Cell* **2016**, *18*, 39.
- [24] M. J. Dalby, M. J. P. Biggs, N. Gadegaard, G. Kalna, C. D. W. Wilkinson, A. S. G. Curtis, *J. Cell. Biochem.* **2007**, *100*, 326.
- [25] Y. Hou, L. Yu, W. Xie, L. C. Camacho, M. Zhang, Z. Chu, Q. Wei, R. Haag, *Nano Lett.* **2020**, *20*, 748.
- [26] R. Kumar, A. Bonicelli, S. Sekula-Neuner, A. C. B. Cato, M. Hirtz, H. Fuchs, *Small* **2016**, *12*, 5330.
- [27] M. J. Landry, F.-G. Rollet, T. E. Kennedy, C. J. Barrett, *Langmuir* **2018**, *34*, 8709.
- [28] M. J. Landry, K. Gu, S. N. Harris, L. Al-Alwan, L. Gutsin, D. De Biasio, B. Jiang, D. S. Nakamura, T. C. Corkery, T. E. Kennedy, C. J. Barrett, *Macromol. Biosci.* **2019**, *19*, 1900036.
- [29] J. Xue, T. Wu, J. Li, C. Zhu, Y. Xia, *Angew. Chem., Int. Ed.* **2019**, *58*, 3948.
- [30] R. J. Wade, E. J. Bassin, W. M. Gramlich, J. A. Burdick, *Adv. Mater.* **2015**, *27*, 1356.
- [31] C. S. Hansel, S. W. Crowder, S. Cooper, S. Gopal, M. João Pardelha da Cruz, L. de Oliveira Martins, D. Keller, S. Rothery, M. Becce, A. E. G. Cass, C. Bakal, C. Chiappini, M. M. Stevens, *ACS Nano* **2019**, *13*, 2913.

- [32] Y. Hou, W. Xie, K. Achazi, J. L. Cuellar-Camacho, M. F. Melzig, W. Chen, R. Haag, *Acta Biomater.* **2018**, *77*, 28.
- [33] J. Deng, C. Zhao, J. P. Spatz, Q. Wei, *ACS Nano* **2017**, *11*, 8282.
- [34] A. J. Andersen, J. T. Robinson, H. Dai, A. C. Hunter, T. L. Andresen, S. M. Moghimi, *ACS Nano* **2013**, *7*, 1108.
- [35] T. Zhang, N. Li, K. Li, R. Gao, W. Gu, C. Wu, R. Su, L. Liu, Q. Zhang, J. Liu, *Carbon* **2016**, *105*, 233.
- [36] X. Zhou, M. Nowicki, H. Cui, W. Zhu, X. Fang, S. Miao, S.-J. Lee, M. Keidar, L. G. Zhang, *Carbon* **2017**, *116*, 615.
- [37] Y. Xia, S. Li, C. Nie, J. Zhang, S. Zhou, H. Yang, M. Li, W. Li, C. Cheng, R. Haag, *Appl. Mater. Today* **2019**, *16*, 518.
- [38] S. Marchesan, K. Kostarelos, A. Bianco, M. Prato, *Mater. Today* **2015**, *18*, 12.
- [39] C. Cheng, J. Zhang, S. Li, Y. Xia, C. Nie, Z. Shi, J. L. Cuellar-Camacho, N. Ma, R. Haag, *Adv. Mater.* **2018**, *30*, 1705452.
- [40] C. Cheng, S. Li, A. Thomas, N. A. Kotov, R. Haag, *Chem. Rev.* **2017**, *117*, 1826.
- [41] M. M. Stevens, J. H. George, *Science* **2005**, *310*, 1135.
- [42] J. Swift, I. L. Ivanovska, A. Buxboim, T. Harada, P. C. D. P. Dingal, J. Pinter, J. D. Pajerowski, K. R. Spinler, J.-W. Shin, M. Tewari, F. Rehfeldt, D. W. Speicher, D. E. Discher, *Science* **2013**, *341*, 1240104.
- [43] R. McBeath, D. M. Pirone, C. M. Nelson, K. Bhadriraju, C. S. Chen, *Dev. Cell* **2004**, *6*, 483.
- [44] L. Hanson, W. Zhao, H.-Y. Lou, Z. C. Lin, S. W. Lee, P. Chowdary, Y. Cui, B. Cui, *Nat. Nanotechnol.* **2015**, *10*, 554.
- [45] T. O. Ihalainen, L. Aires, F. A. Herzog, R. Schwartlander, J. Moeller, V. Vogel, *Nat. Mater.* **2015**, *14*, 1252.
- [46] D.-H. Kim, D. Wirtz, *Biomaterials* **2015**, *48*, 161.
- [47] J. Yang, Y. W. Yang, *Small* **2020**, *16*, 1906846.
- [48] S. Keskin, S. Kizilel, *Ind. Eng. Chem. Res.* **2011**, *50*, 1799.
- [49] C. He, D. Liu, W. Lin, *Chem. Rev.* **2015**, *115*, 11079.
- [50] J. Zhuang, C.-H. Kuo, L.-Y. Chou, D.-Y. Liu, E. Weerapana, C.-K. Tsung, *ACS Nano* **2014**, *8*, 2812.
- [51] M. Yu, D. You, J. Zhuang, S. Lin, L. Dong, S. Weng, B. Zhang, K. Cheng, W. Weng, H. Wang, *ACS Appl. Mater. Interfaces* **2017**, *9*, 19698.
- [52] P. Horcajada, R. Gref, T. Baati, P. K. Allan, G. Maurin, P. Couvreur, G. Férey, R. E. Morris, C. Serre, *Chem. Rev.* **2012**, *112*, 1232.
- [53] B. H. Neufeld, M. J. Neufeld, A. Lutzke, S. M. Schweickart, M. M. Reynolds, *Adv. Funct. Mater.* **2017**, *27*, 1702255.
- [54] X. Fan, F. Yang, J. Huang, Y. Yang, C. Nie, W. Zhao, L. Ma, C. Cheng, C. Zhao, R. Haag, *Nano Lett.* **2019**, *19*, 5885.
- [55] Y. Yang, Y. Deng, J. Huang, X. Fan, C. Cheng, C. Nie, L. Ma, W. Zhao, C. Zhao, *Adv. Funct. Mater.* **2019**, *29*, 1900143.
- [56] J. Xue, T. Wu, Y. Dai, Y. Xia, *Chem. Rev.* **2019**, *119*, 5298.
- [57] W. Qian, L. Gong, X. Cui, Z. Zhang, A. Bajpai, C. Liu, A. B. Castillo, J. C. M. Teo, W. Chen, *ACS Appl. Mater. Interfaces* **2017**, *9*, 41794.
- [58] G. Alhoussein, A. Shanti, I. A. H. Farhat, S. B. H. Timraz, N. S. A. Alwahab, Y. E. Pearson, M. N. Martin, N. Christoforou, J. C. M. Teo, *Cytoskeleton* **2016**, *73*, 221.

Supporting Information

ZnO/Nanocarbons-Modified Fibrous Scaffolds for Stem Cell-based Osteogenic Differentiation

Yi Xia, Xin Fan, Hua Yang, Ling Li, Chao He, Chong Cheng, and Rainer Haag**

1.1 Materials

All chemicals were purchased from Sigma (Steinheim, Germany) unless stated, including dimethylformamide (DMF, CAS: 68-12-2), $Zn(NO_3)_2 \cdot 6H_2O$ (CAS: 10196-18-6), and 2-methylimidazole (CAS: 693-98-1). The deionized water used was purified using a Millipore water purification system with minimum resistivity of 18.0 $M\Omega \cdot cm$. Dialysis was performed in benzoylated cellulose tubes from Sigma-Aldrich (D7884, width: 32 mm, molecular weight cut-off (MWCO) 2000 $g \cdot mol^{-1}$). Dulbecco's phosphate-buffered saline (DPBS, no calcium, no magnesium) and all other chemicals for stem cell culture and viability tests were purchased from Thermofisher.

1.2 Characterization methods

Scanning electron microscope (SEM): The morphology of the C-ZnO nano-compounds and embedded substrates was observed by ultrahigh-resolution FE-SEM (Hitachi SU8200). The samples were dried in an oven and then attached to the sample supports using carbon tape. C-ZnO nano compounds were observed directly without gold coating due to the excellent conductivity. For the non-conductive substrates, the gold coating was deposited with about 1-2 nm.

Transmission electron microscopy (TEM): Droplets ($\sim 5 \mu L$, $\sim 0.02 mg/mL$) of the sample solution were placed on ultrathin carbon film on copper grids (Ted Pella, Inc.

USA) and the supernatant liquid was removed by blotting with a piece of filter paper. The grids were allowed to air dry at least 40 min and were subsequently transferred into a TEM machine, Tecnai G2 F20 S-TWIN transmission electron microscope (FEI Ltd., USA), and operated at 200 kV. The high-angle annular dark-field scanning transmission electron microscopy (HAADF-STEM), energy-dispersive X-ray spectroscopy (EDS), the amplified high resolution TEM has been performed by the same machine.

X-ray photoelectron spectroscopy (XPS): XPS was measured on K-Alpha™ + X-ray photoelectron spectrometer system (Thermo Scientific) with hemispheric 180° dual-focus analyzer with 128-channel detector. X-ray monochromator is micro-focused Al-K α radiation. For the measurement, the powder samples were pressed and loaded on carbon taps, then pasted onto the sample holder for measurement. The data was collected with X-ray spot size of 400 μ m, 20 scans for the survey, and 50 scans for regions. Survey spectra were run in the binding energy range of 0-1000 eV, and high-resolution spectra of C1s, N1s, O1s, and Zn2p were collected. The XPS spectra of C-ZnO nano compounds and embedded substrates were conducted by a similar method.

Water contact angle (WCA): Static contact angle measurements were performed by using a contact angle goniometer (Data Physics Instruments, Germany) with the sessile drop method. A liquid drop of 2 μ L Milli-Q water was placed on the substrate and allowed to equilibrate for 15 s at room temperature. At least eight measurements were averaged on every five parallel samples to get a reliable value.

1.3 Preparation of zeolitic imidazolate framework (ZIF-8) and C-ZnO

First, Zn(NO₃)₂·6H₂O (3.39 g) and 2-methylimidazole (3.152 g) were dissolved in 300 mL methanol, respectively. Then two solutions were mixed and maintained at room temperature for 24 h. The final products were washed with methanol and ethanol for 3 times and then dried in vacuum to obtain Zeolitic imidazolate framework (ZIF-8). The ZIF-8 nanoparticles were subjected to a thermal activation at a temperature of 800 °C

under Ar flow for 2 h with a heating speed of 5 °C per min in a tube furnace to obtain the C-Zn nanocarbons. Finally, the C-Zn nanocarbons were oxidized to C-ZnO nanocarbons at a temperature of 300 °C under airflow for 2 h with a heating speed of 1 °C per min in a tube furnace.

1.4 Fabrication of C-ZnO nanocarbons embedded polycaprolactone (PCL) fibers

PCL (80 kDa, Sigma) was dissolved in 1,1,1,3,3,3-hexafluoro-2-propanol (HFIP) to prepare a 10% (1 g in 10 mL, w/v) polymer solution. C-ZnO nanocarbons were added to the PCL polymer solution at the different concentrations shown in Table 1. The polymer solution was placed into a syringe with a metal needle and then electrospun onto an aluminum foil-wrapped drum collector, which was positioned horizontally, at a flow rate of 2 mL/h. 18 kV voltage was applied with a high voltage power supply and a 12 cm working distance was utilized. The PCL-C-ZnO fibers were dried under vacuum overnight and then peeled off from the aluminum foil for further usage. The embedded substrates were then vacuum dried overnight. The obtained fibers were then characterized by SEM, EDS Mapping, XPS, and WCA.

1.5 Stem cell culture and bioactivity characterizations

Cell culture. Human mesenchymal stem cells (hMSC) were purchased from Lonza, USA. The necessary approval before carrying out MSC-related experiments was obtained from the Department of Biology, Chemistry, and Pharmacy, Freie Universität Berlin. The cell thawing and proliferation were carried out in DMEM medium with 10% FBS, then cells were maintained at 37 °C in a saturated humidity atmosphere containing 95% air and 5% CO₂. The cells were passaged and collected with Accutase (Thermo Fisher) after reaching 70-80% confluency.

Cytocompatibility. The harvested cells were seeded on 48-well plates on fiber surface

at the density of 5×10^3 cells/cm². The viability of cells was assessed after 3 days of culture using a Calcein AM/ethidium homodimer-1 dye (LIVE/DEAD Cell Viability Assay, Life Technologies) under the protocol instruction from the manufacturer. After 30 minutes of sample incubation with the reagents at 37 °C, they were washed with DPBS. The confocal microscope (Leica SP8, Germany) was used to obtain the images. Live and dead cells appeared as green and red, respectively.

The proliferation of hMSC was evaluated by the cell counting kit-8 (CCK-8, Thermo Fisher) on day 1, day 3, and day 5, respectively. The harvested cells were seeded on 96-well plates on the fiber surface at the density of 5×10^3 cells/cm². 10 µL of the CCK-8 solution was added to each well of 96-well plates with 100 µL medium, and cells were incubated at 37 °C for 4 h. The absorbance intensity of each sample was determined at a wavelength of 450 nm using a microplate reader (infinite M200PRO, TECAN, Switzerland). All experiments were repeated three times and six parallel replicates were read for each sample.

Cell morphology. The cellular spreading morphology and skeleton were stained with phalloidin-647/DAPI after 3 days of culture at the seeding density of 3×10^3 cells/cm²; the cells were washed with DPBS before fixing the sample with 4% paraformaldehyde for 20 min. 0.1% Triton X-100 in DPBS was used for 30 min to permeabilize the cell membrane. The samples were then incubated with Alexa Fluor 647 phalloidin at 1:400 and DAPI at 1:200 dilutions in DPBS each for 45 min sequentially. Following three additional washings with PBS, the samples were observed under an inverted confocal microscope (Leica SP8, Germany).

Osteogenic differentiation analysis

For all the osteogenic differentiation experiments, cells were cultured and seeded at the density of 3×10^3 cells/cm². Alkaline phosphatase (ALP) and calcium deposition were

employed as the biomarkers to test osteogenic activity. After 14 days of culture in osteogenic medium (Osteogenesis differentiation kit, Thermo Fisher), the ALP markers of hMSC were stained according the protocol from Thermo Fisher (Alkaline Phosphatase Live Stain (500X)); the samples were observed under the confocal (Leica SP8, Germany). To assess the ALP activity, the samples were washed with PBS twice to remove the medium and lysed in lysis buffer containing 1% Triton-100 followed by centrifugation at 10,000 rpm for 20 min at 4 °C. Following the instructions, the supernatant was collected to measure the ALP activity with Alkaline Phosphatase Assay Kit (Abcam) and the total protein content was quantified with BCA Protein Assay Kit (Thermo Fisher). The ALP activity was normalized against the $\mu\text{mol}/\text{assay time}/\text{mg protein}$.

To evaluate the calcium deposition in osteogenic differentiation, Alizarin Red S (ARS, Thermo Fisher) staining was performed. Similarly, the samples were washed with PBS after cultured in osteogenic medium for 14 days and fixed with 1% paraformaldehyde for 2 min, followed by quick rinsing with PBS and then incubated with 0.1% Alizarin Red S for 30 min to stain the calcium deposits. The samples were further washed twice with PBS. For a quantitative calcium deposition assay, the stained cells were dried and eluted with 5% formic acid solution for 20 min, followed by transferring into a new 96-well plate and measuring the absorbance at 405 nm. All the mentioned steps were conducted at room temperature.

Immunofluorescence staining. The samples were then fixed in 4% paraformaldehyde and permeabilized with 0.1% Triton X-100 in PBS. The non-specific binding epitopes were blocked with 5% (w/v) BSA (bovine serum albumin). The primary antibodies anti-YAP IgG (1:400, rabbit; cell signaling); anti-RUNX2 IgG (1:400, mouse; cell signaling); anti-Vinculin IgG (1:400, rabbit; Thermo Fisher); anti-Lamin A/C (1:400, mouse; cell signaling); anti-IBSP IgG (1:400, rabbit; Thermo Fisher) were dissolved in 5% (w/v) BSA. The samples were incubated with the primary antibodies at 4 °C

overnight. Following 3 to 4 times intensive washing (0.5 wt% Tween-20 in PBS), the secondary antibody labeling was performed with goat anti-mouse IgG conjugated to Alexa Fluor Plus 647 (Thermo Fisher) and goat anti-rabbit IgG conjugated to Alexa Fluor Plus 488 (Abcam). After repeated washing in PBS and nuclear counterstaining with DAPI, the osteogenic markers were then visualized under a confocal microscope (Leica SP8, Germany). All images were taken under the same exposure conditions for analyzing the relative fluorescence intensity.

For the F-actin staining, the samples were then fixed in 4% paraformaldehyde and permeabilized with 0.1% Triton X-100 in PBS. After repeated washing in PBS and stained with DAPI and Phalloidin (1:400, Thermo Fisher), the markers were then visualized under a confocal microscope (Leica SP8, Germany). All images were taken under the same exposure conditions for analyzing the relative fluorescence intensity.

***In vitro* bacterial disinfection properties of scaffolds.** In this study, *Escherichia coli* (*E. coli*, ATCC 6538) was chosen as gram-negative model bacteria and *Staphylococcus aureus* (*S. aureus*, ATCC 25922) was used as a model of gram-positive bacteria. The Mueller-Hinton Agar (MHA) and Mueller-Hinton Broth (MHB) were used as culture media.

Live/dead bacteria on the membrane: 1×1 cm membrane was firstly dispersed in 2 mL of 10⁵ colony-forming unit (CFU)/mL of the bacterial suspension. After co-culturing at 37 °C for 6 h and 12 h, the *E. coli* and *S. aureus* were stained by using LIVE/DEAD® BacLight Bacterial Viability Kits (Thermo Fisher), respectively. Then, the images were acquired via confocal laser scanning microscopy (CLSM, Leica, Switzerland). For the quantitative analysis, the density of bacteria was estimated by at least 3 fluorescence images.

To evaluate the bacterial inhibition capabilities when co-cultured with the membrane, the real-time optical density at 600 nm (OD₆₀₀) of the bacterial/PCL-C-ZnO dispersion was also monitored to study the growth trends of bacteria. 1×1 cm

membrane was firstly dispersed in 1 mL of 10^5 colony-forming unit (CFU)/mL of the bacterial suspension. After co-culturing at 37 °C for 3 h, the OD600 for the suspensions were then monitored by UV-vis spectroscopy every 3 h to make sure whether our samples could achieve bacterial inhibition.

Zn^{2+} ions released properties of PCL-C-ZnO: To study the Zn^{2+} ions release amount from the PCL-C-ZnO, the membrane was soaked in phosphate-buffered saline (PBS, pH 7.4) at 25 °C. The released amounts of Zn^{2+} ions at different time scales were then monitored by ICP-OES method.

Image analysis. Cell spreading area, the shape factor, and volume were quantified based on F-actin staining and nucleus form z-direction confocal imaging. The focal adhesion analysis was performed based on vinculin staining. The fluorescent intensity and contrast were drawn along the representation morphology of each cell under the 8-bit greyscale images. The area and integrated densities were measured by the calibrate function. At least 200 cells were evaluated for each independent sample. For measurements of YAP nucleus localization in scaffolds, the images were thresholded on each color channel to determine the nucleus and cytoskeleton area outside of the nucleus. The YAP nucleus localization ratio was calculated according to Equation 1.

$$\text{Nuclear YAP (nuclear/cytoplasmic)} = \frac{\frac{\text{Nuclear YAP intensity}}{\text{Area of nucleus}}}{\frac{\text{Cell YAP intensity} - \text{Nuclear YAP intensity}}{\text{Area of cell} - \text{Area of nucleus}}} \quad (1)$$

All the above-mentioned images were presented as maximum intensity and analyzed by Fiji software (based on ImageJ), and we determined the 2D fractal dimensional organization with a custom-developed MATLAB program (MATLAB, Natick, MA), which divided images into a series of regions of 100 pixels² spaced at 20 pixels and individually averaged to filter out noise throughout the cell study.

Corresponding 2D fractal dimensions (Df). Df was analyzed by MATLAB of the F-actin staining images. Interrogation windows are used to digitally subdivide cytoskeletal images. To characterize the cytoskeleton spatial arrangement and density, box counting is utilized to infer a fractal dimension (Df). Df is a dimensionless value to quantify the complex arrangement of cell cytoskeleton. Automated partitioning and analysis of whole-cell images using MATLAB for subcellular quantification of cytoskeleton structure process are as follows: custom algorithm automatically partitions cytoskeletal images into the relevant biological regions, from which a mask is generated and data extracted can be specific to these regions. (a) Initially, images of the cytoskeleton are imported for processing, which includes a series of segmentation procedures to outline the shape of the cell. (b) Each cytoskeleton image is then scanned using non-overlapping interrogation windows, within each, fractal analysis is performed through a box-counting method, quantifying the actin arrangement as defined by an edge detection filter. The regional mask is then used to differentiate perinuclear, cytosolic, and peripheral actin quantity and actin arrangement information from the raw cytoskeleton image and resultant 2D array of fractal dimension values, respectively. (c) A user-defined set distance is then used to redefine these boundaries, and pixels between the new and original boundaries form the masks required. This is repeated for each paired cytoskeleton image for the entire live imaging dataset. MATLAB commands used for the entire process are noted under the title of each step, and custom codes are further denoted with a “.m.”

Statistical analysis

All data were expressed as the means \pm standard deviations (s.d) with independent experiments. The statistical analysis was performed using one-way analysis of variance (ANOVA) with the Tukey honestly significant difference *post hoc* test using origin 9.0 software. The dates are indicated with (*) for $p < 0.05$, (**) for $p < 0.01$, and (***) for $p < 0.001$. NS stands for not significant.

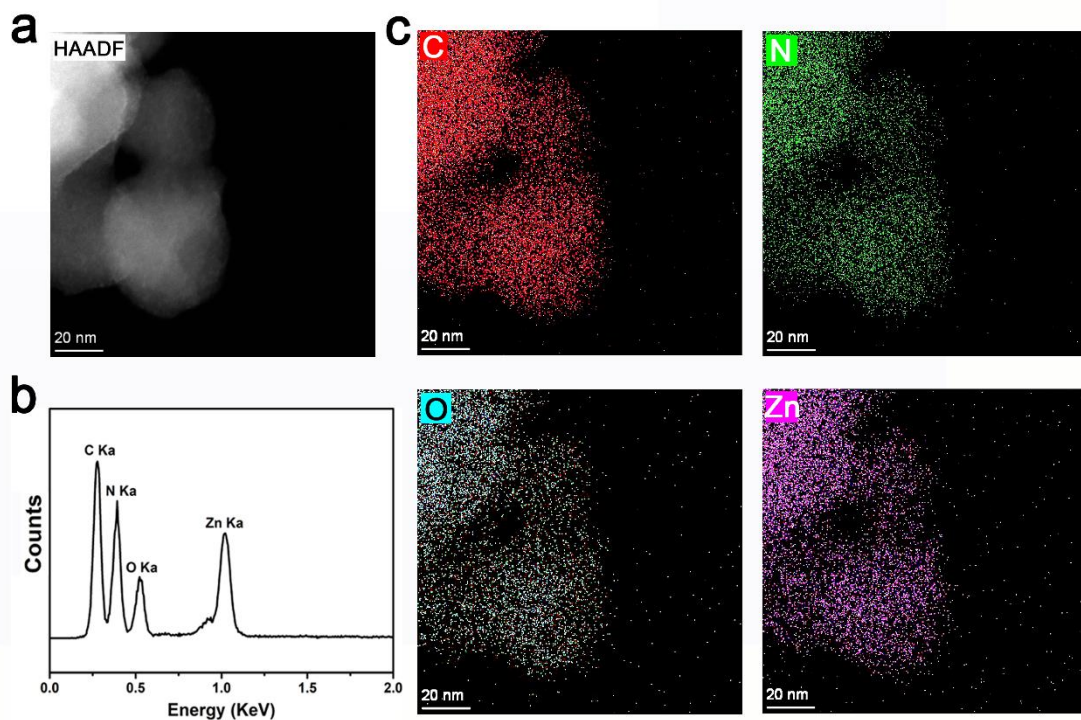


Figure S1. (a) HAADF-STEM image of the C-ZnO and corresponding elemental mapping for revealing the distribution of C, N, O, and Zn. (b) EDS curves of the C-ZnO particle. (c) The corresponding elemental mapping of C-ZnO for revealing the distribution of C, N, O, and Zn.

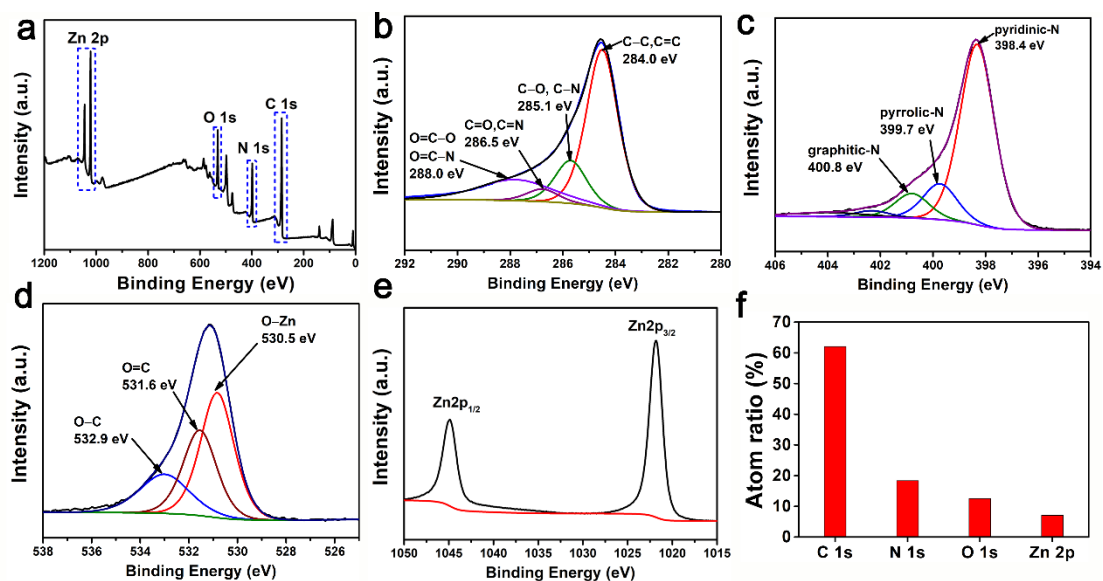


Figure S2. (a) XPS survey scanning spectra for C-ZnO. The high-resolution XPS (b) C1s spectra, (c) N1s spectra, (d) O1s spectra, and (e) Zn 2p spectra for C-ZnO. (f) The atom percentage of C, N, O, and Zn in C-ZnO nanoparticles.

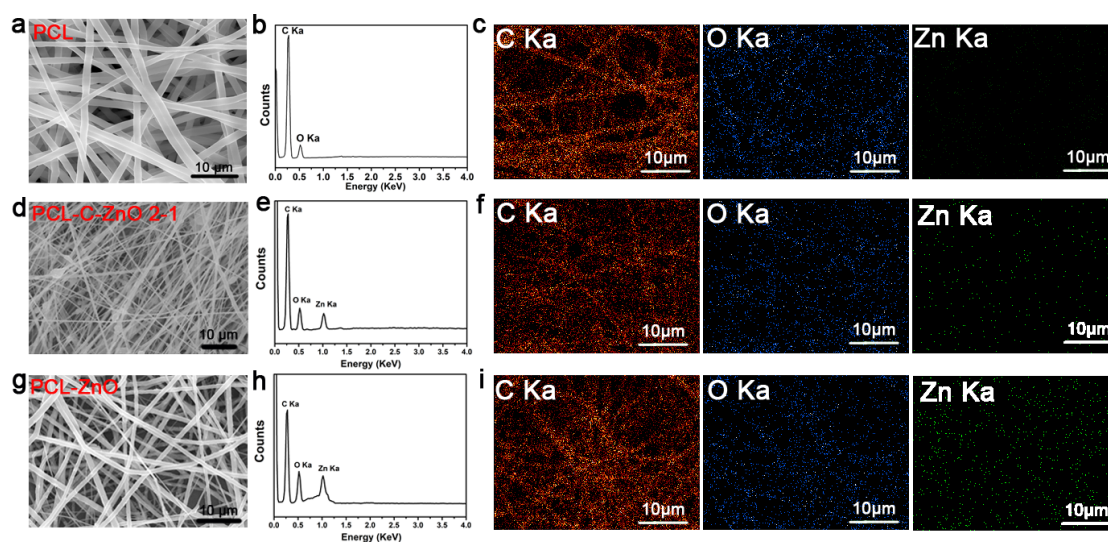


Figure S3. (a), (d), and (g) are SEM images of PCL, PCL-C-ZnO-2, and PCL-ZnO membranes. (b), (e), and (h) are EDS curves of PCL, PCL-C-ZnO-2, and PCL-ZnO

membranes. (c), (f), and (i) are the SEM element mapping of carbon (C), oxygen (O), and zinc (Zn) of PCL, PCL-C-ZnO-2, and PCL-ZnO membranes.

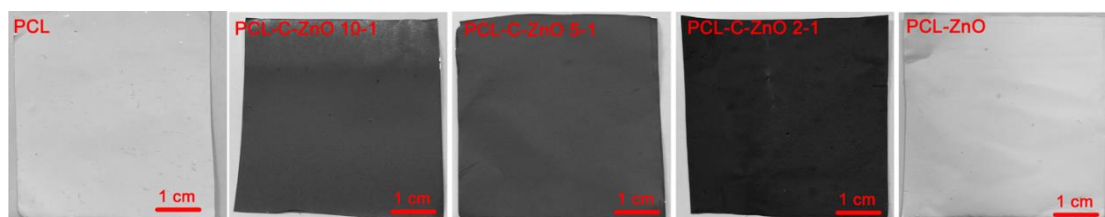


Figure S4. The photographic image for the electrospun bare PCL, PCL-C-ZnO, and ZnO scaffolds.

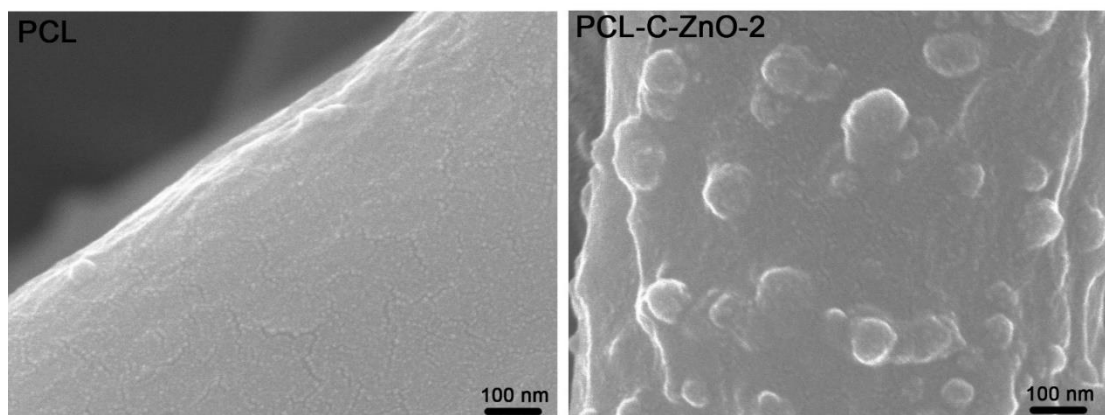


Figure S5. Amplified SEM image for the electrospun fibrous scaffold PCL and PCL-C-ZnO-2, the nanoparticles on the fiber are C-ZnO.

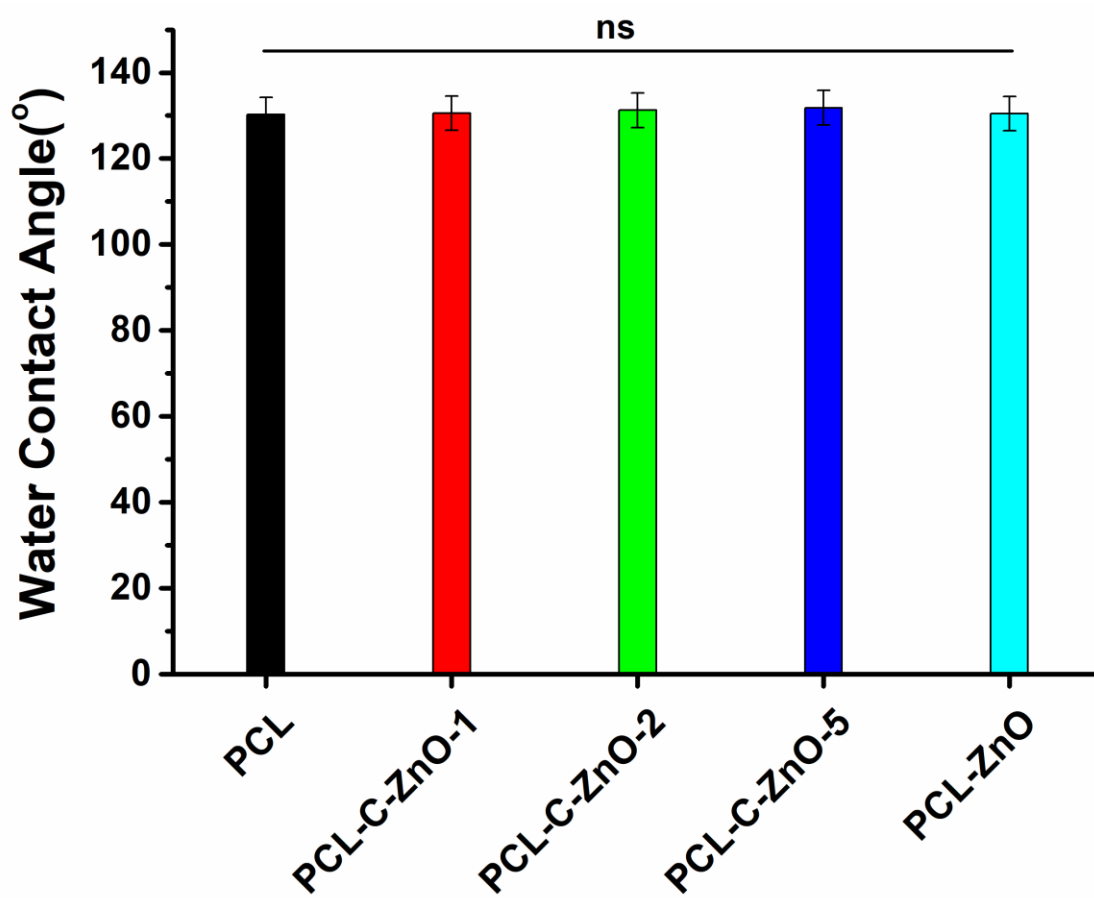


Figure S6. The water contact angles of PCL membrane, and the C-ZnO or ZnO incorporated membranes.

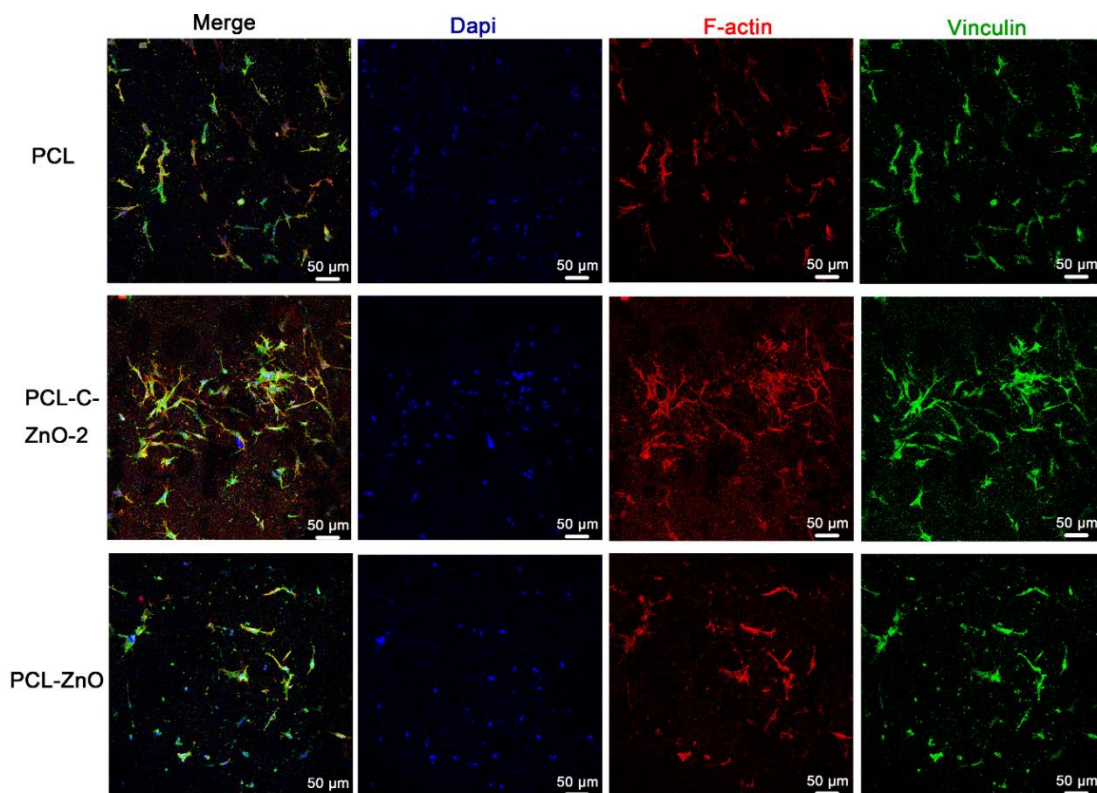


Figure S7. Confocal image of hMSCs growth on samples in growth medium; cells were stained with nuclei (blue), Vinculin (green), and F-actin (red).

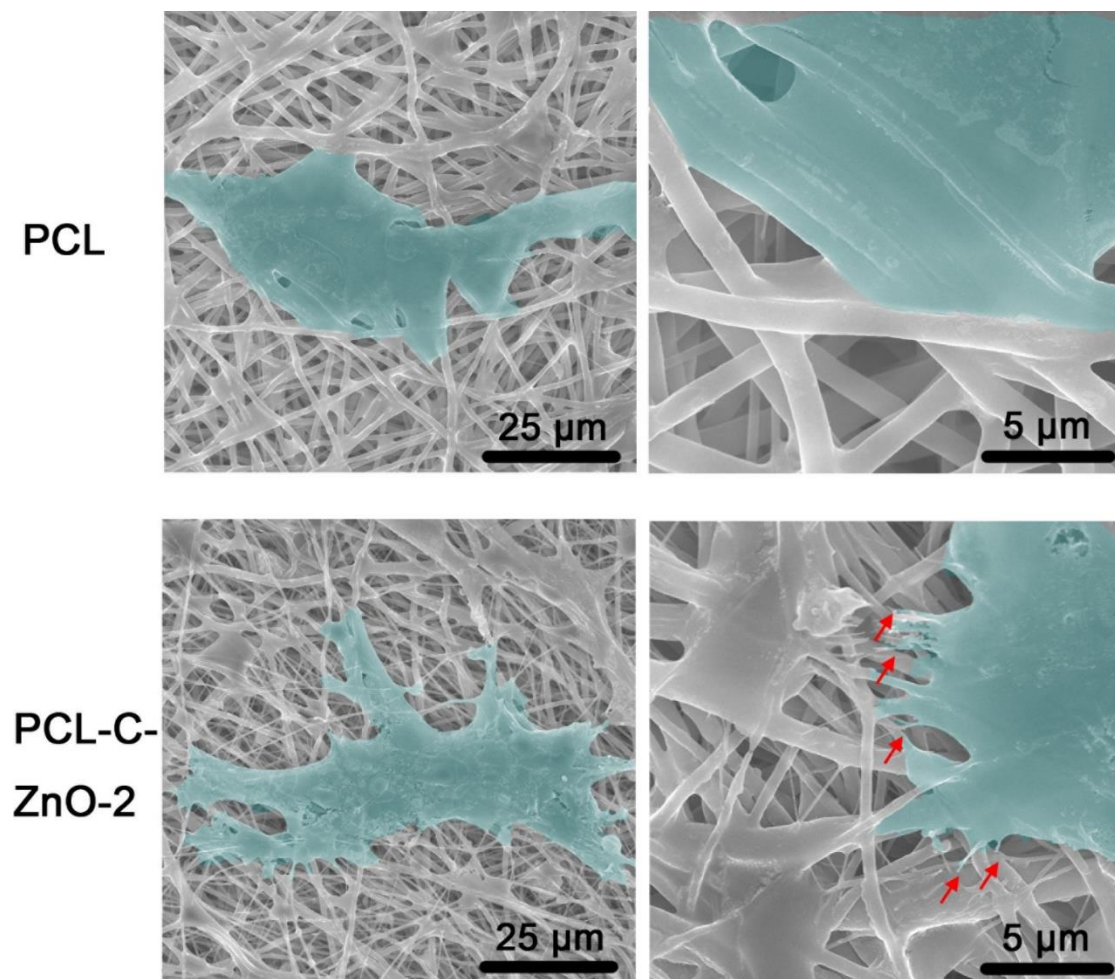


Figure S8. SEM images for the MSCs on PCL and PCL-C-ZnO scaffolds. The red errors are the pseudopodium.

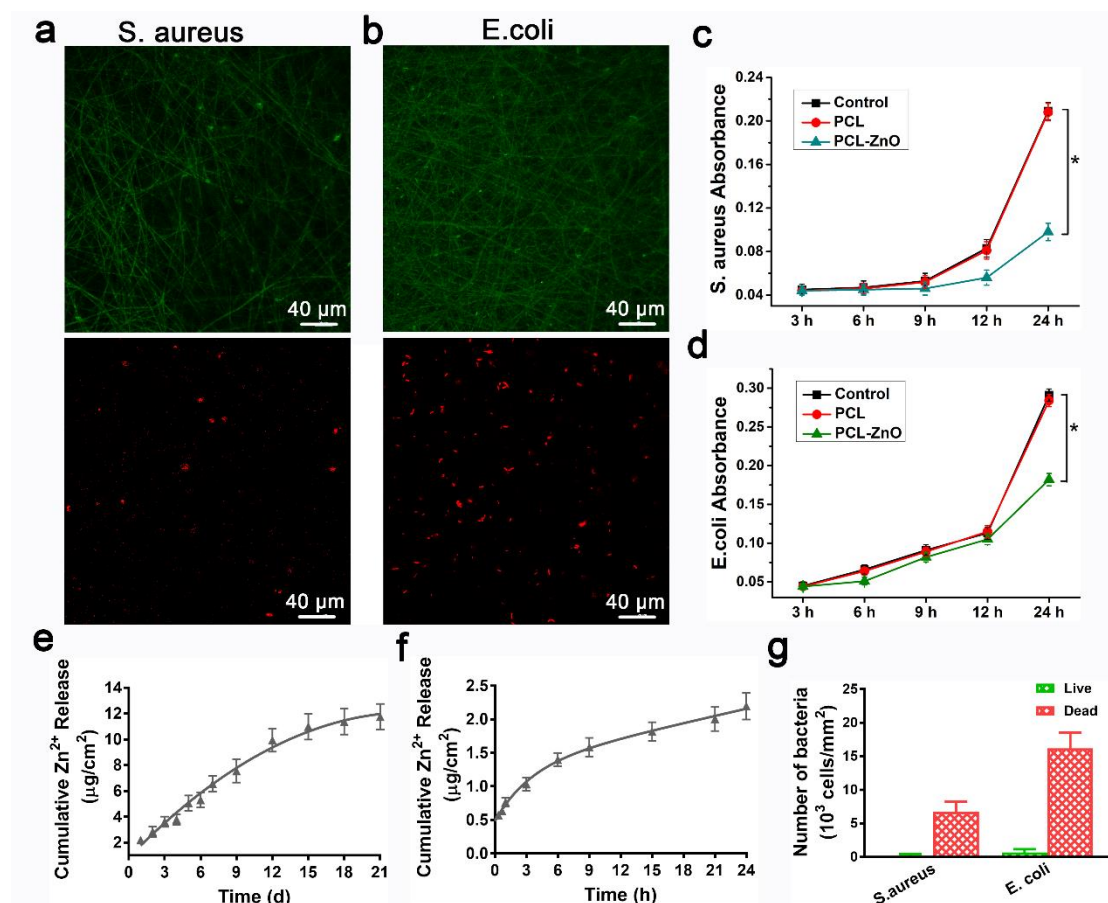


Figure S9. Live/dead staining images (red: dead, green: live) for (a) *S. aureus* and (b) *E. coli* after incubated PCL-ZnO for 12 h and 6 h, respectively. (c) and (d) are the short-term and long-term release of Zn^{2+} ions of the PCL-ZnO. (e) and (f) are Real-time OD₆₀₀ values for the control and samples with *S. aureus* and *E. coli*, respectively, (mean \pm SD, n = 5). P-values correspond the data after 24 h, *P < 0.05. (g) Corresponding numbers of live/dead bacteria on the membrane. The numbers were estimated from fluorescent photographs (mean \pm SD, n = 5). *P < 0.05, **P < 0.01.

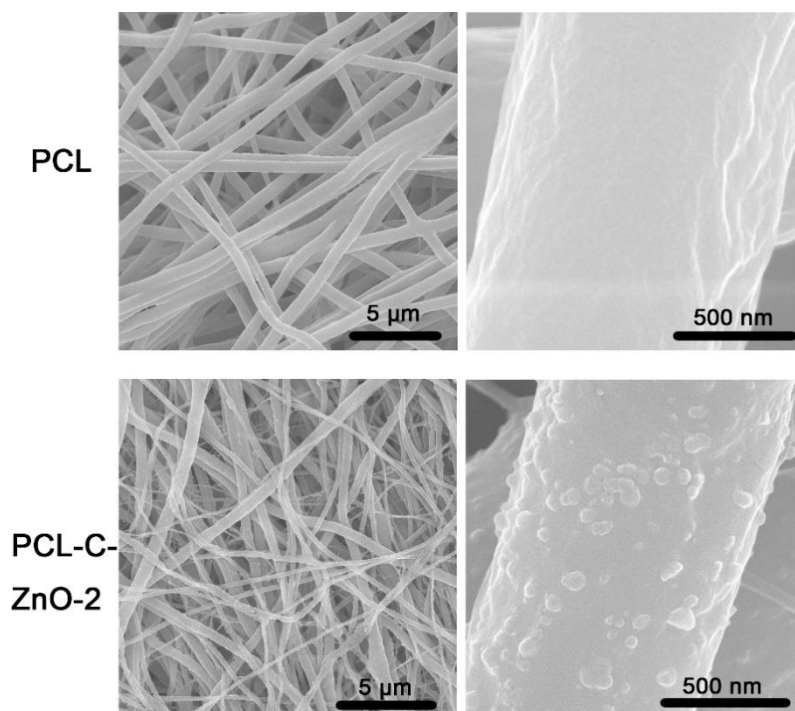


Figure S10. SEM image for the electrospun fibrous scaffold PCL and PCL-C-ZnO-2 after immersed in the medium for 14 days. There is no obvious degradation of the scaffolds.

Table S1. The added weight percentages of PCL and C-ZnO in the fibrous scaffolds, the calculated Zn^{2+} average weight ratio via the adding percentages, and the tested Zn^{2+} weight ratio from the XPS data of the scaffolds' surface.

| Samples | PCL | PCL-C-ZnO-1 | PCL-C-ZnO-2 | PCL-C-ZnO-5 | PCL-ZnO |
|-----------------------------|-----|-------------|-------------|-------------|---------|
| PCL : C-ZnO (wt %) | | 10:1 | 10:2 | 10:5 | 16.5:1 |
| Calculated Zn^{2+} (wt %) | 0 | 2.5 | 4.6 | 9.2 | 4.6 |
| XPS Tested Zn^{2+} (wt %) | 0 | - | 2.9 | - | 1.8 |

4. Summary and Outlook

This thesis mainly focused on the regulation of stem cells behavior by chemical and physical signals of carbon nanomaterial modified fibrous scaffolds. The cell adhesion on scaffolds is indirect via a surface layer of adsorbed proteins, thus the scaffold surface treatments could regulate the protein adsorption amount, cells adherence efficiency. The general property of scaffolds could further affect nutrient/waste exchange, protein synthesis, intracellular matrix construction and cell differentiation eventually, which is very important in stem cells-based tissue engineering, especially in organ and tissue damage. In this work, iPSCs and MSCs were used to investigate the effect on differentiation potential towards neuron and osteogenesis respectively via the chemical and physical cues of carbon nanomaterials-based scaffolds.

The first project prepared a multivalent polyanion-dispersed CNTs modified fibrous scaffolds to integrate the chemical and physical in stem cell regulation research. The CNTs are dispersed and functionalized by biocompatible and multivalent hyperbranched polyglycerol sulfate (HPGS) noncovalently. After air plasma treatment of electrospun fibrous polycaprolactone (PCL) scaffolds, the HPGS modified CNT, namely CNT-HPGS were coated on the PCL fiber surface to combine the chemical and physical cues. Results suggests that CNT-HPGS modified fibrous scaffold is suitable for stem cells adherence and growth, because the combination of CNT and multivalent HPGS on scaffolds surface could offer anchoring points for proteins, growth factors and cytokines, which is very important for stem cells behavior. Meanwhile, the modified scaffolds promote the neural differentiation efficiency due to the special physical property of carbon nanotubes. Moreover, the aligned fibrous scaffolds could orient the elongation direction of grown neurites. Thus, the promoted protein adhesion property of CNT-HPGS contribute to the stem cells growth microenvironment and provide a novel method to construct functional scaffolds for stem therapy research.

Since brutal plasma treatment could lead to polymer degradation and the longtime effects on surface may not be permanent, surface grafting of biocompatible and multivalent HPGS could be a suitable choice. In the second project, the HPGS was

covalently conjugated onto the graphene oxide (GO) nanosheet by using nitrene through a 2+1 cycloaddition reaction. The physical property of graphene oxide and chemical property of HPGS were combined to mediate the stem cells growth and differentiation. Then the GO-HPGS nanosheets functionalized nanofibrous scaffolds were applied to mediate the proliferation, lineage specification, and differentiation of iPSC. Results suggest that coated scaffolds could promote differentiation and maturity of iPSC towards neural differentiation. This study addressed the stability of the dispersion and promote the stem cell lineage specification maturity, which integrate the chemical and physical cues to facilitate the targeted differentiation of iPSC.

In the third project, we constructed a novel nanocarbon-structured fibrous scaffold for stem cell research, and the physical cues of carbon nanomaterials were MOF-derived nanocarbons. The porous carbon nanostructure could the promote the adhesion of proteins and growth factors, moreover, the caging property of the carbon nanostructure achieve the gradual release of chemical cues Zn^{2+} ions, which provide novel pathway for activation of signal pathways and guiding MSCs towards osteogenic differentiation process. This study designed stem cell scaffolds could help achieve multifunctional property, for example, simultaneously enhanced osteogenic and anti-infective capabilities.

In conclusion, this work combined the physical cues of carbon nanomaterials and other chemical cues to investigate the stem cell behavior, including the IPS cells towards neural differentiation and MSCs towards osteogenic differentiation process. The fabrication of scaffolds presented a novel avenue for the future development of carbon nanomaterials in tissue regeneration, bionic, biomedical, and bioelectronics.

5. Kurzzusammenfassung

Diese Arbeit befasst sich mit der Regulierung des Verhaltens von Stammzellen über die physikalischen und chemischen Signale von mit Kohlenstoff-Nanomaterialien modifizierten faserigen Gerüsten. Die Wachstumsumgebung von Stammzellen ist dynamisch und kompliziert. Weiterhin wird das Verhalten der Stammzellen, z.B. Adhäsion, Ausbreitung, Proliferation und Differenzierung durch die physikalischen und chemischen Eigenschaften des Gerüsts bestimmt, was bei der Stammzelltherapie und beim Tissue-Engineering, insbesondere bei Organ- und Gewebeschäden, sehr wichtig ist. In dieser Arbeit wurden induzierte pluripotente Stammzellen (IPS) und mesenchymale Stammzellen (MSC) verwendet, um die physikalischen und chemischen Eigenschaften der auf Kohlenstoff-Nanomaterialien basierenden Gerüste zu bewerten.

Das erste Projekt basiert auf multivalenten Polyanyon-dispergierten Kohlenstoffnanoröhren (CNT) auf einem faserigen Gerüst, um die chemischen und physikalischen Signale in der Stammzellregulations zu kombinieren. Die CNTs werden durch hyperverzweigtes Polyglycerinsulfat (hPGS) durch Ultraschall nicht-kovalent funktionalisiert. Nach der Sauerstoffplasmabehandlung von elektrogesponnenen faserigen Polycaprolacton-(PCL)-Gerüsten wurden CNT-HPGS-Nanodispersion auf die Oberfläche der PCL-Fasern aufgetragen, um die chemischen und physikalischen Signale zu untersuchen. Die Ergebnisse deuten darauf hin, dass CNT-HPGS-modifizierte faserige Gerüste als eine geeignete Plattform für die Adhäsion und Proliferation von Stammzellen dienen könnten. Dabei fördern die modifizierten nanostrukturierten faserigen Gerüste aufgrund der besonderen physikalischen Eigenschaft der Kohlenstoff-Nanoröhren die neuronale Differenzierungseffizienz. Darüber hinaus könnten die ausgerichteten faserigen Gerüste die Dehnungsrichtung von gewachsenen Neuriten orientieren. Auf diese Weise trägt die geförderte Proteinadhäsionseigenschaft von CNT-HPGS zur Mikroumgebung des Stammzellenwachstums bei und bietet eine neuartige Methode zur Konstruktion funktioneller Gerüste für die Stamm zell therapieforschung.

Im zweiten Projekt werde erfolgreich ein kovalent modifiziertes Graphen-oxid

(GO)-Polysulfat Verwendung von Nitren-HPGS durch eine 2+1 Cycloadditions-Reaktion hergestellt. Die physikalische Eigenschaft von GO und die chemische Eigenschaft von HPGS wurden kombiniert, um das Wachstum und die Differenzierung der Stammzellen zu vermitteln. Dann wurden die 2D-Nanoschichten mit funktionalisierten Nanofasergerüsten versehen, um die Proliferation, Abstammungsspezifikation und Differenzierung der Stammzellen zu vermitteln. Die Ergebnisse deuten darauf hin, dass beschichtete Gerüste die Differenzierung und Reife fördern könnten. Diese Studie befasste sich mit der Stabilität der Dispersion und der Förderung der Reife der Stammzell-Linienspezifikation, die die chemischen und physikalischen Signale integrieren, um die gezielte Differenzierung von IPS-Zellen zu erleichtern.

Im dritten Projekt konstruierten wir ein neuartiges faserförmiges Gerüst mit Nanokohlenstoffstruktur für die Stammzellforschung. Die Kohlenstoffnanomaterialien waren von MOF abgeleitete Nanokohlenstoffe. Die poröse Kohlenstoff-Nanostruktur die Adhäsion von Proteinen und Wachstumsfaktoren fördern. Darüber hinaus zeigte die Adhäsionseigenschaft der Kohlenstoff-Nanostruktur die allmähliche Freisetzung chemischer Signale, die einen neuen Weg zur Aktivierung von Signalwegen und zur Steuerung des Differenzierungsprozesses von Stammzellen bieten. Die in dieser Studie entworfenen Stammzellgerüste könnten dazu beitragen, multifunktionale Eigenschaften zu erreichen, z.B. gleichzeitig verbesserte osteogene und anti-infektiöse Fähigkeiten.

Zusammenfassend lässt sich sagen, dass diese Arbeit die physikalischen Signale von Kohlenstoff-Nanomaterialien und andere chemische Signale kombinierte, um das Verhalten von Stammzellen zu untersuchen, einschließlich der IPS-Zellen in Richtung neuronale Differenzierung von IPS-zellen und der osteogener Differenzierung von MSZ. Die Herstellung von multifunktionalen Gerüststrukturen stellte einen neuen Weg für die zukünftige Entwicklung von Kohlenstoff-Nanomaterialien in der Geweberegeneration, Bionik, Biomedizin und Bioelektronik dar.

6. References

- [1] M. L. Lovett, T. J. F. Nieland, Y.-T. L. Dingle, D. L. Kaplan, *Adv. Funct. Mater.* **2020**, 1909146.
- [2] R. G. Canter, J. Penney, L.-H. Tsai, *Nature* **2016**, 539, 187.
- [3] M. A. Hussain, N. D. Theise, *The Lancet* **2004**, 364, 203.
- [4] E. Dawson, G. Mapili, K. Erickson, S. Taqvi, K. Roy, *Adv. Drug Deliv. Rev.* **2008**, 60, 215.
- [5] N. D. Evans, E. Gentleman, J. M. Polak, *Mater. Today* **2006**, 9, 26.
- [6] M. Mimeault, S. K. Batra, *Stem Cells* **2006**, 24, 2319.
- [7] J. Bilic, J. C. I. Belmonte, *Stem Cells* **2012**, 30, 33.
- [8] M. F. Pittenger, A. M. Mackay, S. C. Beck, R. K. Jaiswal, R. Douglas, J. D. Mosca, M. A. Moorman, D. W. Simonetti, S. Craig, D. R. Marshak, *Science* **1999**, 284, 143.
- [9] I. Ullah, R. Abu-Dawud, J. F. Busch, A. Rabien, B. Erguen, I. Fischer, P. Reinke, A. Kurtz, *Biomaterials* **2019**, 216, 119283.
- [10] A. Singh, C. B. Yadav, N. Tabassum, A. K. Bajpeyee, V. Verma, *Eur. J. Cell Biol.* **2019**, 98, 65.
- [11] H. Amani, H. Arzaghi, M. Bayandori, A. S. Dezfuli, H. Pazoki-Toroudi, A. Shafiee, L. Moradi, *Adv. Mater. Interfaces* **2019**, 6, 1900572.
- [12] A. R. Murphy, A. Laslett, C. M. O'Brien, N. R. Cameron, *Acta Biomater.* **2017**, 54, 1.
- [13] I. Bartha, J. di Iulio, J. C. Venter, A. Telenti, *Nat. Rev. Genet.* **2018**, 19, 51.
- [14] Y. Huang, X.-F. Zhang, G. Gao, T. Yonezawa, X. Cui, *Biotechnol. J.* **2017**, 12, 1600734.
- [15] R. C. Dutta, A. K. Dutta, *Biotechnol. Adv.* **2009**, 27, 334.
- [16] S. Mohan, H. B. Raghavendran, P. Karunanithi, M. R. Murali, S. V. Naveen, S. Talebian, M. Mehrali, M. Mehrali, E. Natarajan, C. K. Chan, T. Kamarul, *ACS Appl. Mater. Interfaces* **2017**, 9, 9291.
- [17] A. R. Murphy, J. M. Haynes, A. L. Laslett, N. R. Cameron, C. M. O'Brien, *Acta Biomater.* **2020**, 101, 102.

- [18] C. J. Bettinger, R. Langer, J. T. Borenstein, *Angew Chem. Int. Ed. Engl.* **2009**, *48*, 5406.
- [19] E. D. Tabdanov, V. V. Puram, Z. Win, A. Alamgir, P. W. Alford, P. P. Provenzano, *Nat. Commun.* **2018**, *9*, 4891.
- [20] X. Yao, R. Peng, J. Ding, *Adv. Mater.* **2013**, *25*, 5257.
- [21] J. Fu, X. Liu, L. Tan, Z. Cui, Y. Liang, Z. Li, S. Zhu, Y. Zheng, K. W. Kwok Yeung, P. K. Chu, S. Wu, *Acta Biomater.* **2020**, *101*, 152.
- [22] M. K. Driscoll, X. Sun, C. Guven, J. T. Fourkas, W. Losert, *ACS Nano* **2014**, *8*, 3546.
- [23] N. Huebsch, E. Lippens, K. Lee, M. Mehta, Sandeep T. Koshy, Max C. Darnell, R. M. Desai, Christopher M. Madl, M. Xu, X. Zhao, O. Chaudhuri, C. Verbeke, Woo S. Kim, K. Alim, A. Mammoto, Donald E. Ingber, Georg N. Duda, David J. Mooney, *Nat. Mater.* **2015**, *14*, 1269.
- [24] T. Billiet, M. Vandehaute, J. Schelfhout, S. Van Vlierberghe, P. Dubruel, *Biomaterials* **2012**, *33*, 6020.
- [25] S. Van Vlierberghe, P. Dubruel, E. Schacht, *Biomacromolecules* **2011**, *12*, 1387.
- [26] I. M. Geisler, J. P. Schneider, *Adv. Funct. Mater.* **2012**, *22*, 529.
- [27] S. Hong, K. Yang, B. Kang, C. Lee, I. T. Song, E. Byun, K. I. Park, S.-W. Cho, H. Lee, *Adv. Funct. Mater.* **2013**, *23*, 1774.
- [28] X. Yao, Y. Liu, J. Gao, L. Yang, D. Mao, C. Stefanitsch, Y. Li, J. Zhang, L. Ou, D. Kong, Q. Zhao, Z. Li, *Biomaterials* **2015**, *60*, 130.
- [29] X. Sun, H. Zhang, J. He, R. Cheng, Y. Cao, K. Che, L. Cheng, L. Zhang, G. Pan, P. Ni, L. Deng, Y. Zhang, H. A. Santos, W. Cui, *Appl. Mater. Today* **2018**, *13*, 54.
- [30] A. L. Wollenberg, T. M. O'Shea, J. H. Kim, A. Czechanski, L. G. Reinholdt, M. V. Sofroniew, T. J. Deming, *Biomaterials* **2018**, *178*, 527.
- [31] W. J. Hadden, J. L. Young, A. W. Holle, M. L. McFetridge, D. Y. Kim, P. Wijesinghe, H. Taylor-Weiner, J. H. Wen, A. R. Lee, K. Bieback, B.-N. Vo, D. D. Sampson, B. F. Kennedy, J. P. Spatz, A. J. Engler, Y. S. Choi, *Proc. Natl. Acad. Sci.* **2017**, *114*, 5647.

- [32] S. H. Lim, H.-Q. Mao, *Adv. Drug Deliv. Rev.* **2009**, 61, 1084.
- [33] B. M. Baker, B. Trappmann, W. Y. Wang, M. S. Sakar, I. L. Kim, V. B. Shenoy, J. A. Burdick, C. S. Chen, *Nat. Mater.* **2015**, 14, 1262.
- [34] N. Su, P.-L. Gao, K. Wang, J.-Y. Wang, Y. Zhong, Y. Luo, *Biomaterials* **2017**, 141, 74.
- [35] P. Chen, J. Tao, S. Zhu, Y. Cai, Q. Mao, D. Yu, J. Dai, H. Ouyang, *Biomaterials* **2015**, 39, 114.
- [36] K. Carter, H. J. Lee, K.-S. Na, G. M. Fernandes-Cunha, I. J. Blanco, A. Djalilian, D. Myung, *Acta Biomater.* **2019**, 99, 247.
- [37] Z. Zhu, Y. Liu, Y. Xue, X. Cheng, W. Zhao, J. Wang, R. He, Q. Wan, X. Pei, *ACS Appl. Mater. Interfaces* **2019**, 11, 36141.
- [38] A. Salerno, P. A. Nettis, in *Biomedical Foams for Tissue Engineering Applications*, (Ed: P. A. Nettis), Woodhead Publishing, 2014, 71.
- [39] G. Akay, M. A. Birch, M. A. Bokhari, *Biomaterials* **2004**, 25, 3991.
- [40] Y. Cao, G. Mitchell, A. Messina, L. Price, E. Thompson, A. Penington, W. Morrison, A. O'Connor, G. Stevens, J. Cooper-White, *Biomaterials* **2006**, 27, 2854.
- [41] D. J. Griffon, M. R. Sedighi, D. V. Schaeffer, J. A. Eurell, A. L. Johnson, *Acta Biomater.* **2006**, 2, 313.
- [42] S. J. Hollister, *Nat. Mater.* **2005**, 4, 518.
- [43] S. Hofmann, H. Hagenmüller, A. M. Koch, R. Müller, G. Vunjak-Novakovic, D. L. Kaplan, H. P. Merkle, L. Meinel, *Biomaterials* **2007**, 28, 1152.
- [44] C. G. Jeong, S. J. Hollister, *Biomaterials* **2010**, 31, 4304.
- [45] J. Wang, H. Ma, X. Jin, J. Hu, X. Liu, L. Ni, P. X. Ma, *Biomaterials* **2011**, 32, 7822.
- [46] A. C. Jones, C. H. Arns, D. W. Hutmacher, B. K. Milthorpe, A. P. Sheppard, M. A. Knackstedt, *Biomaterials* **2009**, 30, 1440.
- [47] K. Kim, D. Dean, J. Wallace, R. Breithaupt, A. G. Mikos, J. P. Fisher, *Biomaterials* **2011**, 32, 3750.
- [48] A. Salerno, P. A. Nettis, E. Di Maio, S. Iannace, *J. Cell. Plast.* **2009**, 45, 103.

- [49] L. Fiocco, S. Li, M. M. Stevens, E. Bernardo, J. R. Jones, *Acta Biomater.* **2017**, 50, 56.
- [50] A. Higuchi, Q.-D. Ling, Y.-A. Ko, Y. Chang, A. Umezawa, *Chemical Reviews* **2011**, 111, 3021.
- [51] K. Y. Lee, D. J. Mooney, *Chem. Rev.* **2001**, 101, 1869.
- [52] A. Higuchi, S.-T. Yang, P.-T. Li, Y. Chang, E. M. Tsai, Y. H. Chen, Y.-J. Chen, H.-C. Wang, S.-T. Hsu, *Polym. Rev.* **2009**, 49, 181.
- [53] Y. Mei, K. Saha, S. R. Bogatyrev, J. Yang, A. L. Hook, Z. I. Kalcioğlu, S.-W. Cho, M. Mitalipova, N. Pyzocha, F. Rojas, K. J. Van Vliet, M. C. Davies, M. R. Alexander, R. Langer, R. Jaenisch, D. G. Anderson, *Nat. Mater.* **2010**, 9, 768.
- [54] Z. Melkounian, J. L. Weber, D. M. Weber, A. G. Fadeev, Y. Zhou, P. Dolley-Sonneville, J. Yang, L. Qiu, C. A. Priest, C. Shogbon, A. W. Martin, J. Nelson, P. West, J. P. Beltzer, S. Pal, R. Brandenberger, *Nat. Biotechnol.* **2010**, 28, 606.
- [55] A. J. Engler, S. Sen, H. L. Sweeney, D. E. Discher, *Cell* **2006**, 126, 677.
- [56] L. Little, K. E. Healy, D. Schaffer, *Chem. Rev.* **2008**, 108, 1787.
- [57] B. Balakrishnan, R. Banerjee, *Chem. Rev.* **2011**, 111, 4453.
- [58] B.-S. Kim, I.-K. Park, T. Hoshiba, H.-L. Jiang, Y.-J. Choi, T. Akaike, C.-S. Cho, *Prog. Polym. Sci.* **2011**, 36, 238.
- [59] P. M. Gilbert, K. L. Havenstrite, K. E. G. Magnusson, A. Sacco, N. A. Leonardi, P. Kraft, N. K. Nguyen, S. Thrun, M. P. Lutolf, H. M. Blau, *Science* **2010**, 329, 1078.
- [60] N. Huebsch, P. R. Arany, A. S. Mao, D. Shvartsman, O. A. Ali, S. A. Bencherif, J. Rivera-Feliciano, D. J. Mooney, *Nat. Mater.* **2010**, 9, 518.
- [61] G. J. R. Delcroix, P. C. Schiller, J.-P. Benoit, C. N. Montero-Menei, *Biomaterials* **2010**, 31, 2105.
- [62] A. Higuchi, Q.-D. Ling, S.-T. Hsu, A. Umezawa, *Chem. Rev.* **2012**, 112, 4507.
- [63] W. Qian, L. Gong, X. Cui, Z. Zhang, A. Bajpai, C. Liu, A. B. Castillo, J. C. M. Teo, W. Chen, *ACS Appl. Mater. Interfaces* **2017**, 9, 41794.
- [64] G. Thiruvikraman, G. Madras, B. Basu, *Biomaterials* **2016**, 77, 26.
- [65] S. Shrestha, B. K. Shrestha, J. I. Kim, S. Won Ko, C. H. Park, C. S. Kim, *Carbon*

2018, 136, 430.

- [66] K. H. Vining, D. J. Mooney, *Nat. Rev. Mol. Cell Bio.* **2017**, 18, 728.
- [67] M. Darnell, S. Young, L. Gu, N. Shah, E. Lippens, J. Weaver, G. Duda, D. Mooney, *Adv. Healthc. Mater.* **2017**, 6, 1601185.
- [68] J.-W. Shin, A. Buxboim, Kyle R. Spinler, J. Swift, David A. Christian, Christopher A. Hunter, C. Léon, C. Gachet, P. C. Dave P. Dingal, Irena L. Ivanovska, F. Rehfeldt, Joel A. Chasis, Dennis E. Discher, *Cell Stem Cell* **2014**, 14, 81.
- [69] D. R. Griffin, W. M. Weaver, P. O. Scumpia, D. Di Carlo, T. Segura, *Nat. Mater.* **2015**, 14, 737.
- [70] N. Gjorevski, N. Sachs, A. Manfrin, S. Giger, M. E. Bragina, P. Ordóñez-Morán, H. Clevers, M. P. Lutolf, *Nature* **2016**, 539, 560.
- [71] S. Lee, V. Serpooshan, X. Tong, S. Venkatraman, M. Lee, J. Lee, O. Chirikian, J. C. Wu, S. M. Wu, F. Yang, *Biomaterials* **2017**, 131, 111.
- [72] E. Serena, E. Figallo, N. Tandon, C. Cannizzaro, S. Gerecht, N. Elvassore, G. Vunjak-Novakovic, *Exp. Cell Res.* **2009**, 315, 3611.
- [73] G. Eng, B. W. Lee, L. Protas, M. Gagliardi, K. Brown, R. S. Kass, G. Keller, R. B. Robinson, G. Vunjak-Novakovic, *Nat. Commun.* **2016**, 7, 10312.
- [74] F. Xing, L. Li, C. Zhou, C. Long, L. Wu, H. Lei, Q. Kong, Y. Fan, Z. Xiang, X. Zhang, *Stem Cells Int.* **2019**, 2019, 2180925.
- [75] A. L. Ponte, E. Marais, N. Gallay, A. Langonné, B. Delorme, O. Hérault, P. Charbord, J. Domenech, *Stem Cells* **2007**, 25, 1737.
- [76] P. S. Lienemann, M. P. Lutolf, M. Ehrbar, *Adv. Drug Deliv. Rev.* **2012**, 64, 1078.
- [77] N. S. S. Halim, E. S. Ch'ng, E. Kardia, S. A. Ali, R. Radzi, B. H. Yahaya, *Stem Cell Rev. Rep.* **2019**, 15, 112.
- [78] S. Kuttappan, D. Mathew, J.-i. Jo, R. Tanaka, D. Menon, T. Ishimoto, T. Nakano, S. V. Nair, M. B. Nair, Y. Tabata, *Acta Biomater.* **2018**, 78, 36.
- [79] K. Haider Husnain, S. Jiang, M. Idris Niagara, M. Ashraf, *Circ. Res.* **2008**, 103, 1300.
- [80] J. Y. Kim, S. Y. Chun, J.-S. Park, J.-W. Chung, Y.-S. Ha, J. N. Lee, T. G. Kwon,

Tissue Eng. Regen. Med. **2018**, 15, 195.

[81] F. Li, Y. Liu, Y. Cai, X. Li, M. Bai, T. Sun, L. Du, *Ultrasound Med. Biol.* **2018**, 44, 1044.

[82] J. Pons, Y. Huang, J. Arakawa-Hoyt, D. Washko, J. Takagawa, J. Ye, W. Grossman, H. Su, *Biochem. Biophys. Res. Commun.* **2008**, 376, 419.

[83] D. De, D. Halder, I. Shin, K. K. Kim, *Chem. Soc. Rev.* **2017**, 46, 6241.

[84] Y. Zhang, W. Li, T. Laurent, S. Ding, *J. Cell. Sci.* **2012**, 125, 5609.

[85] S. Zhu, W. Wei, S. Ding, *Annu. Rev. Biomed. Eng.* **2011**, 13, 73.

[86] T. Xu, M. Zhang, T. Laurent, M. Xie, S. Ding, *Stem Cells Transl. Med.* **2013**, 2, 355.

[87] N. Cao, Y. Huang, J. Zheng, C. I. Spencer, Y. Zhang, J.-D. Fu, B. Nie, M. Xie, M. Zhang, H. Wang, T. Ma, T. Xu, G. Shi, D. Srivastava, S. Ding, *Science* **2016**, 352, 1216.

[88] G. Park, B. S. Yoon, Y. S. Kim, S.-C. Choi, J.-H. Moon, S. Kwon, J. Hwang, W. Yun, J.-H. Kim, C.-Y. Park, D.-S. Lim, Y. I. Kim, C. H. Oh, S. You, *Biomaterials* **2015**, 54, 201.

[89] W. Hu, B. Qiu, W. Guan, Q. Wang, M. Wang, W. Li, L. Gao, L. Shen, Y. Huang, G. Xie, H. Zhao, Y. Jin, B. Tang, Y. Yu, J. Zhao, G. Pei, *Cell Stem Cell* **2015**, 17, 204.

[90] S. Wang, J. Bates, X. Li, S. Schanz, D. Chandler-Militello, C. Levine, N. Maherali, L. Studer, K. Hochedlinger, M. Windrem, Steven A. Goldman, *Cell Stem Cell* **2013**, 12, 252.

[91] P. Hou, Y. Li, X. Zhang, C. Liu, J. Guan, H. Li, T. Zhao, J. Ye, W. Yang, K. Liu, J. Ge, J. Xu, Q. Zhang, Y. Zhao, H. Deng, *Science* **2013**, 341, 651.

[92] V. Bansal, D. De, J. An, T. M. Kang, H.-J. Jeong, J.-S. Kang, K. K. Kim, *Biomaterials* **2019**, 193, 30.

[93] S. Lorenz, C. P. Hauser, B. Autenrieth, C. K. Weiss, K. Landfester, V. Mailänder, *Macromol. Biosci.* **2010**, 10, 1034.

[94] H. Shin, S. Jo, A. G. Mikos, *Biomaterials* **2003**, 24, 4353.

[95] Y. Lin, S. Taylor, H. Li, K. A. S. Fernando, L. Qu, W. Wang, L. Gu, B. Zhou, Y.-P. Sun, *J. Mater. Chem.* **2004**, 14, 527.

- [96] T. Kuila, S. Bose, A. K. Mishra, P. Khanra, N. H. Kim, J. H. Lee, *Prog. Mater. Sci* **2012**, 57, 1061.
- [97] S. H. Ku, M. Lee, C. B. Park, *Adv. Healthc. Mater.* **2013**, 2, 244.
- [98] P. Kerativitayanan, J. K. Carrow, A. K. Gaharwar, *Adv. Healthc. Mater.* **2015**, 4, 1600.
- [99] Z. Peng, T. Zhao, Y. Zhou, S. Li, J. Li, R. M. Leblanc, *Adv. Healthc. Mater.* **2020**, 9, 1901495.
- [100] S. R. Shin, S. M. Jung, M. Zalabany, K. Kim, P. Zorlutuna, S. b. Kim, M. Nikkhah, M. Khabiry, M. Azize, J. Kong, K.-t. Wan, T. Palacios, M. R. Dokmeci, H. Bae, X. Tang, A. Khademhosseini, *ACS Nano* **2013**, 7, 2369.
- [101] S. Beg, M. Rizwan, A. M. Sheikh, M. S. Hasnain, K. Anwer, K. Kohli, *J. Pharm. Pharmacol.* **2011**, 63, 141.
- [102] S. Marchesan, K. Kostarelos, A. Bianco, M. Prato, *Mater. Today* **2015**, 18, 12.
- [103] H. Yu, H. Zhao, C. Huang, Y. Du, *ACS Biomater. Sci. Eng.* **2017**, 3, 3017.
- [104] S. R. Shin, R. Farzad, A. Tamayol, V. Manoharan, P. Mostafalu, Y. S. Zhang, M. Akbari, S. M. Jung, D. Kim, M. Comotto, N. Annabi, F. E. Al-Hazmi, M. R. Dokmeci, A. Khademhosseini, *Adv. Mater.* **2016**, 28, 3280.
- [105] H. Shao, T. Li, R. Zhu, X. Xu, J. Yu, S. Chen, L. Song, S. Ramakrishna, Z. Lei, Y. Ruan, L. He, *Biomaterials* **2018**, 175, 93.
- [106] C. Cheng, S. Li, A. Thomas, N. A. Kotov, R. Haag, *Chemical Reviews* **2017**, 117, 1826.
- [107] Z. Zhang, L. H. Klausen, M. Chen, M. Dong, *Small* **2018**, 14, 1801983.
- [108] C. Cheng, J. Zhang, S. Li, Y. Xia, C. Nie, Z. Shi, J. L. Cuellar-Camacho, N. Ma, R. Haag, *Advanced Materials* **2018**, 30, 1705452.
- [109] Y. Zou, N. T. Qazvini, K. Zane, M. Sadati, Q. Wei, J. Liao, J. Fan, D. Song, J. Liu, C. Ma, X. Qu, L. Chen, X. Yu, Z. Zhang, C. Zhao, Z. Zeng, R. Zhang, S. Yan, T. Wu, X. Wu, Y. Shu, Y. Li, W. Zhang, R. R. Reid, M. J. Lee, J. M. Wolf, M. Tirrell, T.-C. He, J. J. de Pablo, Z.-L. Deng, *ACS Appl. Mater. Interfaces* **2017**, 9, 15922.
- [110] J. Wang, C. Cui, H. Nan, Y. Yu, Y. Xiao, E. Poon, G. Yang, X. Wang, C. Wang,

L. Li, K. R. Boheler, X. Ma, X. Cheng, Z. Ni, M. Chen, *ACS Appl. Mater. Interfaces* **2017**, 9, 25929.

[111] C. Ding, A. Zhu, Y. Tian, *Acc. Chem. Res.* **2014**, 47, 20.

[112] S. Y. Lim, W. Shen, Z. Gao, *Chem. Soc. Rev.* **2015**, 44, 362.

[113] H. Chen, L. Wang, H. Fu, Z. Wang, Y. Xie, Z. Zhang, Y. Tang, *J. Mater. Chem. B* **2016**, 4, 7472.

[114] D. Shao, M. Lu, D. Xu, X. Zheng, Y. Pan, Y. Song, J. Xu, M. Li, M. Zhang, J. Li, G. Chi, L. Chen, B. Yang, *Biomater. Sci.* **2017**, 5, 1820.

[115] J. Zhuang, C.-H. Kuo, L.-Y. Chou, D.-Y. Liu, E. Weerapana, C.-K. Tsung, *ACS Nano* **2014**, 8, 2812.

[116] P. Horcajada, R. Gref, T. Baati, P. K. Allan, G. Maurin, P. Couvreur, G. Férey, R. E. Morris, C. Serre, *Chem. Rev.* **2012**, 112, 1232.

[117] D. K. Khajuria, V. B. Kumar, D. Gigi, A. Gedanken, D. Karasik, *ACS Appl. Mater. Interfaces* **2018**, 10, 19373.

[118] J. Liu, T. Jiang, C. Li, Y. Wu, M. He, J. Zhao, L. Zheng, X. Zhang, *Stem Cells Transl. Med.* **2019**, 8, 724.

[119] E. S. Place, J. H. George, C. K. Williams, M. M. Stevens, *Chem. Soc. Rev.* **2009**, 38, 1139.

[120] A. Kikuchi, T. Okano, *J. Control. Release* **2005**, 101, 69.

[121] H. R. Allcock, L. B. Steely, S. H. Kim, J. H. Kim, B.-K. Kang, *Langmuir* **2007**, 23, 8103.

[122] G. E. Park, M. A. Pattison, K. Park, T. J. Webster, *Biomaterials* **2005**, 26, 3075.

[123] Y. Zhu, M. F. Leong, W. F. Ong, M. B. Chan-Park, K. S. Chian, *Biomaterials* **2007**, 28, 861.

[124] U. Edlund, M. Källrot, A.-C. Albertsson, *J. Am. Chem. Soc.* **2005**, 127, 8865.

[125] Q. Chen, S. Yu, D. Zhang, W. Zhang, H. Zhang, J. Zou, Z. Mao, Y. Yuan, C. Gao, R. Liu, *Journal of the American Chemical Society* **2019**.

[126] J. Vonnemann, S. Liese, C. Kuehne, K. Ludwig, J. Dervede, C. Böttcher, R. R. Netz, R. Haag, *Journal of the American Chemical Society* **2015**, 137, 2572.

- [127] M. M. Stevens, J. H. George, *Science* **2005**, 310, 1135.
- [128] M. J. Dalby, N. Gadegaard, R. O. C. Oreffo, *Nat. Mater.* **2014**, 13, 558.
- [129] P. Kanchanawong, G. Shtengel, A. M. Pasapera, E. B. Ramko, M. W. Davidson, H. F. Hess, C. M. Waterman, *Nature* **2010**, 468, 580.
- [130] R. J. McMurray, N. Gadegaard, P. M. Tsimbouri, K. V. Burgess, L. E. McNamara, R. Tare, K. Murawski, E. Kingham, R. O. C. Oreffo, M. J. Dalby, *Nat. Mater.* **2011**, 10, 637.
- [131] Spencer W. Crowder, V. Leonardo, T. Whittaker, P. Papathanasiou, Molly M. Stevens, *Cell Stem Cell* **2016**, 18, 39.
- [132] H. Zhang, P. R. Patel, Z. Xie, S. D. Swanson, X. Wang, N. A. Kotov, *ACS Nano* **2013**, 7, 7619.
- [133] A. Trounson, C. McDonald, *Cell Stem Cell* **2015**, 17, 11.
- [134] J. Deng, C. Zhao, J. P. Spatz, Q. Wei, *ACS Nano* **2017**, 11, 8282.
- [135] A. Higuchi, Q.-D. Ling, Y. Chang, S.-T. Hsu, A. Umezawa, *Chemical Reviews* **2013**, 113, 3297.
- [136] S. Y. Park, J. Park, S. H. Sim, M. G. Sung, K. S. Kim, B. H. Hong, S. Hong, *Adv. Mater.* **2011**, 23, H263.
- [137] K. Alberti, R. E. Davey, K. Onishi, S. George, K. Salchert, F. P. Seib, M. Bornhäuser, T. Pompe, A. Nagy, C. Werner, P. W. Zandstra, *Nature Methods* **2008**, 5, 645.
- [138] Y. Xia, S. Li, C. Nie, J. Zhang, S. Zhou, H. Yang, M. Li, W. Li, C. Cheng, R. Haag, *Applied Materials Today* **2019**, 16, 518.
- [139] C. Cheng, S. Li, S. Nie, W. Zhao, H. Yang, S. Sun, C. Zhao, *Biomacromolecules* **2012**, 13, 4236.
- [140] M. F. Gholami, D. Lauster, K. Ludwig, J. Storm, B. Ziem, N. Severin, C. Böttcher, J. P. Rabe, A. Herrmann, M. Adeli, R. Haag, *Advanced Functional Materials* **2017**, 27, 1606477.
- [141] C. J. Wan, L. Q. Zhu, Y. H. Liu, P. Feng, Z. P. Liu, H. L. Cao, P. Xiao, Y. Shi, Q. Wan, *Adv. Mater.* **2016**, 28, 3557.

- [142] X. Fan, F. Yang, J. Huang, Y. Yang, C. Nie, W. Zhao, L. Ma, C. Cheng, C. Zhao, R. Haag, *Nano Lett.* **2019**.
- [143] Q. Wei, T. Becherer, P.-L. M. Noeske, I. Grunwald, R. Haag, *Advanced Materials* **2014**, 26, 2688.
- [144] Q. Wei, K. Achazi, H. Liebe, A. Schulz, P.-L. M. Noeske, I. Grunwald, R. Haag, *Angewandte Chemie International Edition* **2014**, 53, 11650.
- [145] B. De Strooper, E. Karran, *Cell* **2016**, 164, 603.
- [146] L. A. Rocha, D. Silva, S. Barata-Antunes, H. Cavaleiro, E. D. Gomes, N. A. Silva, A. J. Salgado, *Adv. Funct. Mater.* **2020**, n/a, 1909083.
- [147] M. J. Landry, K. Gu, S. N. Harris, L. Al-Alwan, L. Gutsin, D. De Biasio, B. Jiang, D. S. Nakamura, T. C. Corkery, T. E. Kennedy, C. J. Barrett, *Macromol. Biosci.* **2019**, 19, 1900036.
- [148] K. J. Brennand, A. Simone, J. Jou, C. Gelboin-Burkhart, N. Tran, S. Sangar, Y. Li, Y. Mu, G. Chen, D. Yu, S. McCarthy, J. Sebat, F. H. Gage, *Nature* **2011**, 473, 221.
- [149] G. Lee, E. P. Papapetrou, H. Kim, S. M. Chambers, M. J. Tomishima, C. A. Fasano, Y. M. Ganat, J. Menon, F. Shimizu, A. Viale, V. Tabar, M. Sadelain, L. Studer, *Nature* **2009**, 461, 402.
- [150] M. C. N. Marchetto, C. Carromeu, A. Acab, D. Yu, G. W. Yeo, Y. Mu, G. Chen, F. H. Gage, A. R. Muotri, *Cell* **2010**, 143, 527.
- [151] L. Hou, J. Kim, J. Coller, V. Natu, N. Huang, *Circulation Research* **2016**, 119, A357.
- [152] M. L. Lovett, T. J. F. Nieland, Y.-T. L. Dingle, D. L. Kaplan, *Adv. Funct. Mater.* **2020**, n/a, 1909146.
- [153] A. Higuchi, Q.-D. Ling, Y. Chang, S.-T. Hsu, A. Umezawa, *Chem. Rev.* **2013**, 113, 3297.
- [154] A. Higuchi, Q.-D. Ling, Y.-A. Ko, Y. Chang, A. Umezawa, *Chem. Rev.* **2011**, 111, 3021.
- [155] S. Gao, M. X. Chen, P. Wang, Y. Li, Z. G. Yuan, W. M. Guo, Z. Z. Zhang, X. L. Zhang, X. G. Jing, X. Li, S. Y. Liu, X. Sui, T. F. Xi, Q. Y. Guo, *Acta Biomater.* **2018**,

73, 127.

- [156] X. Sun, Y. Wang, Z. Y. Guo, B. Xiao, Z. Sun, H. Y. Yin, H. Y. Meng, X. Sui, Q. Zhao, Q. Y. Guo, A. Y. Wang, W. J. Xu, S. Y. Liu, Y. J. Li, S. B. Lu, J. Peng, *Adv. Healthcare. Mater.* **2018**, 7, 1800276.
- [157] X. Xue, Y. Sun, A. M. Resto-Irizarry, Y. Yuan, K. M. Aw Yong, Y. Zheng, S. Weng, Y. Shao, Y. Chai, L. Studer, J. Fu, *Nat. Mater.* **2018**, 17, 633.
- [158] J. Zhang, C. Cheng, J. L. Cuellar-Camacho, M. Li, Y. Xia, W. Li, R. Haag, *Adv. Funct. Mater.* **2018**, 28, 1804773.
- [159] M. J. Landry, F.-G. Rollet, T. E. Kennedy, C. J. Barrett, *Langmuir* **2018**, 34, 8709.
- [160] H. Chen, J. Sun, Z. Wang, Y. Zhou, Z. Lou, B. Chen, P. Wang, Z. Guo, H. Tang, J. Ma, Y. Xia, N. Gu, F. Zhang, *ACS Appl. Mater. Interfaces* **2018**, 10, 44279.
- [161] Y. Xia, J. Sun, L. Zhao, F. Zhang, X.-J. Liang, Y. Guo, M. D. Weir, M. A. Reynolds, N. Gu, H. H. K. Xu, *Biomaterials* **2018**, 183, 151.
- [162] K. Alberti, R. E. Davey, K. Onishi, S. George, K. Salchert, F. P. Seib, M. Bornhäuser, T. Pompe, A. Nagy, C. Werner, P. W. Zandstra, *Nat. Methods* **2008**, 5, 645.
- [163] M. X. Chen, Z. X. Feng, W. M. Guo, D. J. Yan, S. Gao, Y. Y. Li, S. Shen, Z. G. Yuan, B. Huang, Y. Zhang, M. J. Wang, X. Li, L. B. Hao, J. Peng, S. Y. Liu, Y. X. Zhou, Q. Y. Guo, *ACS Appl. Mater. Interfaces* **2019**, 11, 41626.
- [164] J. Xue, T. Wu, Y. Dai, Y. Xia, *Chem. Rev.* **2019**, 119, 5298.
- [165] J. Xue, T. Wu, J. Li, C. Zhu, Y. Xia, *Angew. Chem. Int. Ed.* **2019**, 58, 3948.
- [166] J. Xue, J. Xie, W. Liu, Y. Xia, *Acc. Chem. Res.* **2017**, 50, 1976.
- [167] J. Xue, C. Zhu, J. Li, H. Li, Y. Xia, *Adv. Funct. Mater.* **2018**, 28, 1705563.
- [168] C. Cheng, S. Li, A. Thomas, N. A. Kotov, R. Haag, *Chem. Rev.* **2017**, 117, 1826.
- [169] Y. Xia, S. Li, C. Nie, J. Zhang, S. Zhou, H. Yang, M. Li, W. Li, C. Cheng, R. Haag, *Appl. Mater. Today* **2019**, 16, 518.
- [170] C. X. Nie, L. Ma, S. Li, X. Fan, Y. Yang, C. Cheng, W. F. Zhao, C. S. Zhao, *Nano Today* **2019**, 26, 57.
- [171] L. Ma, M. Zhou, C. He, S. Li, X. Fan, C. Nie, H. Luo, L. Qiu, C. Cheng, *Green Chem.* **2019**, 21, 4887.

- [172] C. Cheng, J. Zhang, S. Li, Y. Xia, C. Nie, Z. Shi, J. L. Cuellar-Camacho, N. Ma, R. Haag, *Adv. Mater.* **2018**, 30, 1705452.
- [173] C. Cheng, S. Li, Y. Xia, L. Ma, C. Nie, C. Roth, A. Thomas, R. Haag, *Adv. Mater.* **2018**, 30, 1802669.
- [174] F. Paulus, D. Steinhilber, P. Welker, D. Mangoldt, K. Licha, H. Depner, S. Sigrist, R. Haag, *Polym. Chem.* **2014**, 5, 5020.
- [175] Q. Ran, X. Xu, P. Dey, S. Yu, Y. Lu, J. Dzubiella, R. Haag, M. Ballauff, *J. Chem. Phys.* **2018**, 149, 163324.
- [176] C. Fasting, C. A. Schalley, M. Weber, O. Seitz, S. Hecht, B. Kokschi, J. Dervede, C. Graf, E.-W. Knapp, R. Haag, *Angew. Chem. Int. Ed.* **2012**, 51, 10472.
- [177] Y. Xia, C. Cheng, R. Wang, H. Qin, Y. Zhang, L. Ma, H. Tan, Z. Gu, C. Zhao, *Polym. Chem.* **2014**, 5, 5906.
- [178] J. Vonnemann, S. Liese, C. Kuehne, K. Ludwig, J. Dervede, C. Böttcher, R. R. Netz, R. Haag, *J. Am. Chem. Soc.* **2015**, 137, 2572.
- [179] M. F. Gholami, D. Lauster, K. Ludwig, J. Storm, B. Ziem, N. Severin, C. Böttcher, J. P. Rabe, A. Herrmann, M. Adeli, R. Haag, *Adv. Funct. Mater.* **2017**, 27, 1606477.
- [180] S. Dupont, L. Morsut, M. Aragona, E. Enzo, S. Giulitti, M. Cordenonsi, F. Zanconato, J. Le Digabel, M. Forcato, S. Bicciato, N. Elvassore, S. Piccolo, *Nature* **2011**, 474, 179.
- [181] W. Deng, F. Shao, Q. He, Q. Wang, W. Shi, Q. Yu, X. Cao, C. Feng, S. Bi, J. Chen, P. Ma, Y. Li, A. Gong, S. Tong, J. Yu, M. Spector, X. Xu, Z. Zhang, *Adv. Mater.* **2019**, 31, 1806861.
- [182] B. Zhao, X. Wei, W. Li, R. S. Udan, Q. Yang, J. Kim, J. Xie, T. Ikenoue, J. Yu, L. Li, P. Zheng, K. Ye, A. Chinnaiyan, G. Halder, Z.-C. Lai, K.-L. Guan, *Genes & Development* **2007**, 21, 2747.
- [183] C. M. Madl, B. L. LeSavage, R. E. Dewi, K. J. Lampe, S. C. Heilshorn, *Adv. Sci.* **2019**, 6, 1801716.
- [184] I. Lian, J. Kim, H. Okazawa, J. Zhao, B. Zhao, J. Yu, A. Chinnaiyan, M. A. Israel, L. S. B. Goldstein, R. Abujarour, S. Ding, K.-L. Guan, *Genes & Development* **2010**, 24,

1106.

[185] Y. Li, H. Feng, H. Gu, D. W. Lewis, Y. Yuan, L. Zhang, H. Yu, P. Zhang, H. Cheng, W. Miao, W. Yuan, S.-Y. Cheng, S. M. Gollin, T. Cheng, *Nat. Commun.* **2013**, 4, 2174.

[186] H. Zheng, W.-M. Yu, J. Shen, S. Kang, D. Hambardzumyan, J. Y. Li, Y. Shen, A. M. Kenney, J. Chen, C.-K. Qu, *Sci. Adv.* **2018**, 4, eaat2681.

[187] J. Chen, S. Boyle, M. Zhao, W. Su, K. Takahashi, L. Davis, M. DeCaestecker, T. Takahashi, M. D. Breyer, C.-M. Hao, *Journal of the American Society of Nephrology* **2006**, 17, 1283.

[188] A. A. Sosunov, E. Guilfoyle, X. Wu, G. M. McKhann, J. E. Goldman, *J. Neurosci.* **2013**, 33, 7439.

[189] J. Lu, X. Zhong, H. Liu, L. Hao, C. T.-L. Huang, M. A. Sherafat, J. Jones, M. Ayala, L. Li, S.-C. Zhang, *Nat. Biotechnol.* **2016**, 34, 89.

[190] P. A. Nistor, P. W. May, F. Tamagnini, A. D. Randall, M. A. Caldwell, *Biomaterials* **2015**, 61, 139.

[191] G. Kouroupi, E. Taoufik, I. S. Vlachos, K. Tsioras, N. Antoniou, F. Papastefanaki, D. Chroni-Tzartou, W. Wrasidlo, D. Bohl, D. Stellas, P. K. Politis, K. Vekrellis, D. Papadimitriou, L. Stefanis, P. Bregestovski, A. G. Hatzigeorgiou, E. Masliah, R. Matsas, *PNAS* **2017**, 201617259.

[192] B. Ji, H. Kaneko, T. Minamimoto, H. Inoue, H. Takeuchi, K. Kumata, M.-R. Zhang, I. Aoki, C. Seki, M. Ono, M. Tokunaga, S. Tsukamoto, K. Tanabe, R.-M. Shin, T. Minamihisamatsu, S. Kito, B. J. Richmond, T. Suhara, M. Higuchi, *J. Neurosci.* **2016**, 36, 11544.

[193] K. W. Dunn, M. M. Kamocka, J. H. McDonald, *Am. J. Physiology-Cell Physiology* **2011**, 300, C723.

7. Abbreviations

| | |
|-------|--|
| mESCs | mouse embryonic stem cells |
| iPSCs | induced pluripotent stem cells |
| MSCs | mesenchymal stem cells |
| HSCs | hematopoietic stem cells |
| ECM | extracellular matrix |
| CNS | central nervous system |
| EBs | embryoid bodies |
| EF | electric stimulation |
| CNMs | carbon nanomaterials |
| CNTs | carbon nanotubes |
| SWNTs | single-walled nanotubes |
| MWNTs | multi-walled nanotubes |
| LbL | layer by layer |
| PDDA | poly(dimethyldiallylammonium chloride) |
| IPS | induced pluripotent stem cells |
| HPGS | hyperbranched polyglycerol sulfate |
| PCL | polycaprolactone |
| GO | graphene oxide |
| rGO | reduced graphene oxide |
| ALP | alkaline phosphatase |

8. Appendix

8.1 Publications

- [1] **Yi Xia**, Shuang Li, Chuanxiong Nie, Jianguang Zhang, Suqiong Zhou, Hua Yang, Mingjun Li, Wenzhong Li, Chong Cheng and Rainer Haag. *Appl. Mater. Today* **2019**, 16, 518–528.
- [2] **Yi Xia**, Xin Fan, Hua Yang, Ling Li, Chao He, Chong Cheng, and Rainer Haag. *Small* **2020**, 16, 2003010.
- [3] Chong Cheng, Shuang Li, **Yi Xia**, Lang Ma, Chuanxiong Nie, Christina Roth, Arne Thomas, Rainer Haag. *Adv. Mater.* **2018**, 30, 1802669.
- [4] Chuanxiong Nie, Marlana Stadtmüller, Hua Yang, **Yi Xia**, Thorsten Wolff, Chong Cheng, and Rainer Haag. *Nano Lett.* **2020**, 20, 7, 5367–5375.
- [6] Chong Cheng, Jianguang Zhang, Shuang Li, **Yi Xia**, Chuanxiong Nie, Zhenqiang Shi, Jose Luis Cuellar-Camacho, Nan Ma, Rainer Haag. *Adv. Mater.* **2018**, 30, 1705452.
- [6] Jianguang Zhang, Hua Yang, Bilen Emek Abali, Mingjun Li, **Yi Xia**, Rainer Haag. *Small*, **2019**, 15, 1901920.
- [7] Jianguang Zhang, Chong Cheng, Jose Luis Cuellar-Camacho, Mingjun Li, **Yi Xia**, Wenzhong Li, Rainer Haag. *Adv. Funct. Mater.*, **2018**, 28, 1804773.